Improved Synthesis and Material Processing of Black Phosphorus for Using as Lithium-ion Battery Anode

by

Jianyu Zhang

A dissertation submitted in partial fulfillment
of the requirements for the degree of
Doctor of Philosophy
(Mechanical Engineering)
in the University of Michigan
2020

Doctoral Committee:

Professor Wei Lu, Chair
Professor Pingsha Dong
Professor Jwo Pan
Professor Donald Siegel

Jianyu Zhang

zjianyu@umich.edu

ORCID iD: 0000-0002-0318-8112

Dedication

To my parents

Acknowledgements

I am very grateful to all individuals who have been keeping company with me throughout the last five years.

First of all, I appreciate my advisor and the committee chair Professor Wei Lu for his precious guidance, suggestion and support. Under his supervision, we completed several projects together with this dissertation. I have learnt a lot from his expertise and insights in different domains. His generous financial support and patient technical enlightenment help me explore challenging unknowns with fruitful results. His devotion to research and teaching will inspire me in my future work.

I also would like to express gratitude to my committee members Professor Jwo Pan, Professor Donald Siegel and Professor Pingsha Dong. From candidancy exam, to prelim, to final oral defense, Professor Pan and Professor Siegel gave me very constructive comments to improve my research. It was also a very unique experience to collaborate with Professor Dong on the MD simulation project. Your sharp advice extensively broadened my research horizon.

Along this unforgettable journey, I must thank Dr. Hosop Shin and Dr. Fengchao Liu. The collaboration with you on project and publication is full of encouragement and joy. I cherish your invaluable time and great ideas. Meanwhile, thanks my coworkers Dr. Guangyu Liu, Dandan Wang for your selfless help.

Last but most importantly, I am thankful to my family. The endless freedom, supports and love make this moment possible.

Table of Contents

List of Tables

List of Figures

List of Appendices

Abstract

Recent studies show that black phosphorus (BP) is a promising candidate anode material for Li-ion batteries (LIB), exhibiting much higher theoretical capacity (2,596 mAh/g) compared to commercialized graphite anode (372 mAh/g). Application of BP in LIB requires scalable material synthesis procedure, in-depth understanding of degradation mechanism and novel predictive models. In this work, a variety of synthesis, characterization, and modeling methods are developed to optimize the BP quality and promote its electrochemical performance in LIB.

BP is not naturally available. High energy mechanical milling (HEMM) is a conventional method which transforms red phosphorus (RP) precursor into BP. To precisely control the quality of BP, the effects of processing time, power, ball-to-powder ratio and atmosphere on BP's particle size distribution and crystallinity are systematically studied. A multistep milling technique combining planetary and shaking ball millings is developed. The produced BP and BP-graphite (BPG) composite have homogeneous size distribution, coherent bonding connection and high specific surface area. The as-synthesized material is used to fabricate half coin cell to test its electrochemical performance. The optimal sample cell achieves high initial capacity of 2000 mAh/g at 0.1C rate. After 150 cycles, more than 80% capacity is still reversible. Disassembly analysis reveals electrode cracks and particle fractures cause capacity degradation.

To address the bulk phase BP's intrinsic limitation of volume expansion and contraction upon cycling, 2D phosphorene (an analogy of graphene to graphite) is exfoliated from HEMM-synthesized BP particles. The laser-assisted liquid phase exfoliation is found to be superior than existing methods for its low cost, high productivity and significantly promoting phosphorene

stability. The as-exfoliated phosphorene is very durable against oxidation and humidity. Which relies on the polycrystalline properties of phosphorene and liquid protective layer.

A novel top-down co-exfoliation method to produce phosphorene-graphene heterostructure is developed. An ultrasonication system with moderate processing power is used to do liquid phase exfoliation. Instead of BP crystal, BPG composite from HEMM is directly utilized as precursor. The 2D layered material is found to be ultrathin (~10 nm) and ultrasmall (<2 μm), relieving the volume expansion issue in LIB. Moreover, phosphorene is chemically bonded to graphene, enabling high electronic conductivity and structural stability. Consequently, the phosphorene-graphene based LIB coin cells deliver state-of-the-art high rate (2,4,6 A/g) performance with high initial capacity (> 1500 mAh/g), long cycling life (> 500 cycles), and high capacity retention ratio (>80%). Galvanostatic Intermittent Titration Technique (GITT) shows fast solid-phase diffusion. Impedance evolution progress is investigated by Electrochemical Impedance Spectroscopy (EIS) test. The improvement doesn't only come from conventional conversion/alloying reaction between lithium and phosphorus, but also electrode-electrolyte interface pesudocapacitive effect due to high surface area of 2D phosphorene. This effect is quantified by properly designed Cyclic Voltammetry (CV) test. A non-destructive 3D micro-CT rendering is built to track the electrode structural change after battery cycling.

A data-driven machine learning framework is proposed to aggregate both cycling-related and material-related features into a predictive model. Which is able to estimate failed/alive batteries and identify important material influencers. 90 in-lab made BP-based coin cells from 16 batches are cycled to extract degradation patterns. Combining the material and electrode properties, the most comprehensive alternative anode database is formed. The insights from modeling can further optimize the material/electrode design.

Chapter 1

Introduction

1.1 Anode Materials for Lithium-Ion Battery

Since Sony commercialized the first version of Lithium (Li)-ion batteries (LIB) in 1991, fast development of this rechargeable battery has been changing worldwide energy industry. LIB has superior energy density and power density, making it suitable for electric vehicles (EVs) and portable electronic devices. With growing concern for reducing greenhouse gases emission, there will be more demand for LIB in the future.

In current commercial LIB, graphite is the most widely used negative electrode material. During electrochemical reaction, Li intercalates into the interlayer space between graphene until every six carbon atoms store one Li ion. This reaction mechanism delivers theoretical capacity of 372 mAh/g. Due to fast intercalation kinetics, practical capacity is usually close to the theoretical value (~360 mAh/g) [1].

However, the intrinsic limitation of graphite makes it impossible to further increase its capacity. Alternative anode materials attract great attention in recent years. The first major group is carbonaceous anode materials, such as carbon blacks, hard carbon, carbon nanotubes and mesocarbon. These non-graphitic carbons usually bear their own unique advantages. For example, hard carbon has good thermal stability, enabling LIB to be used safely under high temperature scenario with reversible capacity of 675 mAh/g [2]. Carbon nanotube has high conductivity and structural integrity, which can be directly used or form composite with other materials in LIB [3].

Expanded mesocarbon microbeads (EMCMB) showed large exchange current density and almost 100% capacity retention after 50 cycles [4].

Besides carbonaceous negative electrode materials, various conversion/alloying reaction based materials have been extensively researched. Conversion compounds such as Fe_2O_3 (1007 mAh/g), Fe_3O_4 (924 mAh/g), MnO (756 mAh/g), Mn_3O_4 (937 mAh/g), CoO (715 mAh/g), Co_3O_4 (890 mAh/g), CuO (674 mAh/g), Cr_2O_3 (1,058 mAh/g) can deliver very high specific capacity [5], owing to multiple electron reaction is possible per transition metal. The general reaction can be expressed as Equation (1.1), in which M is a transition metal, X is an anion, and n is the oxidation number of the transition metal ion in MX.

$$nLi^{+} + ne^{-} + M^{n+}X = Li_{n}X + M^{0} \tag{1.1}$$

There are two major challenges of applying conversion reaction-based transition metal oxides. First, the difference in voltage hysteresis causes energy density inefficiency. Additionally, large volume changes during charging and discharging results in capacity fade. Proper nanostructures have been designed to overcome these issues, such as nanowires, nanosheets, hollow structures, porous structures, and oxide/carbon nanocomposites.

Some metals (Si, Ge, and Sn), forming alloys with Li, can electrochemically store Li ions by Equation 1.2. Alloying reaction involves breaking the bonds between host atoms, causing dramatic structural changes in the process. The reaction is not constrained by the atomic framework of the host, contributing to much higher specific capacity. The Li-Si alloy phase is famous for highest 4,200 mAh/g theoretical capacity. However, the large amount of Li ions inserting into the host materials causes extreme volume expansion, up to 300% for fully lithiated Si. Which will make active materials fragmentation, electrical contact loss, accelerated irreversible side reaction and finally capacity drop. Preventing such mechanical fracture by nanostructure design and improving electrode fabrication procedure are essential to make these materials practically useful [6]. BP studied in this work also has alloying reaction with Li.

$$M + nLi^{+} + ne^{-} = Li_{n}M \tag{1.2}$$

1.2 Black Phosphorus and Phosphorene

BP is not naturally available. It was synthesized from white phosphorus for the first time in 1914, using a high pressure of 1.2 GPa and a high temperature of 200 °C [7]. Compared to easily ignitable white phosphorus and RP, BP is thermally stable in the air. Van der Waals force is the most important attractive force to determine the order of stability of all known phosphorus allotropes, which identifies orthorhombic BP as the most thermodynamically stable allotrope at 0 K. In 1981, large single crystals of BP were first successfully obtained from melted RP through a wedge-type cubic high-pressure apparatus [8]. Lower pressure synthesis methods assisted by mineralizer: Au, Sn and SnI_4, were reported recently [9].

BP has three crystalline structures: orthorhombic, simple cubic, and rhombohedral. Under normal pressure condition, BP holds an orthorhombic puckered layer structure, shown in Figure 1.1. Each phosphorus atom connects with the nearest three atoms through covalent bonds, forming each layer into a corrugated shape. For a single-layer BP, it has two atomic layers and two kinds of P–P bonds. In the same plane, the shorter bond with a length of 0.2224 nm connects the nearest P atoms. And the longer bond length of 0.2244 nm connects P atoms between the top and bottom of a single layer. It is an asymmetrical crystal, which leads to many anisotropic mechanical, electronic and thermal properties. In vertical direction, the Van der Waals bond can be easily compressed or exfoliated. While in the x-y plane, linear thermal expansion coefficients is approximately 2.5 times larger than that along zigzag direction at 300 K [10]. The migration barrier in the zigzag direction is 0.08 eV for Li ion on a phosphorene surface. But for armchair direction, the barrier is 0.68 eV [11]. Luo et al. [12] found that the thermal conductivity anisotropic ratio of the two directions was about 2 for BP films. The anisotropic phonon dispersion was thought to influence the observed anisotropy.

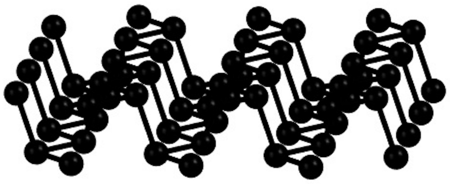

Figure 1.1 Side view of single layer phosphorene crystal lattice

The interlayer connection of BP is by Van der Waals force instead of covalent bonds. Therefore, it can be reduced to monolayer or few atomic layer in vertical direction. This thin film is usually called phosphorene, as an analogue of graphene to graphite. During phosphorene isolation from bulk BP, it's critical to control the thickness or number of layers. Several traditional exfoliation methods for graphene can be logically transferred to phosphorene. Mechanical exfoliation by adhesive tape generally produces highest quality crystal, but limited by scalability. Ar^+ plasma can partially assist thinning down with clear surface. Instead, liquid-phase exfoliation in an organic solution, typically N-methyl-2-pyrrolidone (NMP), dimethylformamide (DMF), dimethyl sulfoxide (DMSO), has much higher yield. Ion intercalation, ion exchange or ultrasonication power have been used to first expand BP and then loose the interlayer attraction. Liquid-phase processing in anhydrous and oxygen-free solvent can prevent phosphorene from oxidation and humidity contamination. Ambient degradation of phosphorene is the major obstacle hindering its application. Phosphorene quickly reacts with water and oxygen in the air to form phosphoric compound, losing all useful properties.

Since 2014, based on the extensive researches on graphene, few-layered hexagonal boron nitride (hBN), and transition metal dichalcogenides (TMDs), phosphorene reentered semiconducting industry. Similar to other 2-D layered materials, phosphorene has very unique electronic, optical and thermal properties. Theoretical computation has shown that monolayer phosphorene has extreme high hole mobility up to 10,000 $cm^2 \cdot V^{-1} \cdot s^{-1}$ [13]. It also has the direct band gap tunability from 0.3 eV (in bulk) to 1.5 eV (in monolayer) [14]. In addition to thickness, strain is theoretically predicted to influence band gap of phosphorene. A uniaxial compressive strain can transfer a direct band gad BP semiconductor to an indirect bandgap semiconductor, semimetal or even metal. Energy band structure can be modified by controlling the edge to be zigzag or armchair with different functional groups attached on the edge. The intermediate 0.3 eV band gap at bulk form fill the gap between zero gap of graphene and large 1.5-2.5 eV band gap for many TMDs. These properties pave the way for many electronic, photonic, thermoelectric and gas sensing applications. Phosphorene has strong optical conductivity in 1~5 μm wavelength range. Combining phosphorene with other 2D materials is studied for optoelectronics devices as detector, modulator and light-emitting diodes (LED) [15].

1.3 Current Application of BP/phosphorene in LIB

Although several efforts have been made to use red phosphorus (RP) for battery systems, the direct use of RP in a practical battery system is limited due to safety concern [16]. RP is more flammable than BP and can be easily ignited at moderate temperature when exposed to air. In addition, heated RP in the presence of moisture creates phosphine gas, which is both highly flammable and toxic. These reactive or unstable characteristics of RP would be problematic in manufacturing battery electrodes. Moreover, RP has an amorphous structure with poor bulk conductivity.

BP is an excellent candidate to be a next-generation anode material, enabling high energy density battery systems. It theoretically gives the specific capacity of 2,596 mAh/g (calculated in Equation 1.3), that is significantly higher than the capacities of current generation anodes (graphite, 372 mAh/g) and closer to that of a silicon anode. To be used an electrode anode, good electronic conductivity and ion diffusivity are vital. Bulk BP or phosphorene is a fairly good conductor of electrons. Combining with various carbon sources, the mobility has the order of 1,000 $cm^2 \cdot V^{-1} \cdot s^{-1}$. During lithiation process in Figure 1.2 and Equation 1.4, the intermediate products like LiP_5, Li_3P_7, LiP were studied for electronic and atomic structures. The results showed moderate electronic conductivity decline after Li intercalation into BP. At the same time, transport of lithium ions could conduct electricity unaffected. Overall, BP-based LIB would have good electronic conductivity and fast ion transport.

$$\frac{26.8\ Ah}{1\ mol\ Li} \times \frac{1\ mol\ Li}{{}^{1}/_{3}\ mol\ P} \times \frac{1\ mol\ P}{30.97\ g} = 2{,}596\ mAh/g \tag{1.3}$$

$$BP \rightarrow Li_xP \rightarrow LiP \rightarrow Li_2P \tag{1.4}$$

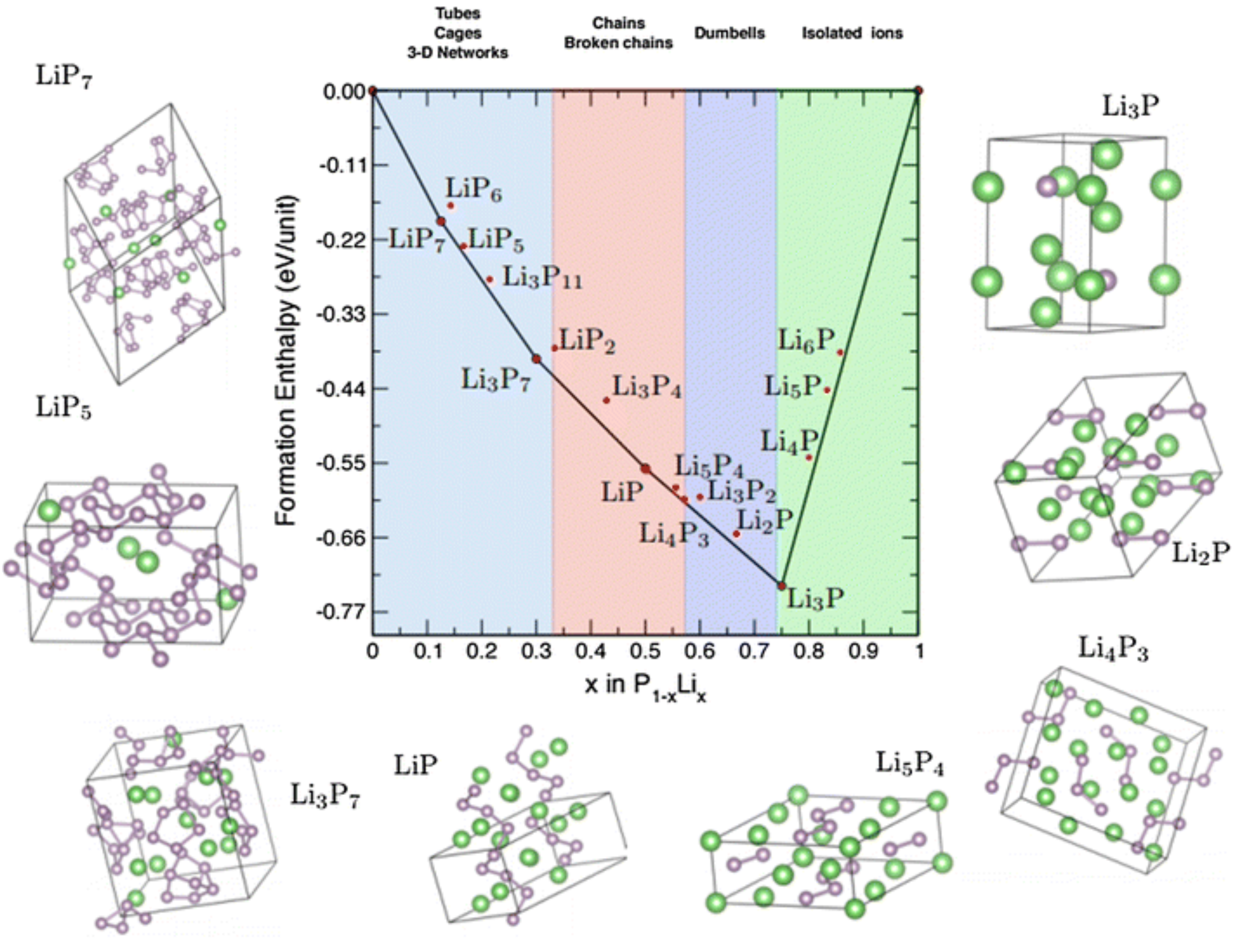

Figure 1.2. Formation enthalpy per atom versus the fractional lithium concentration in the Li–P compound. The green and purple spheres denote Li and P atoms, respectively, and the purple lines indicate P–P bonds [17].

Despite the great potential of BP as an alternative anode material, three main challenges have been hindered its application for industrial battery system. First, a scalable and energy-efficient synthesis or processing technique for high-quality BP has not been established yet. To transform BP from white P or RP, a high-pressure and high-temperature synthesis condition is required. The synthesis environment must be precisely controlled in an inert atmosphere due to safety issue. Although several methods have been developed for the production of BP, those methods either use toxic chemicals or complex apparatuses, or are time-consuming, or only produce a limited amount of BP. Second, the electronic conductivity of BP is not sufficient as a battery material. Ideally, BP exhibits a moderate electronic conductivity ($0.2{\sim}3.3\times10^{2}$ S/m), higher than silicon (10^{-3} S/m) but lower than graphite ($3.3\times10^{2}{\sim}2\times10^{5}$ S/m). However, the electronic conductivity of BP is quite dependent on the crystalline form (orthorhombic, rhombohedral, and simple cubic form) as well as the quality. With the synthesis method currently being used (such as, high-energy mechanical milling (HEMM)), it is difficult to synthesize a high quality of BP with a considerable electronic conductivity. Because of the low electronic conductivity, the electrochemical activity of BP is typically poor, showing low reversible capacities. To tackle the problem, many researchers have used nano-sized BP materials or synthesized phosphorous-carbon composite materials. Finally, similar to Si anode, BP suffers from a large volume change during lithiation/delithiation, which causes pulverization and fracture of the bulk BP. Consequently, the large volume change eventually leads to loss of electrical contact, which is the origin of severe capacity fade of BP-based batteries. Although the volume change percentage for orthorhombic BP being transformed to hexagonal Li_3P is theoretically 307 %, a recent *in-situ* transmission electron microscopy (TEM) has revealed that BP experiences an anisotropic volume change of 77 % upon delithiation. To withstand the mechanical stress induced by the large volume change, researchers have been using nano-sized BP along with various carbon materials [18].

A few studies have examined the electrochemical performance of pure BP and it was typically shown that first-cycle coulombic efficiency is very low and reversible capacity drops rapidly. This is because intrinsic electronic conductivity is not sufficient and a large volume change caused by Li_3P formation induces mechanical cracking and crumbling of BP, along with subsequent pulverization, delamination from current collectors. Therefore, BP must be first composited with other materials, such as graphite (G) and copper, to mitigate volume change and increase conductivity. Park *et al*. pioneered research into the synthesis of BP-G using high-energy mechanical milling (HEMM) for a battery application [19]. With the HEMM process, the pressure and temperature in the reaction vessel can reach approximately 6 GPa and 200 °C, respectively. They showed that BP phase transformation occurs sequentially as BP, LiP, Li_2P, and Li_3P upon discharging. Sun *et al*. implemented a high-pressure and high-temperature (HPHT) method using a cube-shaped pressure-transmitting medium and demonstrated the BP prepared using their method exhibits a higher electrochemical reactivity of BP toward Li insertion than BP produced by the HEMM method [20]. They emphasized that a better quality of BP in terms of electrochemical reactivity can be produced by precisely controlling the synthetic conditions.

BP has a larger 0.53 nm interlayer distance than graphite of 0.36 nm. Which enables it to accommodate both Li and Sodium ions. The *in-situ* transmission electron microscopy (TEM) studies revealed BP experiences an anisotropic volume change, which was approximately 77% (for the lithiation process) and 92% (for the sodiation process) [21]. Minimizing the size of BP is crucial to relieve the destructive volume expansion. Meanwhile, smaller size comes along with smaller crystallite size, which not only reduces the diffusion length for Li ions, but also promotes charge transfer capability. Given the intrinsic layered structure of BP, phosphorene naturally provides such advantages. The crystallinity of phosphorene is important, providing clear pathway for Li ions migration. Comparison study between low crystallinity and high crystallinity BP illustrates superiority of high crystallinity. It delivered first discharge and charge capacities of 2,649 and 1,425 mAh/g at a current density of 50 mA/g [22].

1.4 Outline of This Work

The goal of this dissertation is to systematically understand how to improve the electrochemical performance of BP and phosphorene in LIB. The dissertation is organized as following.

Despite there are many different strategies for BP synthesis, to satisfy our specific interest in BP battery application, in Chapter 2, a conventional BP synthesis method, high energy mechanical milling (HEMM), is optimized with respect to several key processing procedures and parameters. This method is known for its scalability and easiness, and is widely used in academia and industry for alloys and composites fine powder processing. However, its stochastic black-box nature makes the precise control difficult. To obtain satisfactory BP and BP-G for LIB, the relationship between HEMM processing and material property is carefully analyzed. Two distinctive mechanical milling techniques, shaker-mode and planetary-mode, are combined to produce BP and BP-G composite. The processing time, ball-to-powder ratio, ball size and procedure order affect the final product in different ways. Generally speaking, the optimal processing time, proper ball-to-powder ration and additional post treatment steps help to obtain high crystalline, super small and homogeneously distributed BP/BPG particles. Using the as-synthesized BP-G composite for LIB anode, high initial capacity with long term cyclability is achieved at moderate current density. Various electrochemical characterization methods are used to unveil the underlying mechanism of improvement. We find the optimal composite shows slow charge transfer increase, fast ion solid diffusion and enhanced reversibility/cyclability. Disassembly study for cycled cells reveals electrode crack and particle fracture related capacity degradation mechanism. When large isolated BP particles exist in the electrode, it is vulnerable for cracking during charge-discharge process. The pulverization effect exposes large amount of new electrode surface to electrolyte, consuming active Li ions and accumulating solid electrolyte interface (SEI) deposit. Inhomogeneous volume expansion causes electrode fracture and electronic contact loss. The BP and BP-G powders synthesized in Chapter 2 lay the foundation for incremental researches in Chapter 3-5.

Phosphorene is thought to be able to promote LIB rate capability, thanks to its fast ion diffusivity and mild volume change. In Chapter 3, A new liquid-phase exfoliation method using pulse laser as power source is developed to produce high quality phosphorene. Similar to other liquid-phase methods, the NMP solution protects as-exfoliated phosphorene against oxygen and humidity contamination. Pulse laser has the great advantage of only introducing short-term transient thermal excitation on BP. So the exfoliation is completed within short time without heat accumulation. This further prevents phosphorene from degradation. Another uniqueness of this phosphorene is that it is based on the HEMM-synthesized BP as precursor. Our method not only reduces the cost significantly, but also increases phosphorene's ambient stability evidenced by a variety of characterizations. The mechanism is that HEMM-synthesized BP has polycrystalline structure. It is more durable than the monocrystalline counterparty, due to free from clear initial reaction sites. After outside layer is corroded, internal phosphorene will not further react with the air. HEMM introduces defects and impurity on phosphorene also help ambient stability indirectly.

This finding supports the application of HEMM-synthesized BP based phosphorene in LIB, as studied in Chapter 4.

Phosphorene-graphene is usually used as hybrid structure in LIB. Previous researchers mixed separately exfoliated phosphorene and graphene in a self-assembly way, leaving the connection between phosphorene and graphene is maintained by weak Van der Waals. However, we prove that solid connection between P and C is vital for battery long term performance. To strengthen the phosphorene-graphene connection, a top-down co-exfoliation procedure is developed in Chapter 4, using HEMM-synthesized BP-G composite directly. The quality of produced phosphorene-graphene heterostructure is studied from material and electrochemistry perspectives. The pristine surface morphology and uniform lateral size and thickness demonstrate its suitability for battery application. Spectrum-based and microscopy-based characterization results prove solid chemical bonding between phosphorene and graphene, even after long time ultrasonication treatment. More important, the connection is not just intimate contact, but covalently chemical bonding. Therefore, the phosphorene-graphene based LIB achieved excellent rate performance at stressed cycling current density, over 500 cycles, without noticeable capacity degradation. Furthermore, cautiously designed electrochemical testing and non-destructive post cycling analysis reveal that fast solid phase diffusion, negligible impedance increase, pesudocapacitive effect, as well as structural robustness are responsible for the improvement.

Harvesting material synthesis data with cycling results, a dataset containing 90 sample cells from 16 batches are summarized in Chapter 5. This is so far the most comprehensive recording for alternative high capacity anode in LIB. It serves as a base for many additional analysis and modeling. Therefore, several machine learning models are fitted to classify failed or alive batteries at the end of 50 cycles. Overall, the models show good prediction accuracy and explanation power.

It can be detected that there exists strong relationship between electrode/particle properties to battery electrochemical performance. Some empirical degradation observations in Chapter 2-4 are numerically validated. Quantitative analysis and comparison identify most critical factors and provide guidance for improvement.

Chapter 2

Optimization of High Energy Mechanical Milling for Black Phosphorus Synthesis

2.1 Introduction

One approach to synthesize a chemically bonded composite structure is using a facile ball-milling process [18, 19, 23, 24]. While the ball-milling process cannot avoid the destruction of carbon materials, it enables production of the composites with a high ratio of phosphorus. It was proposed that the carbon structure plays an essential role in forming the stable P-C bond of the composite [23]. The study claimed graphite causes a strong P-C bond formation in the composite, contributing to a long cycle life and high-rate capability of the composite. Although HEMM synthesis is simple and easy to implement, there is an inherent limitation in controlling the reaction conditions precisely. And previous studies have shown conflicting results regarding the electrochemical performances of phosphorous-carbon composites. This is presumably due to several reasons: (1) the reported capacities of composites have been defined in a different manner (either based on the weight of phosphorous itself or the total weight of phosphorous and carbon) so that the rate of cycling (i.e., C-rate or current density) is not comparable to each other; (2) different synthesis methods or synthesis variables have been applied to make the composites; (3) carbon sources and the properties of carbon and BP were different; (4) different electrolyte, electrode composition, and active material loading have used to make LIB cells. Thus, there still remains a lack of understanding about the origin of significant differences in the electrochemical performances and how to improve the electrochemical performance of phosphorous-carbon or BP-carbon composite materials.

While many efforts have focused on the improvement of phosphorus-based materials, fundamental studies to understand the degradation of BP-based electrodes during cycling have rarely been conducted. Although mechanical failure (cracking, crumbling, or pulverization) had been envisioned, there was no direct evidence showing mechanical failure of BP-based anodes in the literature. This might be attributed to the fact that most researchers synthesized nanostructured phosphorus composites to better show electrochemical performance. With nanostructured phosphorus material, it might be difficult to detect any mechanical degradation at the particle level. In addition, it remains unclear how a better phosphorus-carbon composite can be synthesized in terms of electrochemical performance.

In this chapter, the correlation between black phosphorus-graphite (BP-G) material properties and cycle performance is systematically investigated by synthesizing and characterizing BP-G composite materials with different BP-G compositions. We found that the cycle performance of BP-G is significantly affected by the molar ratio of BP to graphite. BP-G with a low ratio of BP ($BP_{0.3}G_1$) shows moderate capacity fade, while BP-G with a high ratio of BP ($BP_{0.9}G_1$) exhibits rapid capacity fade within 20 cycles owing to more volume change and associated loss of electrical contact in the electrode. The use of Fluoroethylene carbonate (FEC) additive is effective in further improving the cycle performance of $BP_{0.3}G_1$; however, it does not mitigate the mechanical degradation of $BP_{0.9}G_1$ and its severe capacity fade. The ball-milling time affects not only the cycle performance of BP-G but also the reversible capacity and 1st cycle coulombic efficiency. An optimal ball-milling time needs to be identified to completely transform BP/G mixture to BP-G composite, which is directly correlated to the electrochemical performance. We reveal the mechanical degradation in BP-based anodes during cycling and present unknown degradation mechanisms that may undergo the poor cycle life of BP-based anodes. Finally, a multi-step ball-milling approach is employed to synthesize BP-G, which results in excellent reversible capacity (2,285 mAh/g) and superior cycle stability with the capacity retention of 80 % over 150 cycles.

2.2 Experimental

2.2.1 Material Synthesis

All the materials were handled in an Ar-filled glove box (<1 ppm O_2 and H_2O) and material synthesis was also carried out in the glove box using a shaker-type milling machine (SPEX, 8000M mixer/mill). Note there is a possibility that the remaining RP after BP synthesis can be inversely transformed to white phosphorus, which is easy to self-ignite in the air at approximately 30 °C. Thus, material synthesis should be conducted carefully in an inert condition. To prepare the BP powder, RP powder (100 mesh, 98.9% purity, Alfa Aesar) was used as a starting material. Using the shaker miller, the HEMM process was conducted to synthesize BP powder from RP. The RP (6 g) was put into a hardened steel cylindrical vial (65 mL) with hardened steel balls (10 balls with a diameter of 12.7 mm and 18 balls with a diameter of 6.35 mm). The ball to powder ratio for BP synthesis was 17:1.

For BP-G composite synthesis, the BP synthesized by the HEMM process (6 h) was put into a hardened steel vial (65 mL) with graphite power (Timrex SLP30, Timcal), and then hardened steel balls (10 balls, 12.7 mm in diameter; 18 balls, 6.35 mm in diameter) were added to the vial. The ball-to-powder ratio was 25:1. The BP-G (4 g) composite was synthesized for 6 h using the same shaker miller. BP-G composites with different molar ratios were prepared: low BP-ratio $BP_{0.3}G_1$ (43.6 wt.% of BP and 56.4 wt.% of graphite) and high BP-ratio $BP_{0.9}G_1$ (69.9 wt.% of BP and 30.1 wt.% of graphite), and half BP-ratio BP-G (50 wt. % of BP and 50 wt. % of graphite). It was reported the optimum composition of BP-C composite was 70 wt.% BP to 30 wt.% carbon (Super P), which is very close to $BP_{0.9}C_1$ [19]. Thus, BP-C composite was synthesized with the composition (70:30 wt%). Different from most other studies, a pristine graphite (Timrex SLP 30, Timcal) was used as the carbon element instead of carbon black (Super P) or mesoporous carbon. According to a previous study, it was suggested that ball-milled graphite is the most suitable material for BP-C composite compared with other types of carbon materials.

To reduce the particle size of BP-G and disperse agglomerated particles, we performed wet-ball-milling process after the HEMM synthesis of BP-G. The synthesized BP-G was wet-ball-milled at 3000 rpm for 30 min. with 15 EA of zirconium oxide balls (5 mm) and N-methyl-2-pyrrolidone (NMP) using a SpeedMixer (a dual asymmetric centrifuge-type mixer, FlackTek Inc.), before the slurry mixing procedure. For the same purpose, we also designed a multi-step ball-milling process that uses two different modes of milling (shaker mill and planetary mill). Before the BP-G synthesis by the HEMM, a planetary ball-milling (PBM) was applied to BP and graphite for 12 h (with 10 min. rest every 50 min.) in order to reduce the particle size. 3 g of graphite and 3 g of the synthesized BP were put into a stainless steel vial (100 mL), where the ball-to-power ratio was 50:1.

2.2.2 Battery Electrode Fabrication

To prepare the BP-based anodes, a slurry was prepared by mixing the synthesized material (either BP or BP-G, 80 wt%) with a polyvinylidene fluoride (PvdF, Kureha 7298) binder (10 wt%) dissolved in N-methyl-2-pyrrolidone (NMP) and Super P (10 wt%) at 3000 rpm for 30 min, using a SpeedMixer (DAC 150 FVZ double centrifugal mixer). The BP/G (mixture of BP and graphite) was prepared by mixing BP and graphite at 3000 rpm for 30 min. using the SpeedMixer. And the mixture of BP and graphite (80 wt.%) was finally mixed with PvdF binder (10 wt.%) and Super P (10 wt.%) using the same mixer. The viscosity of the final slurry was adjusted by the addition of NMP with 30 sec. of mixing at 3000 rpm after each addition. The resulting slurry was cast onto a

9 μm-thick copper (Cu) foil at a constant speed using a doctor-blade film coater (9 mils). The electrode was dried for 4 h in a vacuum oven at 110°C and dried overnight in vacuum conditions. This electrode-drying step should be performed carefully to prevent any reaction between the Cu foil and BP (more details are presented in the results section). The electrode was punched into disks (10 mm in diameter). The thickness of the electrode (without Cu foil) was in the range of 50 μm to 70 μm and the electrode loading (total weight of BP and graphite) was approximately 3.5–4.0 mg/cm^2. The electrode disks were stored in an Ar-filled glove box to avoid exposure to moisture. To prevent the BP-based electrode from oxidation or degradation, storage in an inert atmosphere was required.

2.2.3 Cell Fabrication/Electrochemical Tests/Post-mortem Analysis

2032-type coin cells were assembled in an Ar-filled glove box at moisture and oxygen levels below 0.1 ppm. The working electrode was assembled in a half-cell configuration with a Li foil counter/reference electrode (0.75 mm thick, 99.9%, Alfa Aesar) and a separator (Celgard 2320) soaked in an electrolyte solution. The electrolyte used for the cells was 1.0 M lithium hexafluorophosphate ($LiPF_6$) (Battery grade, <50 ppm HF, <15ppm H_2O, Sigma Aldrich) dissolved in a mixture (1:1, v/v) of ethylene carbonate (EC) and dimethyl carbonate (DMC). FEC (5 wt%) (99% fluoroethylene carbonate, Sigma-Aldrich) was added to the base electrolyte in an aluminum container in order to prepare the FEC-containing electrolyte.

The cells were cycled using a Maccor cycler between 0.01 V to 2V (vs. Li/Li+) with a constant current charge/discharge protocol. To compare the cycle performance of $BP_{0.3}G_1$ with that of $BP_{0.9}G_1$, either the same current density (200 mA/g, based on the total weight of BP and graphite) or a similar C-rate (~C/3 and ~C/7) was applied. Here, the C-rate was based on the theoretical capacity of each composite estimated by a simple mixing rule ($BP_{0.3}G_1$: 1352.24 mAh/g and $BP_{0.9}G_1$: 1929.7 mAh/g). The specific capacity was calculated based on the weight of either BP or BP-G. Electrochemical impedance spectra (EIS) was measured using a Biologic VMP3 with an EIS module. The frequency was scanned from 250 kHz to 25 mHz using 5 mV amplitude perturbation. Before the EIS test, the cell voltage was held at 1.0 V (vs. Li/Li+) for 2 h.

In post-mortem analysis, the cycled BP-based anodes were disassembled at the delithiated state (2.0 V vs. Li/Li+) in an Ar-filled glove box and washed with DMC to remove residual salts remaining on the electrode. The electrode was dried for more than 8 h and put onto a scanning electron microscopy (SEM) pin stub mount in the glove box. Then, it was placed in a vacuum-sealed bag for sample transportation. All samples were quickly inserted into the SEM instrument (less than 1 min.).

2.2.4 Material Characterization

X-ray diffraction (XRD) patterns of synthesized samples were obtained by a Rigaku rotating anode instrument with a Cu Kα radiation source (λ=1.541 Å). The XRD samples were prepared by grinding synthesized powder and then pressing the powder onto a glass substrate. The XRD patterns were collected over the 2θ range of 10 to 80° using a scan speed of 0.8 degrees per min and the increment set to 0.02 degree per step. SEM images were taken using a Phenom Pro (low-resolution images, accelerating voltage 10 kV) and a Philips XL30 FEG (high-resolution images, accelerating voltage 20 kV). Elemental analysis was performed using energy-dispersive X-ray spectroscopy equipped in the Philips XL30 FEG. Scanning transmission electron microscopy (STEM) was performed using a JEOL 3100R05 Double Cs Corrected TEM/SEM instrument operated at 200 kV. Raman spectroscopy characterization was conducted using a BWTEK i-Raman plus with a 532 nm excitation laser and a WITec alpha300 RA confocal Raman system with a laser wavelength of 532 nm. All Raman tests were performed at a low power level (approximately 2.5 mW) to avoid laser-introduced damage to the samples. To avoid any moisture effect, all samples were tested immediately after removal from the Ar-filled glove box. X-ray photoelectron spectroscopy (XPS) was conducted using a Kratos Axis Ultra X-ray photoelectron spectrometer equipped with a monochromatic Al Kα excitation source (hν = 1486.6 eV). The analyzed area was 300 x 700 μm2. The binding energy scale was calibrated from intrinsic hydrocarbon contamination using the C 1s peak at 285 eV. Core spectra were recorded with 20 eV constant pass energy. The fitting of core peaks was performed using the Shirley background correction and Gaussian-Lorentzian curve synthesis (70% Gaussian, 30% Lorentzian). Charge neutralization was used during measurements. Particle size distribution analysis was performed using a Saturn Digitizer 2 instrument (Micromeritics). Since the synthesized BP was hydrophobic, the BP was dispersed in NMP before adding it to the water in the system. BET surface area was measured using a Quantachrome Nova 4200 surface area analyzer. Electronic conductivity measurements were conducted using the four-point probe method. For conductivity measurements, BP/G and BP-G electrodes (80:10:10, active material:carbon black:PvdF wt%) were cast onto a glass plate. The electrode was dried at 110°C for more than 8 h in a vacuum oven. The large size of the electrode (around 18 x 8 cm2) was used to increase the accuracy of the measurement. For each electrode, measurements were conducted five times at different locations.

2.3 Results and Discussions

2.3.1 BP Synthesis and Characterization

The starting RP, an amorphous or low-range ordered structure, was successfully transformed to crystalline BP after the HEMM process. The XRD pattern in Figure 2.1 (a) of the synthesized BP showed a number of crystalline peaks, which was consistent with standard power diffraction data (JCPDS #01-073-1358). The synthesized BP was similar to those synthesized by other research groups [18, 19, 23, 24], except for one [25]. The phase change from RP to BP was completed after just 1 h of the HEMM process, which was consistent with a previous study [26]. In our study, 6 h of HEMM process was selected as an optimal time to synthesize BP considering the level of BP's crystallinity, time-saving, and the level of contamination. It should be noted that the achievable degree of crystallinity of BP by HEMM synthesis was limited. A further increase of ball-milling time did not help to improve the crystallinity of BP. Raman spectra in Figure 2.1 (b) also confirmed the phase transformation of RP to BP after 6 h of HEMM process. The synthesized BP showed three Raman active modes at 363, 438, and 467 cm, which indicates that BP had an orthorhombic phase rather than a rhombohedral phase or a cubic phase [27].

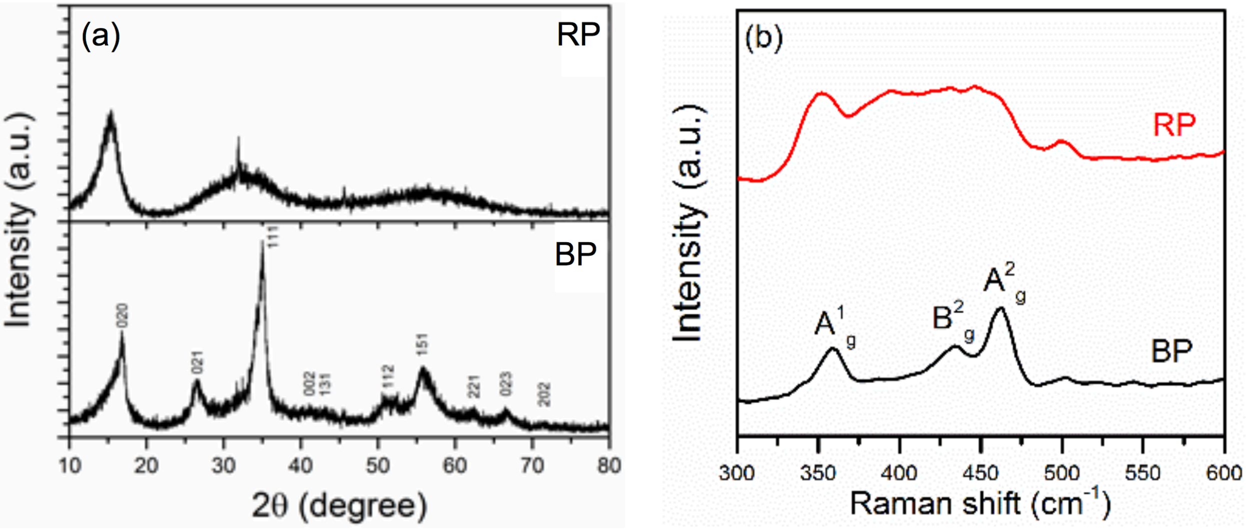

Figure 2.1 (a) XRD patterns and (b) Raman spectra of RP and BP after 6 h of the HEMM process.

A distinct difference in particle morphology was found between RP and BP in Figure 2.2. While the RP showed particles with sharp edges, the synthesized BP displayed round-shaped coarse-fine particles. The large RP particles (below 150 mm) were broken down into smaller pieces while the phase transformation occurred. The synthesized BP was agglomerated to form secondary particles in which fine particles adhere to each other due to particle interaction during the HEMM process. Ball-milled fine particles have a strong tendency to agglomerate owing to their relatively large specific surface area and other properties. The synthesized BP encompassed a wide range of particle sizes (75 nm-71 mm) and the median D50 value was 5.7 ± 1.7 mm, which was much smaller than RP. Note that only 20% of the particles were shown as nano-size and most were micron-size particles. The BET surface area of the synthesized BP was 7.156 m^2/g, which was similar to the surface area of graphite (approximately 7.5 m^2/g) used for this study.

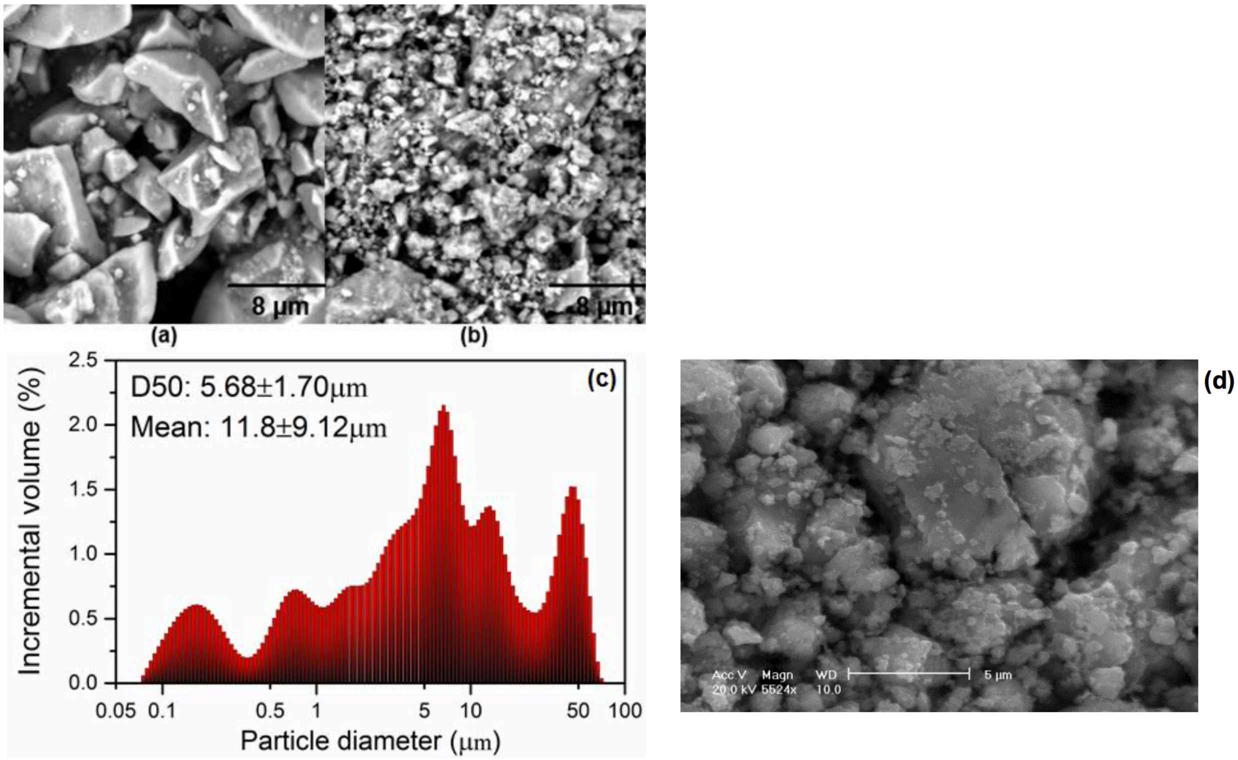

Figure 2.2 Low-resolution SEM images of (a) RP and (b) synthesized BP powder; (c) Particle size distribution and (d) high-resolution SEM image of the synthesized BP powder after 6 h of the HEMM process.

2.3.2 BP-G Composite Synthesis and Characterization

To understand the difference in material characteristics of $BP_{0.9}G_1$ and $BP_{0.3}G_1$, synthesized BP-G composite materials were systematically characterized. As expected, $BP_{0.3}G_1$ contained more carbon element than $BP_{0.9}G_1$ in Figure 2.3. Although relatively large particles were occasionally observed in $BP_{0.9}G_1$, there was no significant difference in the morphology and size of particles between $BP_{0.9}G_1$ and $BP_{0.3}G_1$ materials. Distinct differences between $BP_{0.9}G_1$ and

$BP_{0.3}G_1$ materials were observed in their crystal structures and chemical bonds, which will be demonstrated by the following Raman, XPS, and XRD results.

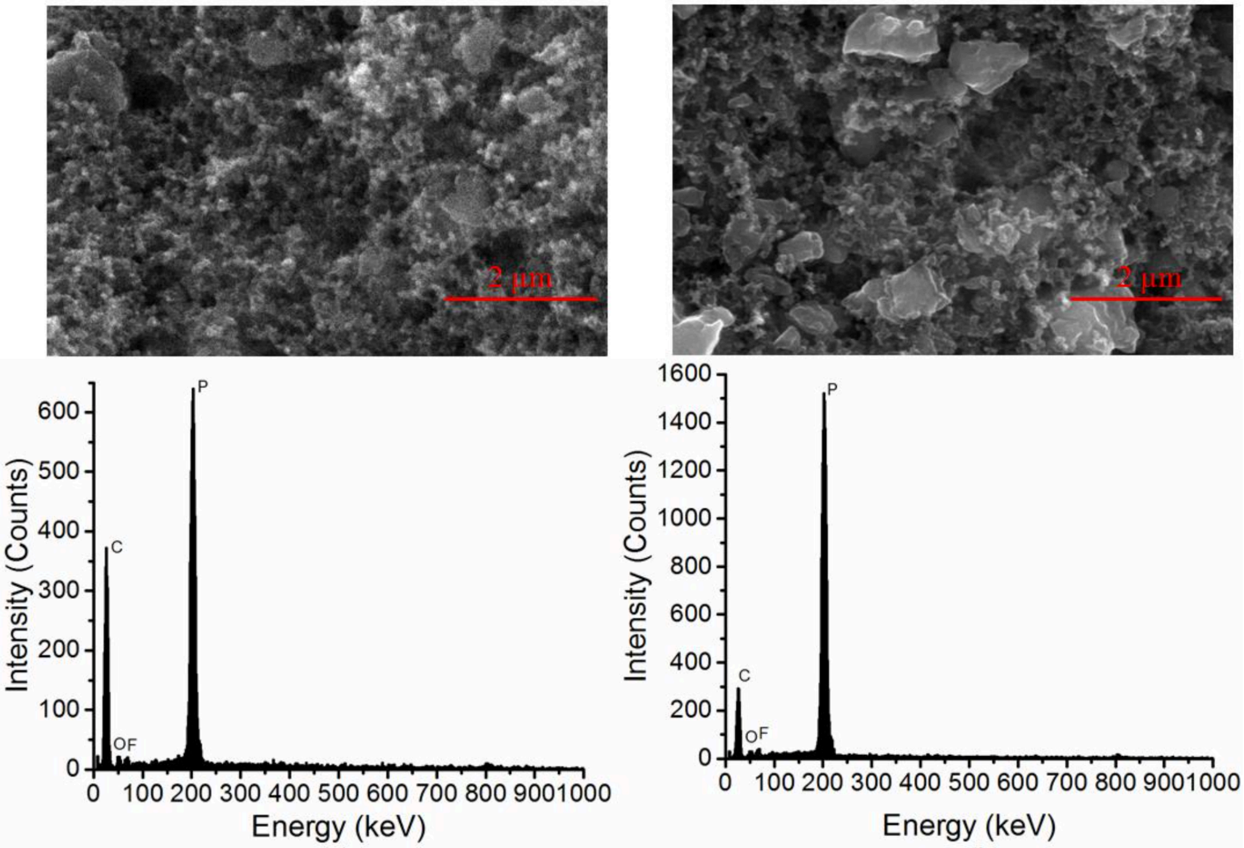

(a) (b)

Figure 2.3 SEM images of (a) $BP_{0.3}G_1$ and (b) $BP_{0.9}G_1$ electrodes before cycling and the corresponding EDAX spectra.

Figure 2.4 (a) shows the Raman spectra of pristine graphite and BP before the synthesis of BP-G composite. The synthesized BP powder displayed three Raman active modes at 363, 438, and 467 cm, while the pristine graphite showed two characteristic D and G bands near 1350 and 1580 cm, respectively. To characterize the extent of structural disorder in graphite, the peak intensity ratio I_D/ I_G has been typically used [28]. Pristine graphite showed the dominant G-band peak with respect to the D-band peak (low I_D/I_G ratio), indicating a highly ordered graphite structure without defects. In contrast, BP-G composites showed much higher peak intensity ratios of I_D/I_G (i.e., the dominant D-band with respect to the G-band). This indicates that severe structural disordering occurred in the graphite when BP-G composites were produced by the HEMM process. During the HEMM process, particles of the BP/G powder mixture are subject to high energetic impact and mechanochemistry effect. The mixture particles are flattened and crushed by the compressive forces due to the collision of the milling balls and cluster of particles are impacted repeatedly with high kinetic energy. This induces not only creation of severely disordered carbon and phosphorous but also strong chemical reactions between as-milled BP and graphite particles. It is commonly known that the reactivity of as-milled solid particles increases during the high-energy ball milling process.

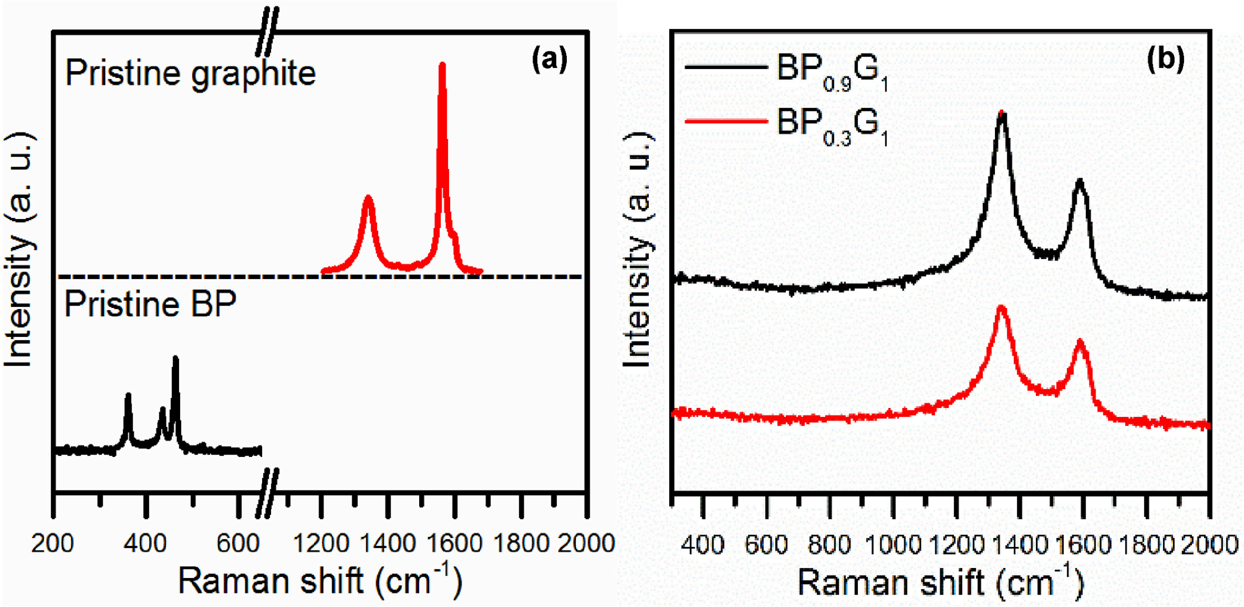

Figure 2.4. Raman spectra of (a) pristine graphite and BP powder; (b) BP-G composite powder ($BP_{0.9}G_1$ in black; $BP_{0.3}G_1$ in red).

It is important to point out that the observed structural disordering was not only due to the structural destruction of graphite. Interestingly, a higher intensity ratio of D-band to G-band was observed in $BP_{0.9}G_1$ (1.53) compared to $BP_{0.3}G_1$ (1.41) in Figure 2.4 (b). The difference in the degree of disordering indicates that the structure of $BP_{0.9}G_1$ could be different from $BP_{0.3}G_1$. $BP_{0.9}G_1$ had a more disordered carbon form or a less stable structure than $BP_{0.3}G_1$. The result suggests that BP-G composition determines the crystal structure of a BP-G composite, affecting the structural stability. A theoretical study was consistent with ours, supporting our finding [29].

Note that the BP-related signals (A^1_g, B^2_g and A^2_g) which represent P-P bond were no longer observed in both BP-G composites. There has been no agreement on the presence of BP Raman feature in BP-carbon composites. While Qian et al. [24] and Sun et al. [23] observed BP Raman feature in their composites, Kim et al. [30] and Ramireddy et al. [18] did not observe the feature. The absence of BP Raman signals in our BP-G composites might indicate that our BP-G has a composite structure similar to the phosphorous-carbon composites produced by Kim et al. and Ramireddy et al. [18]. Alternatively, the disappearance of BP-related Raman signals in BP-G composites might represent the breakup of P-P bonds in BP, creating P-C bonds in BP-G composites [23]. A previous study demonstrated that BP Raman signals in P/C composites were weakened and finally disappeared with increasing ball-milling time [24]. They explained that this is indicative of the strong interaction between phosphorus and carbon. Therefore, the synthesized $BP_{0.3}G_1$ and $BP_{0.9}G_1$ composites were believed to have the P-C bonds, which was further confirmed by the following XPS analysis.

As shown in Figure 2.5, the deconvoluted XPS spectra (P 2p) of BP, $BP_{0.9}G_1$ and $BP_{0.3}G_1$ powders were compared to understand the formation of P-C bonds in BP-G composites. While BP powder exhibited only a P-P bond (129.9 eV and 130.8 eV assigned to $2p_{3/2}$ and $2p_{1/2}$, respectively), BP-G composites showed the co-existence of both a P-P bond and P-C bond (130.2 eV and 131.1 eV assigned to $2p_{3/2}$ and $2p_{1/2}$, respectively). The content (47.7%) of the P-C bond in the $BP_{0.3}G_1$ was much higher than that (17.1%) of the $BP_{0.9}G_1$. This suggests that more P-C bond formation existed in the structure of $BP_{0.3}G_1$ than $BP_{0.9}G_1$. It means that a different BP-G crystal structure with different chemical P-C bonds was formed depending on BP:G stoichiometry.

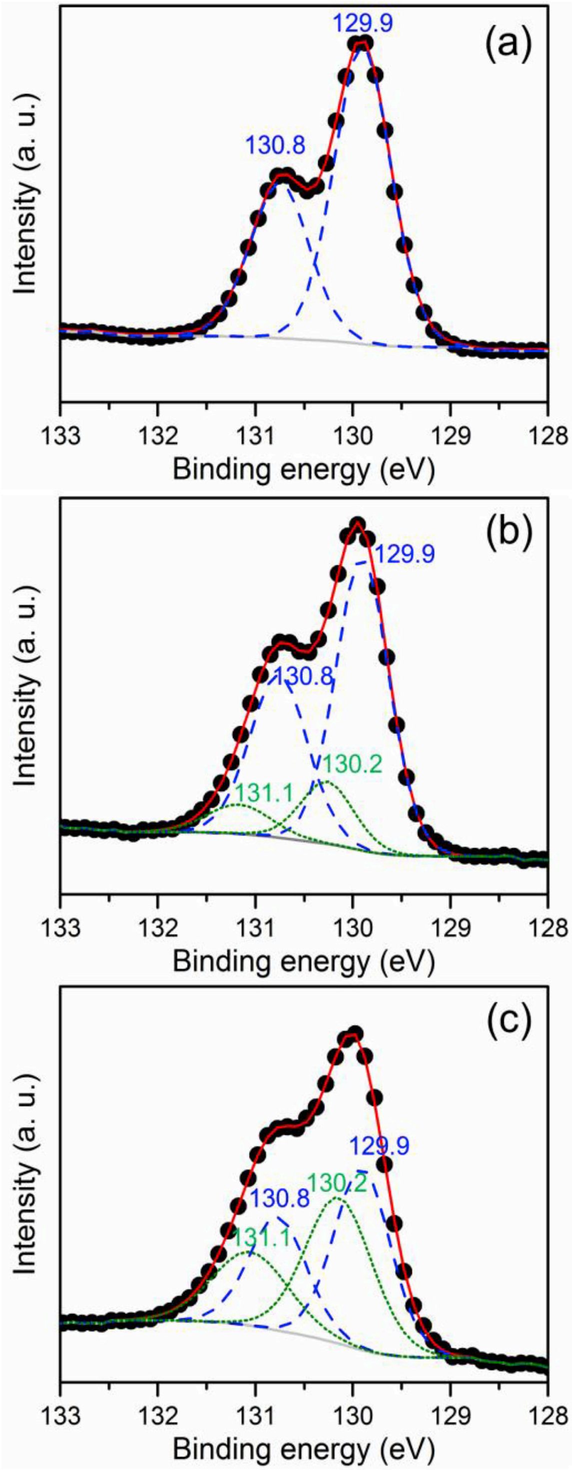

Figure 2.5. Comparison of XPS spectra (P 2p) of (a) BP, (b) BP$_{0.9}$G$_1$, and (c) BP$_{0.3}$G$_1$ powders. Black dots, red solid lines, blue dashed lines, and green dashed lines represent the measurement data, the fitted XPS spectra, PP bond doublets, and PC bond doublets, respectively.

Based on our Raman and XPS analysis, the crystal structure of $BP_{0.3}G_1$ had a less disordered carbon form and consisted of more formation of P-C bonds than $BP_{0.9}G_1$. The structure of $BP_{0.3}G_1$ might be more robust in terms of structural stability than $BP_{0.9}G_1$. This could be closely related to the mechanical degradation/failure of BP-G composites.

According to previous density functional theory (DFT) calculation studies [29, 31, 32], there is preferred local bonding environment of carbon and phosphorus, and it is dependent on phosphorus/carbon composition. For instance, when phosphorus content is low in phosphorus carbide, the preferred type of structure is phosphorus-doped graphite [32]. In addition, formation of phosphorus carbides typically requires a significant number of weak P-P bonds. This reasonably explains why P-P bonds (or BP Raman signals) were not shown in BP-G composites. Our experimental results and the DFT predictions suggest that the synthesized BP-G composites had structures with P-C bonds but weak P-P bonds.

The crystal structural difference between $BP_{0.3}G_1$ and $BP_{0.9}G_1$ was further investigated by XRD analysis, as shown in Figure 2.6. In the XRD pattern of $BP_{0.3}G_1$, the characteristic peaks related to orthorhombic BP (such as (020), (021), and (111) reflections) almost disappeared, which was due to the breakup of P-P bonds in BP and the creation of P-C bonds in $BP_{0.3}G_1$. Although the intensities of the characteristic peaks related to graphite, such as (002) and (101) reflections, marked as downside triangles in blue, were significantly diminished and broadened, these characteristic peaks remained. Moreover, these peaks shifted to lower 2q angles with respect to the original (002) and (101) reflections. The decrease in the intensity of BP-related diffraction peaks and the shift of graphite-related peaks ((002) and (101) reflection) observed in $BP_{0.3}G_1$ might be attributed to the formation of new BP-G composite structure with P-C bonds.

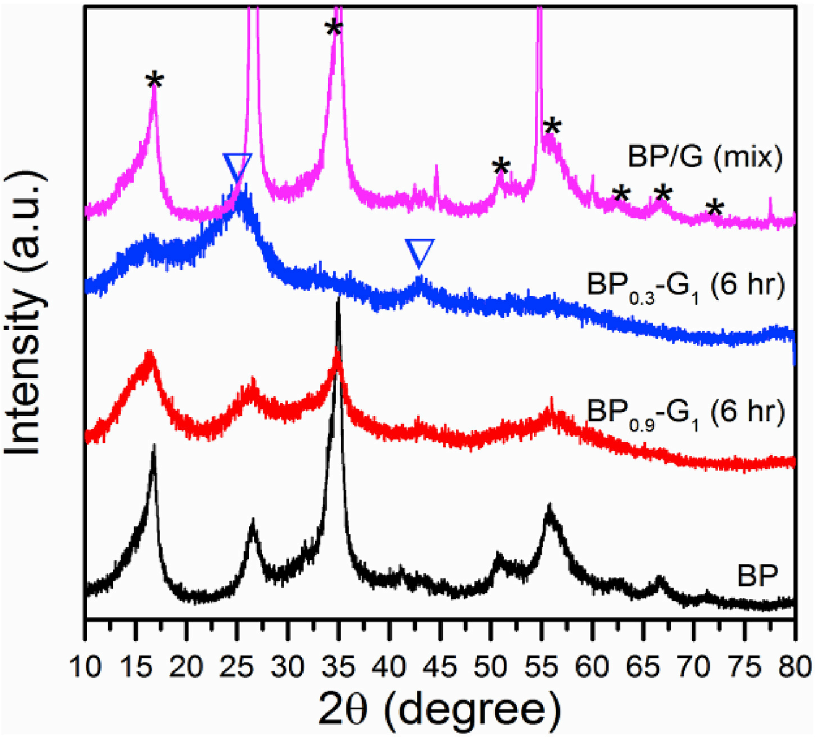

Figure 2.6 XRD patterns of BP, BP-G composites ($BP_{0.9}G_1$ in red; $BP_{0.3}G_1$ in blue), and BP/G mixture (44:56 wt %). (For interpretation of the references to colour in this figure legend, the reader is referred to the Web version of this article.)

In contrast, $BP_{0.9}G_1$ showed a different XRD pattern. The XRD pattern of $BP_{0.9}G_1$ still displayed the characteristic peaks related to BP but graphite-related diffraction peaks were relatively negligible. Thus, a different XRD pattern of $BP_{0.3}G_1$ compared with $BP_{0.9}G_1$ indicates $BP_{0.3}G_1$ had a different type of structure compared with the structure of $BP_{0.9}G_1$.

In summary, $BP_{0.3}G_1$ had an amorphous-type structure with robust P-C bonds, while $BP_{0.9}G_1$ had a medium-range ordered structure with fewer or weaker P-C bonds. It was speculated that $BP_{0.9}G_1$ was more brittle than $BP_{0.3}G_1$ since $BP_{0.9}G_1$ still retained the BP feature and BP was much harder than graphite. The amorphous- like structure with robust P-C bonds (i.e., $BP_{0.3}G_1$) could withstand large volume expansion during lithiation/delithiation, preventing any cracking or fracture. This is demonstrated in the next section.

The difference in crystal structure of $BP_{0.3}G_1$ and $BP_{0.9}G_1$ was further confirmed by the difference in their electrical conductivity. As shown in Figure 2.7, the $BP_{0.3}G_1$ electrode (1.6×10^1

S/cm) showed approximately two times greater electrical conductivity than the $BP_{0.9}G_1$ electrode (8.9×10^2 S/cm). The structure type of $BP_{0.3}G_1$, which is close to phosphorus-doped graphite structure, is likely to have greater electrical conductivity than other types of phosphorus-carbon structures because it retains the original graphite or graphene-like structure to some extent [32]. Thus, the difference in electrical conductivity between $BP_{0.3}G_1$ and $BP_{0.9}G_1$ might originate from their structural difference. It should also be mentioned that BP/G mixtures showed much greater electrical conductivity than the corresponding BP-G composites. BP/G (70:30 wt%) and BP/G (44:56 wt%) mixtures exhibited 1.4 and 4.9 S/cm, respectively. This indicates that BP and graphite were chemically bonded during the HEMM process, creating BP-G composites with completely different characteristics compared to BP or graphite.

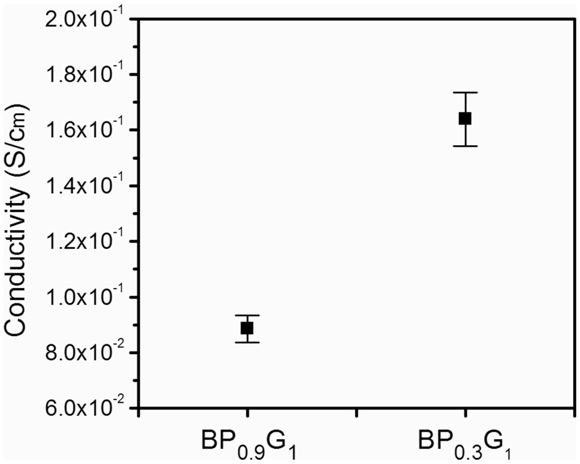

Figure 2.7 Comparison of electrical conductivity of $BP_{0.9}G_1$ and $BP_{0.3}G_1$.

Based on the above results, we conclude that $BP_{0.9}G_1$ exhibits a medium-range ordered structure which retains the original BP features somewhat and consists of weak P-C bonds. In contrast, $BP_{0.3}G_1$ has an amorphous and phosphorus-doped graphite-like structure with strong P-C bonds. In the section 2.2.3, we demonstrate how the difference in the structural characteristics of BP-G composites caused by BP-G molar ratio is directly correlated to the difference in their electrochemical performance.

2.3.3 Cycling Performance of BP-G Composite and Its Degradation Mechanism

To better understand the BP-G composite material, electrochemical performance was compared for BP/G (70:30wt%) mixture, 1 h-HEMM and 6 h-HEMM synthesized $BP_{0.9}G_1$ composites. Figure 2.8 shows the galvanostatic discharge-charge profiles of BP/G, 1 h-HEMM $BP_{0.9}G_1$, and 6 h-HEMM $BP_{0.9}G_1$ at the 1st cycle. Compared with the BP/G mixture, the first discharge capacity and cycle coulombic efficiency of 1 h-HEMM $BP_{0.9}G_1$ and 6 h-HEMM $BP_{0.9}G_1$ were significantly improved. The first discharge capacity of the BP/G mixture was 571 mAh/g, showing the first-cycle efficiency of only 16.1%. This indicates that a large portion of BP particles in the BP/G mixture did not participate in electrochemical reaction. Note that the electrical conductivity of BP/G mixture was much greater than the corresponding BP-G composite. This means that increasing electrical conductivity at the electrode level does not necessarily help making more BP particles to participate in electrochemical reaction.

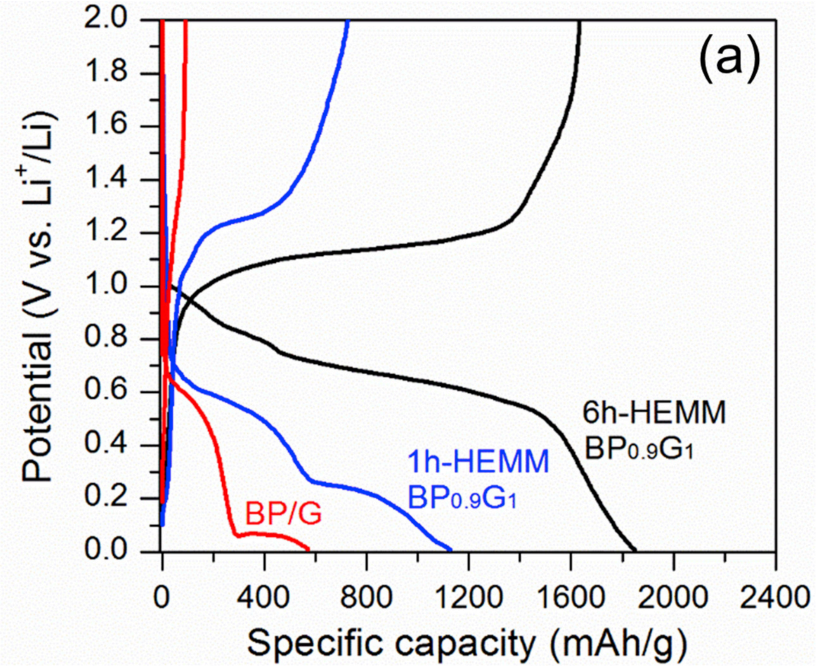

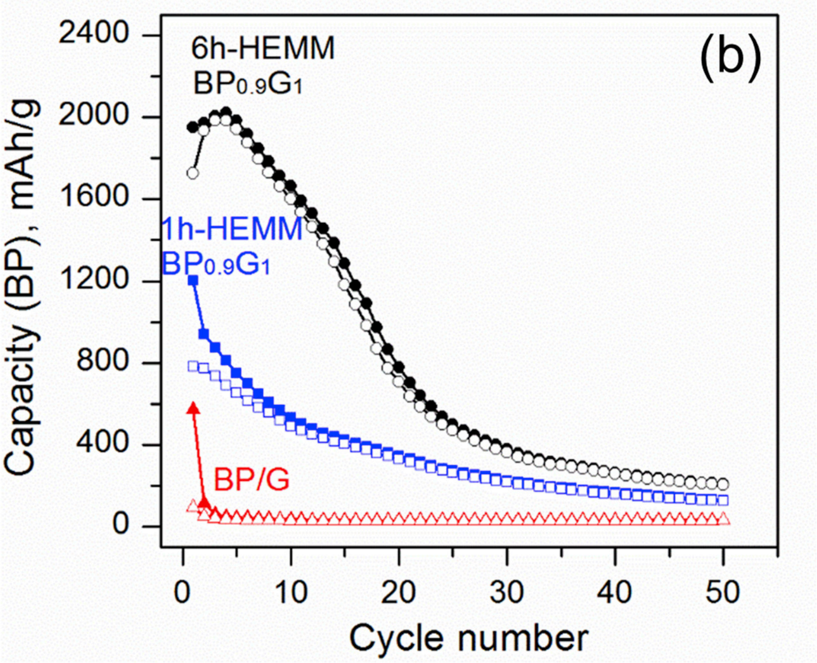

Figure 2.8 (a) Galvanostatic discharge-charge profiles and (b) cycle performance of BP/G (70:30 wt%) mixture (red), 1 h-HEMM $BP_{0.9}G_1$(blue), and 6 h-HEMM $BP_{0.9}G_1$ (black). Half-cells were cycled at a current density of 200 mA/g. Here, the capacity was calculated based on the weight of BP. Close and open symbols represent discharge and charge capacity, respectively.

Once BP and graphite were chemically bonded during the HEMM process to form a BP-G composite, the electrochemical performance was significantly enhanced. The first discharge capacity of 1 h-HEMM $BP_{0.9}G_1$ was 1126 mAh/g, showing a first-cycle efficiency of 64.5%. With increasing ball-milling time (6 h), the first discharge capacity of $BP_{0.9}G_1$ increased up to 1847 mAh/g, showing a first-cycle efficiency of 88.5%. The HEMM process contributed to increasing electrical conductivity of BP at the particle level by creating the BP-G composite. As a result, the enhanced electrochemical performance of $BP_{0.9}G_1$ was observed.

Although $BP_{0.9}G_1$ achieved a high discharge capacity and coulombic efficiency, severe capacity fade was still observed, as shown in Figure 2.8 (b). The reversible capacity rapidly dropped within 30 cycles. The rapid capacity fade was consistent with a previous study, in which a different type of mill (either a planetary ball mill or magneto-ball bill) was used for synthesizing the $BP_{0.9}G_1$ composite [18]. Thus, the rapid capacity fade observed in $BP_{0.9}G_1$ might not be a synthesis issue but be an intrinsic material issue. As far as graphite is used as a carbon source for synthesizing phosphorus- carbon composite with 70 wt% of BP, the composite cannot avoid fast capacity fade. This might be correlated with the structural characteristics of $BP_{0.9}G_1$. The $BP_{0.9}G_1$, which exhibited a medium-range order structure with fewer and weaker P-C bonds, might be inherently vulnerable to large volume change during lithiation or delithiation, resulting in cracking and crumbling of BP-G particles.

As shown in Figure 2.9, the mechanical degradation of $BP_{0.9}G_1$ was responsible for the fast capacity fade. A number of fractured particles (marked with red arrows) were clearly found in the $BP_{0.9}G_1$ electrode after 50 cycles. The mechanical degradation (cracking, crumbling, and pulverization) of $BP_{0.9}G_1$ caused loss of electrical contact of active materials, thereby resulting in a rapid capacity fade. Note that the fractured particles were noticeably observed to be those with a relatively large size of 5-20 mm. This might be the reason why previous studies could not report any evidence of mechanical failure in the phosphorus-carbon composite. Since most previous studies have tried to confine nano-size phosphorous into a carbon matrix, it was difficult to characterize any possible fractures or cracks of the nano-size particles, although it is highly likely to happen. Alternatively, similar to the widely studied Si anodes, nano-size particles were likely to have less mechanical stress than micron-size particles upon cycling, thereby mitigating severe fracturing. The decrease of Si particle size to the nano-range has been known as an effective way to relieve any mechanical stress during a large volume expansion/contraction [33]. To the best of our knowledge, our study is the first report demonstrating direct evidence of mechanical failure of BP-G anodes.

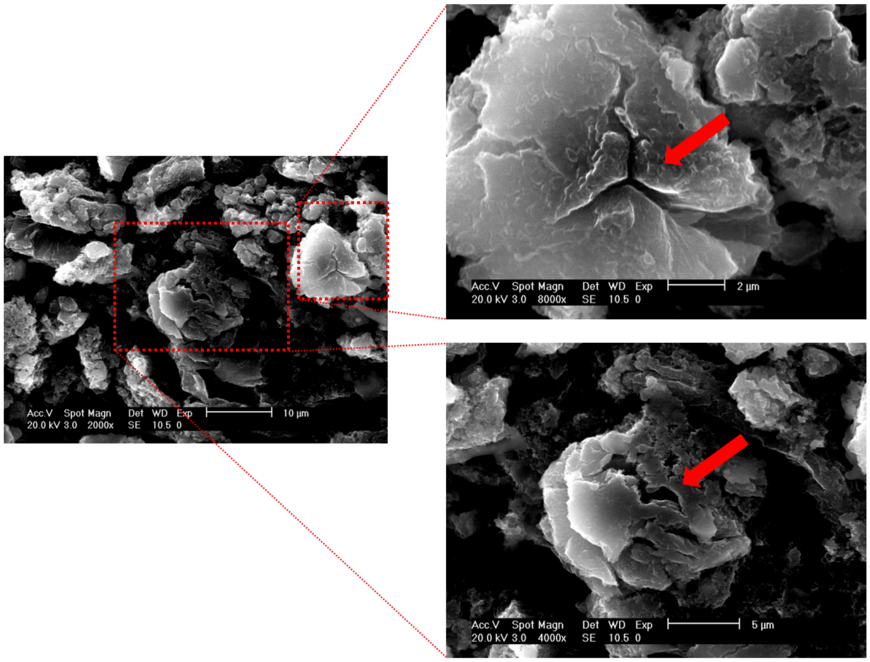

Figure 2.9 SEM images of particle cracks observed in $BP_{0.9}G_1$ after 50 cycles.

Interestingly, cycle performance of BP-G composite was noticeably improved with a different BP-G composition ($BP_{0.3}G_1$). As shown in Figure 2.10, $BP_{0.3}G_1$ showed much better cycle performance than $BP_{0.9}G_1$.

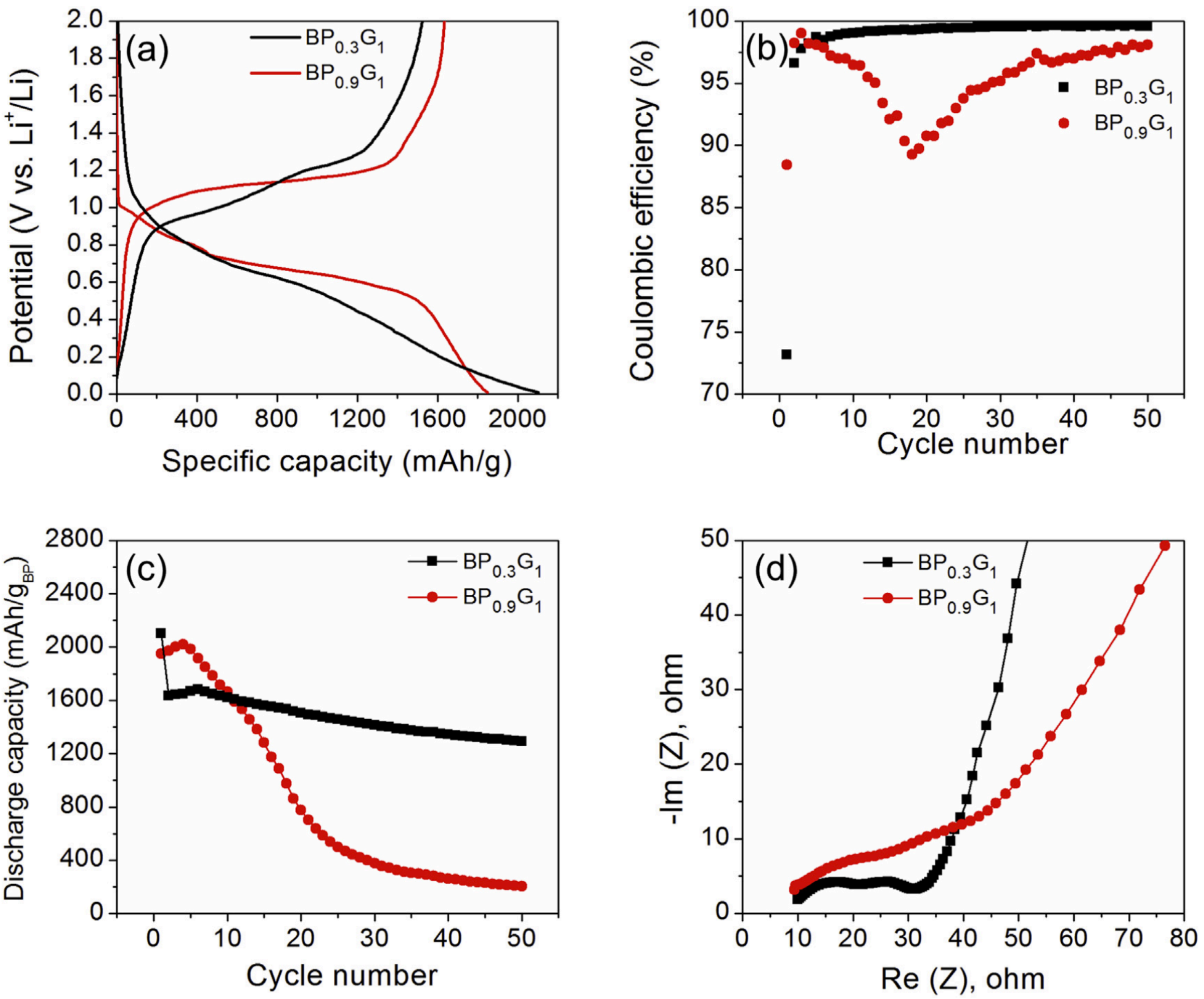

Figure 2.10 Comparisons of (a) the 1st cycle discharge-charge profile, (b) coulombic efficiency, (c) cycle performance, and (d) EIS spectra after 50 cycles between BP0.3G1 (black) and BP0.9G1 (red). Half-cells (BP-G vs. Li) were cycled at a current density of 200 mA/g (based on total weight of BP and graphite).

The excellent cycle stability of $BP_{0.3}G_1$ was attributed to the mechanical stability of $BP_{0.3}G_1$ electrode upon cycling. As shown in Figure 2.11, the $BP_{0.3}G_1$ electrode maintained its structural integrity after 50 cycles. This means that the $BP_{0.3}G_1$ electrode endured the large volume change while retaining electrical contact between particles. In the cycled $BP_{0.3}G_1$ electrode, cracks in particles or fractured particles were rarely observed in Figure 2.11 (a). The cross-sectional SEM image Figure 2.11 (c) also revealed that no structural disruption was found in the electrode. In contrast, the $BP_{0.9}G_1$ electrode showed severe mechanical failure at both the particle and electrode level. Cracking of $BP_{0.9}G_1$ particles was considerably found everywhere, and the pulverization of BP-G particles was also observed in Figure 2.11 (b). As a result, the $BP_{0.9}G_1$ electrode was damaged and its structural integrity was not maintained after cycling in Figure 2.11 (d). The mechanical fracture and pulverization led to considerable loss of active materials, followed by loss of electrical contact between active materials. This was confirmed by comparing the EIS spectra of $BP_{0.9}G_1$ and $BP_{0.3}G_1$ after 50 cycles.

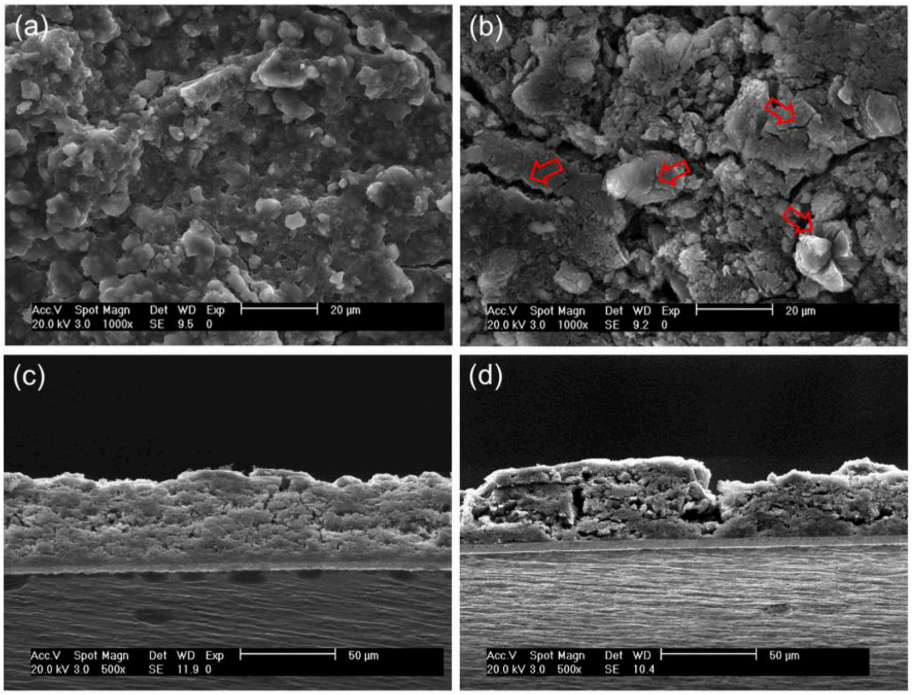

Figure 2.11 Top-view and cross-sectional SEM images of (a) (c) $BP_{0.3}G_1$ and (b) (d) $BP_{0.9}G_1$ electrodes after 50 cycles.

To further analyze the difference in electrochemical reactions, discharge-charge and the corresponding differential capacity curves of $BP_{0.9}G_1$ were compared with those of $BP_{0.3}G_1$, as shown in Figure 2.12. During the first discharge, $BP_{0.9}G_1$ showed several cathodic peaks near 1.0, 0.8, 0.7, and 0.5 V, which correspond to SEI formation (0.8 V) and lithiation-related reactions (0.7 and 0.5 V). The origin of the peak at near 1.0 V was not clear, which was not seen in $BP_{0.3}G_1$, and it disappeared after the first cycle. It could correspond to formation of irreversible Li_xP. Alternatively, several cathodic peaks could be related to lithiation reactions coupled with side reactions induced by particle fracturing and cracking. Note that the peak related to SEI formation (0.8 V, marked with asterisk) was still present during the 3rd cycle, which was different from the case of $BP_{0.3}G_1$. This indicates that additional SEI formation occurred in $BP_{0.9}G_1$ during the 3rd cycle due to newly exposed surface areas of fractured and cracked $BP_{0.9}G_1$ particles. During the 1st and 3rd discharge, $BP_{0.9}G_1$ showed only one anodic peak at 1.1 V, which corresponded to delithiation reaction. During the 25th cycle, the anodic and cathodic peaks were greatly diminished and shifted to the higher and lower voltages, respectively, indicating little lithiation/delithiation and large polarization. In contrast, $BP_{0.3}G_1$ showed only one lithiation-related cathodic peak at near 0.7 V and two delithiation-related anodic peaks at near 1.0 and 1.2 V. The intensity and position of lithiation/delithiation-related peaks remained relatively well during 25 cycles. The SEI formation- related peak at 0.8 V (marked with asterisk) disappeared after the 1st cycle, demonstrating no severe fractures and cracks occurred in $BP_{0.3}G_1$.

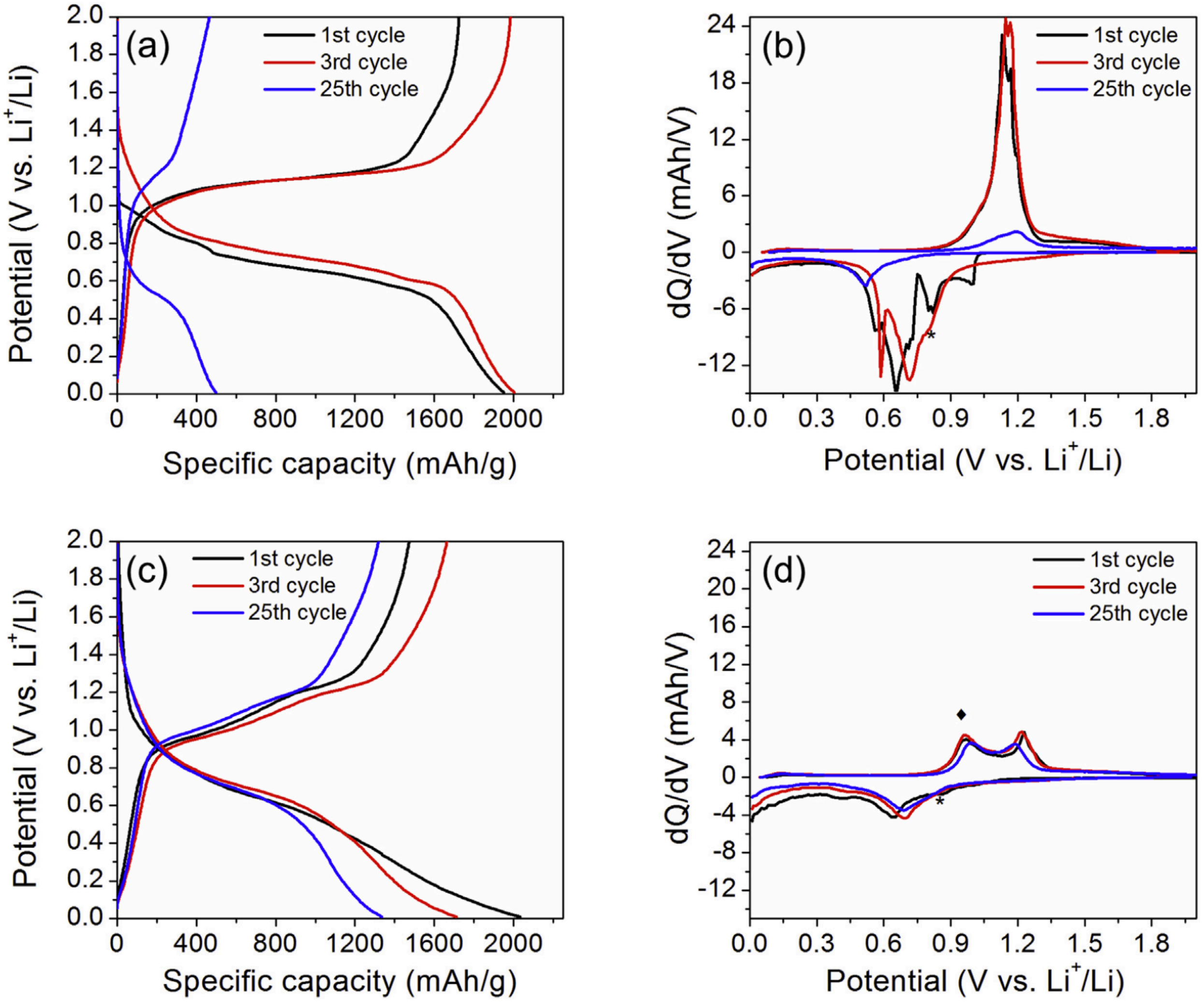

Figure 2.12 Galvanostatic discharge-charge profiles and the corresponding differential capacity plots of (a) (b) $BP_{0.9}G_1$ and (c) (d) $BP_{0.3}G_1$ at the 1st, 3rd, and 25th cycle.

The distinct difference in the differential capacity curves suggests that the lithiation/delithiation process of $BP_{0.3}G_1$ is considerably different from $BP_{0.9}G_1$. In particular, it is apparent that the delithiation mechanism of $BP_{0.3}G_1$ (two anodic reactions) is different from $BP_{0.9}G_1$ (one anodic reaction). This could be attributed to the difference in crystal structure of $BP_{0.3}G_1$ and $BP_{0.9}G_1$. $BP_{0.3}G_1$, having an amorphous type of structure with a lot of robust P-C bonds, could cause a unique lithiation/delithiation mechanism that avoids particle fracturing and cracking. Alternatively, it might be a suitable structure form that withstands the large volume change upon cycling. Note that BP suffers from a huge size increase and cracking during delithiation process, not lithiation process [34]. The two-step delithiation process observed in $BP_{0.3}G_1$ may mitigate delithiation-induced stress since the stress is distributed through two electrochemical reaction steps. However, we cannot rule out the possibility that the extra graphite used in $BP_{0.3}G_1$ might act as a flexible buffer matrix during cycling. The extra graphite might allow BP-G microparticles to expand and fractured nanoparticles to anchor while retaining electrical connectivity at both the particle and electrode level [35].

The next synthetic approach we used was to incorporate a solvent-free planetary ball milling (PBM) prior to shaker/mixer milling (HEMM). While a shaker/mixer mill provides efficient impact interactions for mechanochemical reactions due to its “breaking” mode, wherein the impact of balls on the particle is dominated by normal collision forces, a planetary-type mill is effective in reducing particle size during its “peeling” mode caused by dominant shear forces. By combining these two processes (PBM + HEMM), nano- and submicron-sized BP-G particles are produced while preserving the strong connections between phosphorus and carbon.

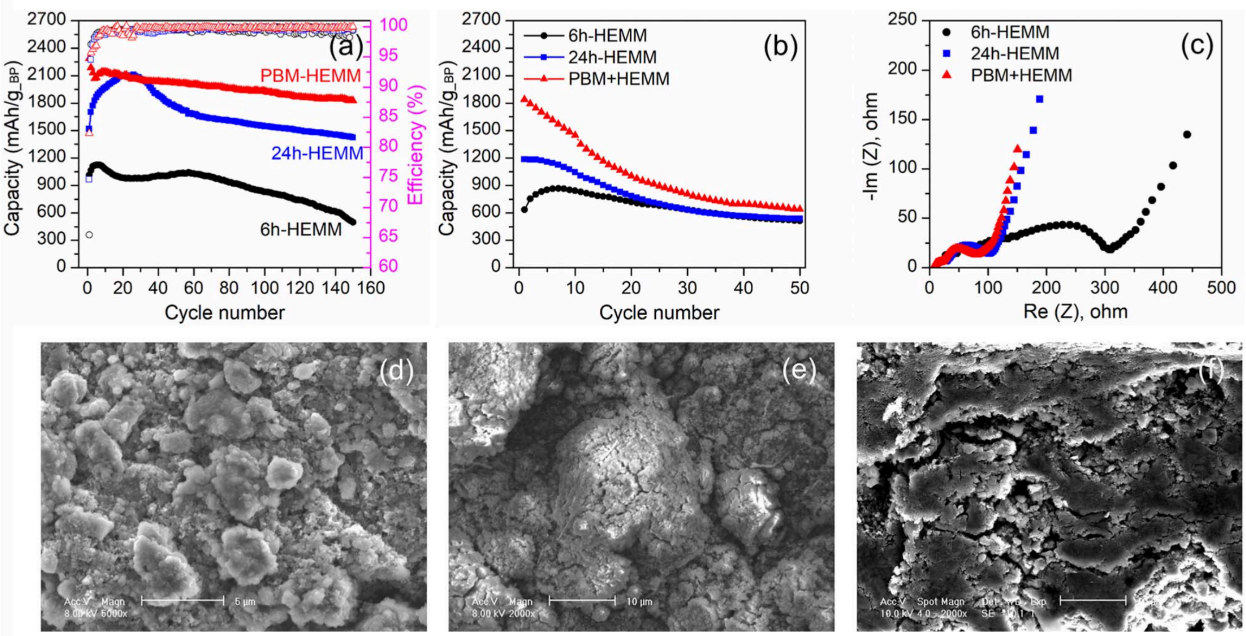

Figure 2.13 Cycle performance of BP-G (50:50 wt%) electrodes synthesized with different processes. The cells were cycled with FEC additive between 2.0 – 0.01 V (vs. Li^+/Li) with a current density of either (a) 100 mA/g or (b) 1000 mA/g. The capacity is charge (delithiation) capacity, which is based on the weight of BP. Open symbol corresponding to coulombic efficiency is

displayed in the right axis. The active material (BP + G) loading was between 1.1 to 1.5 mg/cm^2. (c) EIS spectra of 6h-HEMM, 24h-HEMM and PBM + HEMM processed BP-G (50:50 wt%) electrodes after 150th cycles. Top-view SEM images of PBM + HEMM processed BP-Gs are shown after the 150th cycle at (d) 100 mA/g and (e) 1000 mA/g, respectively. (f) Cross-sectional SEM image of PBM + HEMM processed BP-G after the 150th cycle at 1000 mA/g.

As shown in Figure 2.13 (a), the multi-step ball milling (PBM + HEMM) approach significantly affected the cycle performances of BP-G composites. BP-G composites synthesized by PBM + HEMM showed excellent reversible capacity (2,285 mAh/g after 1 cycle) and superior cycling stability, with a capacity retention of 80% over 150 cycles (1,827 mAh/g at the 150th cycle) compared to other BP-G composites (6h-HEMM and 24h-HEMM). This synthesis protocol produced active material loadings similar to one another, preventing active material loading effects on cycle performance. In addition, the first cycle coulombic efficiency (82%) was significantly higher for the multi-step protocol than for the HEMM-only processes (6h-HEMM BP-G: 65%, 24h-HEMM BP-G: 75%). However, these improvements were only observed upon combining PBM with HEMM. No improvements were observed when PBM or HEMM alone was used for BP-G synthesis.

Improvements in BP-G cyclability and reversible capacity by PBM + HEMM process are attributed to the combined effect of reduced particle size and robust connections between phosphorus and carbon. While the PBM step reduced particle size, the HEMM process was essential to facilitating strong connections between phosphorus and carbon due to its dominant impact interaction mode. The multi-step protocol was thereby able to mitigate volume-change induced cracking or pulverization of BP-G particles and subsequent electrolyte decomposition successfully. As demonstrated in the SEM image (Figure 2.13 (d)), no obvious particle cracking or pulverization was observed, and the structural integrity of the electrode was well maintained after 150 cycles. The improved cycle performance of the PBM + HEMM sample was further investigated by comparing the EIS spectra of three samples, 6h-HEMM, 24h-HEMM, and PBM +

HEMM, as shown in Figure 2.13 (c). The equivalent circuit model described in Figure S 5 was used to fit the EIS spectra. Based on fitting results, R_{SEI} and R_{ct} of the PBM + HEMM sample after 150 cycles were 15 and 61 , respectively, lower than those for both 6h-HEMM (R_{SEI}: 48 and R_{ct} : 201) and 24h-HEMM (R_{SEI} : 20 , R_{ct} : 72) samples. This demonstrates that the PBM + HEMM sample did not experience significant electrolyte decomposition followed by SEI growth, while the 6h-HEMM and 24-HEMM samples did.

However, the PBM + HEMM sample was not robust enough to withstand high C-rates. As shown in Figure 2.13 (b), the sample exhibited a rapid capacity fade at a high current density of 1000 mA/g (roughly close to 1C rate) similar to 6h-HEMM and 24-HEMM samples. This indicates that even PBM + HEMM samples cannot avoid mechanical degradation followed by side reactions when they are subjected to high C-rates. As shown in Figure 2.13 (e)(f), particle-level degradation such as cracking, and electrode-level degradation such as delamination, were both observed in PBM + HEMM samples after 150 cycles at a high C-rate. This is because high current density severely disrupts current distribution homogeneity, eventually resulting in uneven expansion/contraction and local stress concentration on BP-G particles. The PBM + HEMM sample did, however, show higher initial reversible capacity at 1000 mA/g than the other samples, with the initial reversible capacity at 1000 mA/g only slightly lower than that at 100 mA/g.

2.4 Summary

We have systematically investigated the difference between BP-G composite with a high ratio of BP ($BP_{0.9}G_1$) and BP-G composite with a low ratio of BP ($BP_{0.3}G_1$) to understand the correlation between material property and electrochemical performance. The results demonstrate the significance of BP-G composition for achieving cycle stability of the BP-G composite. We found that the crystal structure and P-C bonds of BP-G composites are affected by BP:G molar ratio, which determines the structural integrity of BP-G composites. $BP_{0.3}G_1$ composite has a structurally-stable crystal structure with considerable P-C bonds, which is beneficial for withstanding the large volume change during cycling. Moreover, it results in a different lithiation/delithiation mechanism during cycling. As a result, stable cycle performance can be achieved with the $BP_{0.3}G_1$ composite. In contrast, $BP_{0.9}G_1$ composite cannot avoid fast capacity fade mainly caused by the fracture and pulverization during cycling because it has less structural stability than $BP_{0.3}G_1$. The difference in the structural characteristics of BP-G composites caused by BP-G molar ratio is directly correlated to the differences in their electrochemical performance and lithiation/delithiation mechanism.

We compare the influence of FEC additive, HEMM synthesis parameters, and electrode loading in Appendix 1-4. Results suggest that the cycle stability of BP-G composites is most significantly affected by material composition and electrode loading (material composition >electrode loading >FEC additive >ball milling time), while first cycle efficiency and reversible capacity are more dependent on ball milling time and material composition (ball milling time >material composition >electrode loading ≈ FEC additive). Further improvements in cycle stability can be achieved by optimizing the HEMM synthesis process. While BP-G composition is critical for cycle stability, ball milling time strongly affects the activation of BP in BP-G composites. It is important to optimize HEMM synthesis times accordingly to achieve a high reversible capacity in BP-G composite.

With these findings, an optimized BP-G synthesis approach that employs a combination of shaker-type and planetary-type ball milling modes is proposed. This approach yielded improved electrochemical performance of BP-G composite, with excellent reversible capacity (2,285 mAh/g) and superior cycle performance (capacity retention of 80% over 150 cycles). Despite these strides forward, however, alternate strategies to HEMM-based synthetic routes will be necessary to design BP-G composites with high C-rate capabilities.

We suggest other possible mechanisms underlying capacity degradation of BP-based anode materials. Both highly hydrophilic nature of BP upon oxidation and formation of Cu_3P phase on Cu current collector might contribute to additional structural instability of BP-based electrodes.

This work provides a better understanding of black phosphorus-graphite composite materials and its dependence on various factors. It illuminates potential causes for the significant differences in P-C electrochemical performance reported in the literature. It also reveals correlations between HEMM synthesis processes and the electrochemical performance of BP-G composites, providing useful guidelines for developing better BP-based anode materials using HEMM synthesis in the future.

Chapter 3

Pulse Laser Assisted Liquid Phase Exfoliation of Phosphorene with Improved Ambient Stability

3.1 Introduction

Black phosphorus (BP) is the most thermodynamically stable phosphorus allotrope, from both experimental and quantum chemical perspectives. It can be synthesized by the high pressure method, chemical vapor deposition (CVD) and mineralization. Phosphorene, a two-dimensional monolayer or few-layer BP, has recently attracted attention due to its unique structure containing puckered individual layers connected by weak van der Waals forces, as well as superior electronic and optoelectronic properties. Phosphorene possesses wide and tunable bandgaps from 0.3 eV to 1.5 eV in an inverse relationship to its thickness. This property makes phosphorene a promising material for use in digital devices alongside graphene and other transition metal materials. In addition, a high carrier mobility (286–1000 $cm^2 \cdot V^{-1} \cdot s^{-1}$), anisotropic in-plane transport properties and a high on–off current ratio (10^2–10^5) render phosphorene a suitable channel material for field effect transistors. BP and phosphorene are both promising candidates for use as high-capacity anode materials (2596 $mA \cdot h \cdot g^{-1}$) for lithium-ion battery applications, whose capacity is much higher than that of the commonly used graphite (372 $mA \cdot h \cdot g^{-1}$). It is of importance to note that both materials can be used in sodium-ion (Na-ion) batteries, where graphite is not applicable. Similar to other high-capacity anode materials such as silicon, however, BP-based Li-ion/Na-ion batteries suffer from rapid capacity fade, mainly owing to large volume expansion and subsequent structural failure. According to in situ transmission electron microscopy (TEM) studies, phosphorene is more robust during lithiation/delithiation or sodiation/desodiation in comparison to bulk BP particles [21, 36]. Thus, phosphorene-based anode materials have been proposed to mitigate significant volume expansion and contraction (370% in a Li-ion battery, 500% in a Na-ion battery) [37].

Multiple strategies have been used to exfoliate phosphorene. Mechanical cleavage through scotch-tape produces the highest quality samples, but productivity is low. Liquid-phase exfoliation assisted by ion intercalation, ultra-sonication and shear force is a more scalable process. An appropriate processing time, power and centrifugation parameters are necessary to control phosphorene thickness and size distribution [38, 39].

Unfortunately, phosphorene is known for its fast degradation within hours of exposure to ambient environments [40], especially when oxygen, moisture and light are involved together [41-43]. Significant compositional and structural changes will result in a loss of phosphorene's electronic and physical properties. Many strategies have been explored to address this issue. Graphene, boron nitride and Al_2O_3 have been used to encapsulate phosphorene and prevent air contamination [44-46]. A study on fluorinated phosphorene has reported that the lifetime of phosphorene extends up to 7 days without an additional passivation layer [47]. Recently, Ag^+ modified BP was found to exhibit better stability and transistor performance [48]. However, it should be noted that the current phosphorene-based battery research relies on single-crystalline bulk phosphorus, which requires stringent synthesis conditions and is cost-prohibitive. Both degradation and high costs have hindered the industry-scale applications of phosphorene in batteries and other fields.

In this chapter, we present a cost-effective and easy-to-implement technique to exfoliate phosphorene with a pulsed laser using high energy mechanical milling (HEMM)-synthesized BP powder as the precursor. Surprisingly, the as-exfoliated phosphorene from the HEMM-synthesized BP powder was found to exhibit excellent ambient stability compared to that exfoliated from bulk BP crystals, as characterized by TEM and Raman spectroscopy.

3.2 Experimental

BP is not naturally available and must be transformed from red phosphorus or white phosphorus under high pressure and high temperature conditions. HEMM is a scalable method for creating the appropriate conditions for producing BP. Here, the synthesis procedure outlined in 2.2.1 is used as baseline. To obtain the raw BP powder, 6 g of red phosphorus (98.9%, Alfa Aesar) was mixed with stainless steel balls (12.7 mm ball: 10EA + 9.5 mm ball: 17EA) inside a stainless steel vessel with a capacity of 50 mL. The vessel was sealed in an argon-filled glovebox with the O_2 and H_2O levels maintained lower than 1 ppm. A shaker miller (8000M Mixer/Mill, SPEX) performed HEMM for 6 h. Red phosphorus was transformed to black phosphorus.

The as-synthesized BP powder was then added into N-methyl- 2-pyrrolidone (NMP, Alfa Aesar, 99.5%) in a vial. The sample solution was sealed with a cap attached with a sapphire window in a glovebox to prevent oxidation. An Nd–YAG pulsed laser with a wavelength of 1064 nm and a single pulse energy output of 100 mJ was used to scan the target through the window at a frequency of 1 Hz for 4 h. Each single pulse was less than 50 ms in duration. A magnetic stirrer was used for continuous mixing of the solution at 1000 rpm to ensure homogenous processing. After laser-induced exfoliation, the mixture was statically stored in the glovebox for 12 h. The upper 2/3 of the supernatant was then collected and centrifuged at 3000 rpm for 30 min to remove large unexfoliated BP particles. The collected supernatant was centrifuged again at 9000 rpm for 30 min. The final phosphorene deposit (denoted as HEMM phosphorene) was rinsed with ethanol several times to remove the NMP residue, and then dried on an SiO_2 (200 nm)/Si substrate in a vacuum for 12 h.

For comparison, a bulk BP crystal (99.998%, Sigma-Aldrich) was also used to exfoliate phosphorene (denoted as basic phosphorene) in NMP by pulsed laser using the same procedure.

The dried HEMM phosphorene and basic phosphorene were transferred onto a copper grid with a perforated carbon membrane for TEM analysis. Measurements were performed using a JEOL JEM-2010 TEM at a voltage of 200 keV. A WITec alpha300 RA confocal Raman system with a laser wavelength of 532 nm was used to analyze the samples. The power was adjusted to less than 0.5 mW with an accumulation time of 30 s to avoid laser-introduced damage during Raman characterization. We maintained a constant level of laser power across all characterization experiments. The magnification of the objective lens was 100 and zoomed to an area with a diameter of less than 1 mm. As mentioned earlier, the samples were stored in air at a temperature of 22 °C and humidity ranging from 25 to 30%.

3.3 Results and Discussions

3.3.1 Exfoliated Phosphorene Characterization

As shown in the XRD pattern in Figure 3.1 (a), the phosphorene maintains crystalline structure. From the TEM image with the selected area electron diffraction (SAED) pattern in Figure 3.1 (b), we can observe thick BP stacks with a polycrystalline structure. The puckered layered structure indicates the potential to be further exfoliated into single layer phosphorene.

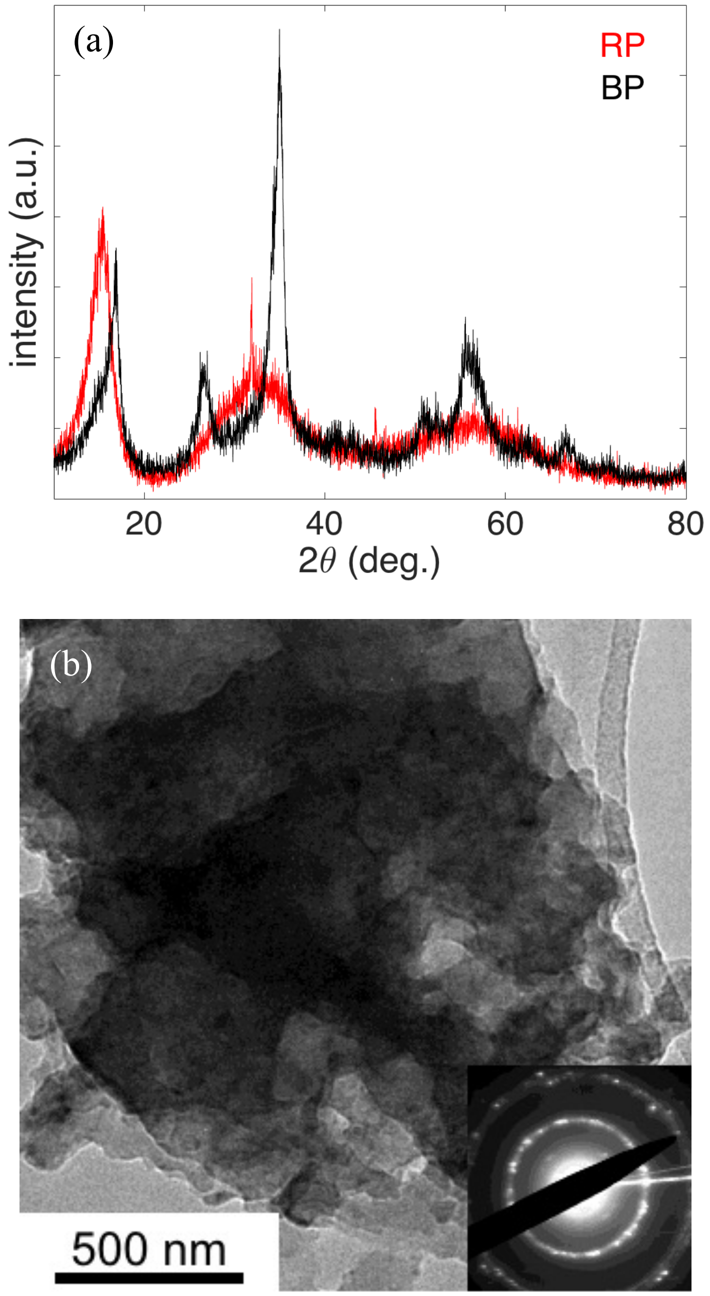

Figure 3.1 (a) X-ray diffraction patterns of black phosphorus (BP) and red phosphorus (RP); (b) TEM image of the HEMM-synthesized bulk BP with the corresponding SAED pattern.

In Figure 3.2 (a), the atomic force microscopy (AFM) image and the corresponding height profile shows an average size of about 1–2 mm and an average height of about 6 nm. We demonstrated for the first time that six-to-nine-layer phosphorene could be successfully exfoliated using HEMM-synthesized BP powder. Considering the simplicity of HEMM and the abundance of RP, the proposed method could be easily scaled up for industrial production of phosphorene. In addition, a pulsed laser is energy-efficient and tunable; the average power during the process was only 0.1 W. By optimizing the focal point of the laser beam and the power, phosphorenes with different sizes and thicknesses can be obtained.

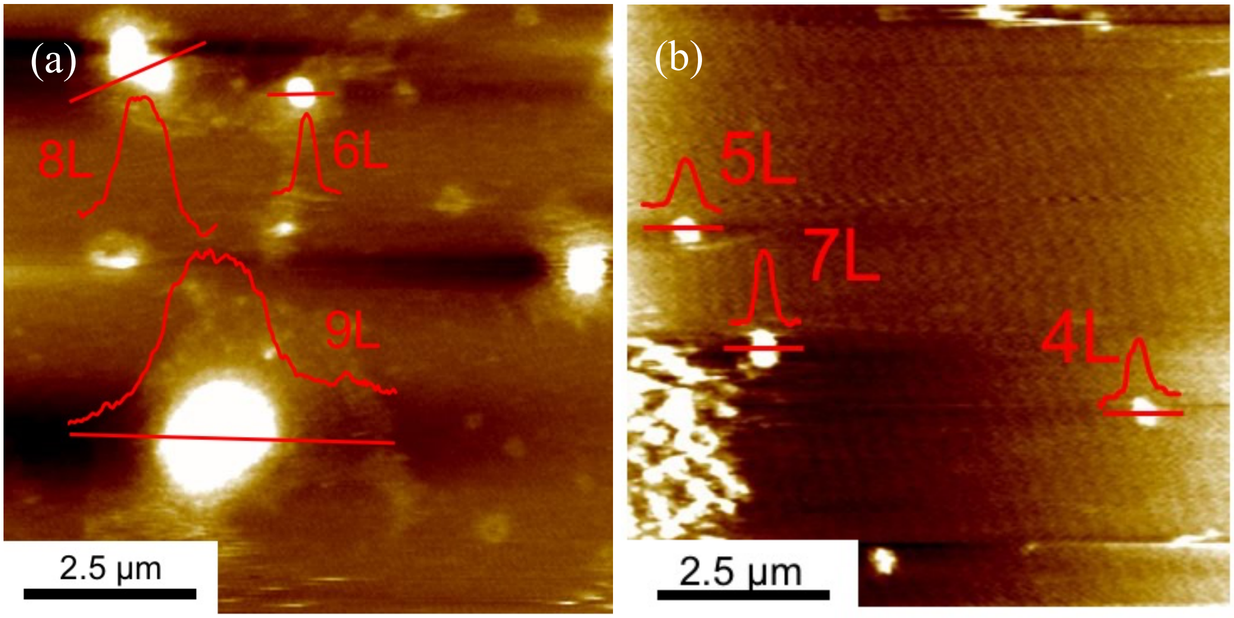

Figure 3.2 AFM topography of the (a) phosphorene laser-exfoliated from the HEMM-synthesized BP powder (HEMM phosphorene) and (b) phosphorene laser-exfoliated from a BP crystal (basic phosphorene).

The AFM image and the height profile of the basic phosphorene in Figure 3.2 (b) show fewer layers and smaller sizes compared to that of the HEMM phosphorene. The HEMM-synthesized powder may be composed of loosely connected phosphorene bundles, which makes it easier for large flakes to exfoliate. In contrast, it would be more difficult to peel off phosphorene from a BP crystal, leading to smaller phosphorene pieces. More importantly, TEM and Raman characterization experiments show that the HEMM phosphorene exhibit superior ambient stability compared with the basic phosphorene, which is discussed in further detail below.

3.3.2 Phosphorene Ambient Stability Comparison

As shown in Figure 3.3 (a)(c), the initial as-exfoliated phosphorene morphologies are quite different from one another. HEMM phosphorene presents a corrugated surface with more bends, overlaps and wrinkles, mainly because the HEMM process is stochastic in nature. As the high pressure and high temperature required for the transformation of red phosphorus to black phosphorus are obtained by random collision, the synthesized BP and the exfoliated HEMM phosphorene do not show a well-organized, single crystalline layered pattern, but instead show a polycrystalline structure. This structure is revealed by the diffraction rings in the SAED pattern in the inset of Figure 3.3 (a). Compared with the exfoliated HEMM phosphorene, the basic phosphorene maintained a flat surface and a single crystalline structure Figure 3.3 (c).

Phosphorene is known to suffer from rapid degradation when exposed to oxygen and moisture. Previous studies have suggested that complex P_xO_y and phosphoric acid are generated on the surface of phosphorene within a few hours [49], making phosphorene use in general ambient environments impractical. To date, no report on the stability of exfoliated HEMM phosphorene has been published. We exposed our grids with HEMM phosphorene and basic phosphorene to air for 24 h, during which the temperature was constant at 22 °C, and the humidity was between 25 and 30%.

TEM analysis revealed obvious morphological changes after this exposure Figure 3.3 (b)(d). Specifically, the surface of the HEMM phosphorene sample became slightly rougher without significant degradation. The SAED pattern also confirmed that the polycrystalline structure was maintained to a certain extent. In contrast, the smooth surface of the basic phosphorene became significantly degraded and contaminated. Such defects and fractures on the surface indicate significant oxidation and dampening, resulting from phosphorene's hygroscopic properties, and indeed, the SAED pattern revealed that the basic phosphorene completely lost its crystalline structure.

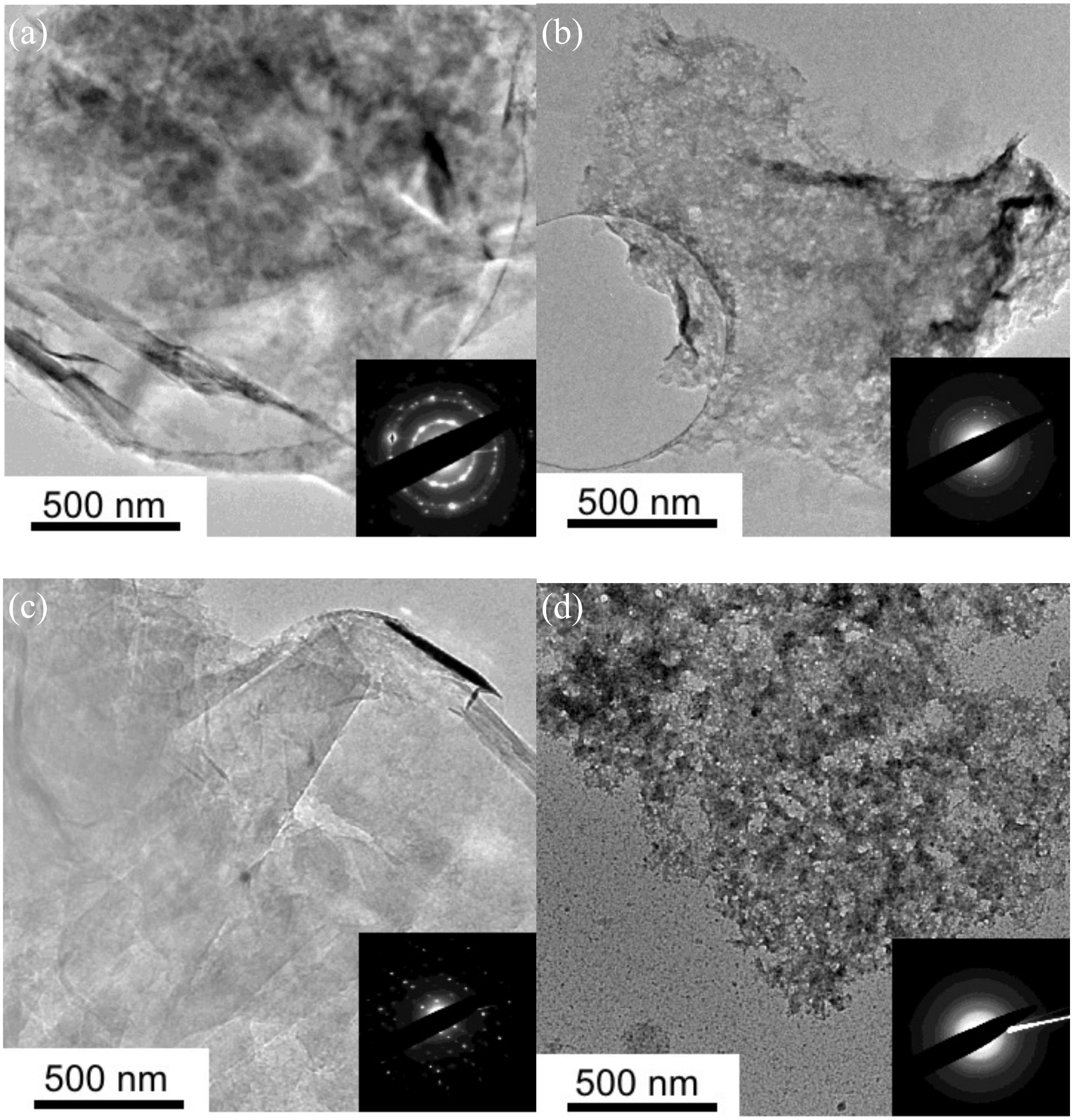

Figure 3.3 TEM images with the corresponding SAED patterns of the (a) as-exfoliated HEMM phosphorene, (b) HEMM phosphorene after 24 h air exposure, (c) as-exfoliated basic phosphorene, and (d) basic phosphorene after 24 h air exposure.

Figure 3.4 shows the Raman spectra of HEMM phosphorene and basic phosphorene on the SiO_2/Si substrate as a function of storage time. Compared with the bulk BP, all three-vibrational peaks show a slight shift to the right. Monolayer phosphorene is known to have the most significant shift; more layers correspond to a small shift [50]. The minor peak shifts of both the HEMM phosphorene and the basic phosphorene with respect to the bulk BP indicate that the pulsed laser exfoliation of BP produces few-layer phosphorene instead of a single layer one, which is consistent with the AFM and TEM results in Figure 3.1-3.3. Figure 3.4 (a) shows a minor decrease in the intensities of the three peaks of HEMM phosphorene during 6 hours of air exposure, as a result of the reaction with the oxygen and water in air. In contrast, the three peaks of the basic phosphorene almost completely disappear during 6 hours of air exposure, indicating significant structural degradation.

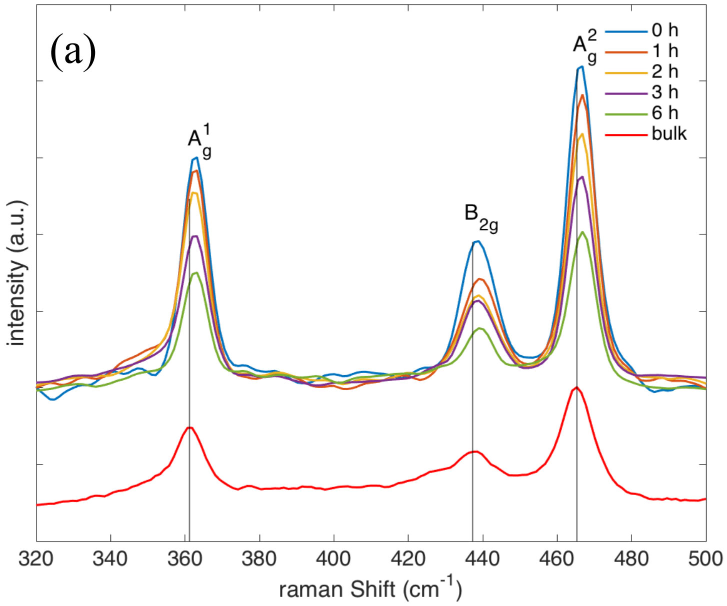

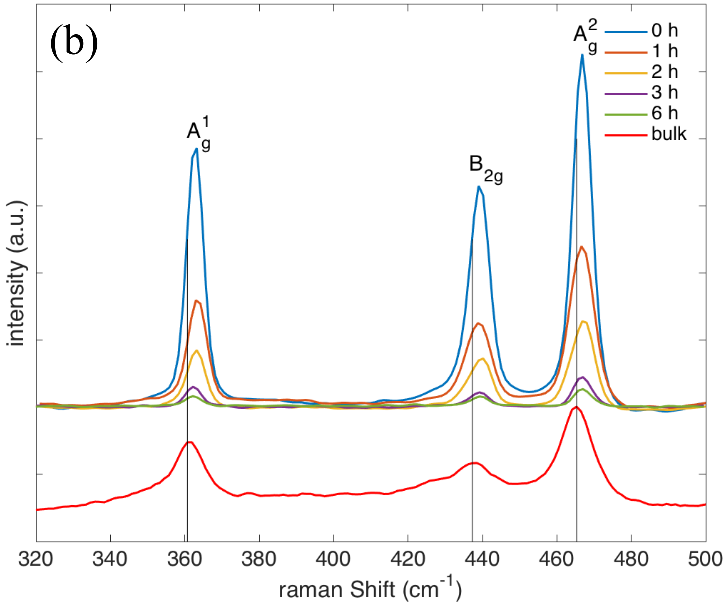

Figure 3.4 Raman spectra of (a) HEMM phosphorene and (b) basic phosphorene after exposure to air for 0h, 1h, 2h, 3h and 6h. The Raman spectrum of the HEMM-synthesized bulk BP is shown as a reference (red line).

Based on these observations, we propose that the following factors contribute to the superior stability of HEMM phosphorene.

First, the superior stability of HEMM phosphorene is attributed to its morphological and structural characteristics. The average size and thickness of HEMM phosphorene are larger than those of basic phosphorene, and HEMM phosphorene retains a polycrystalline structure rather than a single crystal structure. These characteristics are beneficial in preventing phosphorene degradation, which occurs in a layer-by-layer fashion. A recent study has demonstrated that a larger-sized phosphorene sample degrades more slowly than smaller-sized ones, and the degradation predominantly occurs on the edges rather than in the basal plane [45]. Thus, few-layer phosphorene with a perfect layer-by-layer stack and clear edge planes is more susceptible to degradation. We found that HEMM phosphorene has a pseudo-2D polycrystalline structure rather than being a perfect layer-by-layer stack connected by weak Van der Waals forces. The randomly distributed crystalized clusters strengthen the cross-layer connection, which may cause HEMM phosphorene to lack clear edges and boundaries for degradation initialization. Thus, HEMM phosphorene can better withstand damage caused by oxidation.

Second, HEMM phosphorene have a better NMP-based solvation shell to shield itself from reacting with oxygen. Phosphorene is known to be hydrophilic. Compared with the smooth surface of regular phosphorene, the rough surface of HEMM phosphorene allows it to be effectively covered with an NMP-based solvation shell during the process of liquid-based exfoliation. This shell could enable high oxidative stability. A previous study showed that various solvents are able to form tightly packed solvation shells adjacent to phosphorene surfaces, offering excellent protection from oxygen and water [51].

Finally, liquid phase pulsed laser exfoliation intrinsically ensures that the exfoliation occurs locally and quickly to avoid the oxidation conditions during the exfoliation process. In contrast, sonication, another liquid-based exfoliation method, causes both temperature increase and gas leakage as a result of the required long processing time. The uncontrolled temperature increase and vibration-induced gas leakage could accelerate phosphorene degradation. The pulsed laser-based method can prevent these issues.

3.4 Summary

In summary, we have demonstrated that liquid phase pulsed laser exfoliation combined with HEMM produced a pseudo-2D phosphorene structure that exhibited high stability under ambient conditions, as confirmed by TEM and Raman characterization experiments. To overcome the issues of phosphorene oxidation and instability, it is necessary to not only avoid oxidation-favorable conditions during exfoliation but also design a phosphorene structure and morphology that impede oxidation. We suggest that 3D-like or pseudo-2D phosphorene with fewer edge planes and a passivation layer is highly desirable for enhancing the long-term resistance to oxidation. The ease and low cost of processing and the high stability of the produced phosphorene are important for industrial applications, especially in the field of batteries.

Chapter 4

Scalable Ultrasonication-Assisted Exfoliation of Phosphorene with Superior Rate Performance in Lithium-Ion Battery

4.1 Introduction

The demand for rechargeable batteries with high energy density, high power density and long cycle life is growing rapidly with their wide applications in consumer electronics, electric vehicles as well as stationary energy storage systems [52].

Few-layer BP or 2D-phosphorene, which can be exfoliated by sonication, mechanical, and laser methods [53, 54], has recently attracted significant attention since it can provide more active reaction sites and shorter lithium diffusion pathways. These make them promising for high power density lithium and sodium-ion batteries [55-57]. However, there are still several obstacles hindering its practical use for battery application. First, previous phosphorene-based battery research utilized single BP crystals as a starting material, which is extremely expensive ($500/g), to produce phosphorene materials [57-60]. Without the development of a low-cost and scalable synthesis method, the use of phosphorene for battery application is not realistic. Second, similar to other high capacity anode materials (silicon, transition metal oxides/sulfides), phosphorene exhibits large volume change and insufficient electrical conductivity, thereby it needs to be bonded to a carbon backbone. Graphene and few-layer graphite are a suitable choice for carbon backbone since it exhibits similar layer structure to phosphorene and a few-layer phosphorene. Previous studies either simply relied on weak Van der Waals connection between phosphorene and graphene, or developed complex methods to strengthen connections from separated phosphorene and graphene (which we call as a bottom-up way) [55, 58, 61]. It is critical to develop a facile method which enables building strong chemical bonding between phosphorene and graphene [20, 62].

Finally, although previous studies claimed that the process of volume expansion/mechanical fracture/electronic contact loss is the major reason for fast capacity fade of phosphorene-graphene at high current densities, no clear evidence was provided to support their claims [61, 63, 64]. Moreover, it is still not clear why phosphorene or phosphorene-graphene can benefit against phosphorus-carbon composites.

To address the existing challenges, a facile synthetic route is proposed in this chapter. RP rather than single BP crystal was used as a starting material to produce BP by HEMM process and BP-graphite composite (BPG_BM) was synthesized by the subsequent HEMM process. Which is shown in Chapter 2. Then, the as-synthesized BPG_BM was subjected to ultrasonication directly exfoliate pre-bonded phosphorene-graphene (BPG_soni) nanosheets. While HEMM is an effective method to establish strong chemical bonding between phosphorus and graphite [20, 62], sonication is beneficial in exfoliating particles of layer structure like BP and graphite owing to its cavitation effect [53, 65]. During sonication process, the lateral size and thickness of few layer structure can be controlled by carefully adjusting the power and processing time.

This proposed method is inherently different from other studies, in which phosphorene and graphene were firstly exfoliated individually and then combined by Van der Waals interaction or special post-treatment [55-58, 60, 61]. In our method, the strong connection was already established before exfoliation and ultrasonication enabled to exfoliate the composite material without the loss of strong bonding. The exfoliated hybrid structure was directly applied to make anode without any additional processing. Thus, it is called as a top-down way. Far beyond convenience, the top-down exfoliation induces multiple unexpected but pleasant benefits at multiple scales, compared to conventional bottom-up methods. First, at atomic level, it is traditionally taken for granted that pristine phosphorene is good for battery performance. But recent computational study uncovered that defects-contained phosphorene enables higher binding energy of Li and P, and low diffusion energy barrier [66]. Both are very important for fast charge/discharge capability and cycling stability. Meanwhile, the bandgap and electron mobility of phosphorene are almost preserved [67]. Which means the HEMM-synthesized BP precursor with defects (vacancy, Stone-Wales, grain boundary) in our method is never inferior, but even superior than costly pristine bulk BP. As a result, the exfoliated phosphorene shows ultrafast and stable lithium ion storage. Second, at nanoscale, the stacking mode of phosphorene-graphene are different using top-down and bottom-up methods. For the bottom-up methods, large lateral sized (> 5 μm) phosphorene and graphene stack with each other layer by layer, in which only inter-plane lattice mismatch exists [55, 57, 64]. It is known that lithium ions react with phosphorene from edge to center, having anisotropic expansion rate in lateral plane [56]. The expansion in thickness direction is almost negligible given its thin film property. The interlayer space between graphene and phosphorene cannot accommodate inlayer volume change. The increased surface area is commonly thought to promote rate performance. But when considering phosphorene, this statement is flawed. The rate of 'edge to center' reaction mechanism depends little on surface area, but edge length or area. With large lateral size of phosphorene, the ratio of edge to surface (EtoS) is inevitably small, providing limited active reaction sites. Indeed, producing small lateral-sized phosphorene with high EtoS ratio is essential to rate performance of phosphorene. For our top-down method, the highly disordered phosphorus-graphite structure is constructed during ball milling process with strong chemical bonding. After exfoliation, not only inter-plane mismatch, in-plane co-existing of phosphorene-graphene leads to more layer distortions, larger inter-layer distance, more pores space and large number of exposed active reaction sites. The porous structure is effective to buffer isotropic volumetric change. Due to ultra-small lateral sized single crystal phosphorene (< 10 nm) buffered with graphene, the length of diffusion path is greatly reduced. Furthermore, the randomly organized crystal orientation of phosphorene make the diffusion path of Li ions in phosphorene is no longer restricted to zigzag direction, but more homogeneous in all directions. Therefore, anisotropic expansion effect is mitigated. These properties contribute to outstanding high rate cycling capability.

In this Chapter, the electrochemical performance of phosphorus-graphite (3D-heterostructure, BPG_BM) vs. phosphorene-graphene (2D-heterostructure, BPG_soni) was systematically investigated using a variety of electrochemical tests including electrochemical impedance spectra (EIS) and cyclic voltammetry (CV). Various characterization techniques were applied to understand the characteristics of the as-exfoliated nanosheets and their correlation with the electrochemical performance.

Our results showed the sonication-assisted modification achieved superior high rate performance. More than 70% of the initial capacities were retained after 100 high rate cycles. More important, close relationship between good cycling performance and internal structural evolution was established by post cycling analysis. The superiority can be attributed to nanoscale and homogenously distributed BPG_soni in the carbon buffer. For the first time, direct evidences were provided to show that the condense phosphorene-based BPG_soni electrode structure was maintained, free from electrode-level cracks and pulverization which were prevailing in BPG_BM. The same material of 2-D and 3-D structures behave fundamentally different in the similar electrochemical system. Both active kinetics and structural stability lead to the high initial capacity, retention ratio and coulombic efficiency of 2-D phosphorene-based LIB, demonstrating its suitability for power-type batteries.

4.2 Experimental Methods

4.2.1 Material Preparation

There are two major steps in BP-G composite preparation: ball milling and ultrasonication. Detailed ball milling procedure can be found in 2.2.1. Briefly, raw BP powder was transformed from RP (98.9% purity, Alfa Aesar) using shaking-mode HEMM device (8000D Mixer/Mill, SPEX Sample Prep.) with 6 hours of processing time. The ball to powder mass ratio was 17:1 and two different sized balls (12.7 mm (10 EA) + 6.35 mm (18 EA)) were used. To prevent oxygen contamination and self-ignition, BP synthesis was conducted in Ar-filled glove box (O_2 and H_2O level < 1 ppm). Then, raw BP particles and graphite particles were ball-milled separately by a planetary-mode milling machine (Across international PQ-N04) for another 12 hours at a relatively low speed of 600 rpm under Ar atmosphere. This step was to produce more nano-sized BP and graphite particles (BP/G mixture) by reducing the particle size further. The ball to powder mass ratio was 50:1, using three different sized balls: 10 mm (16 EA) + 6 mm (100 EA) + 3 mm (200 EA). The as-synthesized BP/G mixture with 50%:50% mass ratio was subjected to HEMM process for additional 24 hours, in order to make strong connection between BP and ball-milled graphite. The ball to composite powder mass ratio was 25:1, using two different sized balls: 12.7 mm (10 EA) + 6.35 mm (18 EA). The final product, BP-G composite, was used as active material to assemble coin cells (Li vs. BP-G half cells) as a benchmark sample, denoted as BPG_BM.

Probe ultrasonication (VCX 750, sonics) was employed to exfoliate the BPG_BM in Isopropyl alcohol (IPA, 99.9%). To minimize the side effects like oxidation, the processing power of 150 W was carried out for 10 hours in this study. Each single epoch had 45 s sonication and 15 s resting to reduce overheating. The as-processed liquid mixture was set statically for 6 hours to allow large particles to be deposited at the bottom. Finally, only thin layers suspending in the supernatant was filtered out by centrifuging at 9000 rpm for 30 min. The precipitate was dried and then directly used to make electrode. This sample is denoted as BPG_soni.

4.2.2 Material Characterization

Multiple material characterization techniques were used to understand the characteristics of the synthesized samples. AFM test was performed in non-contact mode by Veeco Dimension Icon Atomic Force Microscope. X-ray diffraction (XRD) analysis of raw RP, ball-miled BP (BP_BM), sonication-processed BP (BP_soni), BPG_BM, BPG_soni were taken from Rigaku SmartLab XRD with Cu Kα radiation source (λ=1.541 Å) and the scanning range was set between 10° to 80°, at a recoding rate of 0.02° per step. X-ray photoelectron spectroscopy (XPS) was done by Kratos Axis Ultra X-ray photoelectron spectrometer equipped with a monochromatic Al Kα excitation source (hν 1486.6 eV). Scanning electron microscope (SEM) images were taken from Phenom Pro at 10 kV. SEM with energy-dispersive X-ray spectroscopy (EDAX) analysis were conducted by JEOL IT500 at 8 kV. Transmission electron microscopy (TEM) was performed by JEOL 2010F at 200kV. Scanning transmission electron microscopy (STEM) analysis was performed using a JEOL 2100F Cs corrected STEM with a EDAX system at 200 kV. The particle size distribution was evaluated by Beckman Coulter LS 12 320 device in IPA-filled liquid module. The thermogravimetric analysis (TGA) test was recorded by TA Instruments TGA 550. X-ray microCT was performed on Zeiss Xradia Versa 520, with accelerating voltage of 60 kV and maximum power of 5 W. The sample was rotated through 180° to get 3201 projections. The 3-D reconstruction image was obtained from XMReconstructuor (Carl Zeiss Inc.) software. The mechanical indentation test was taken by Hysitron 950 Triboindenter.

4.2.3 Electrode Fabrication and Cell Assembly

To make electrode slurry, 0.4 g of either BPG_BM or BPG_soni as active material, 0.05 g of Super P as conductive additive, 0.05 g of Carboxymethyl cellulose (CMC) as binder were put together into deionized water. The slurry was homogenously mixed by SpeedMixer (FlackTek Inc.) at 3000 r/min for 30 mins using ten ZrO_2 balls (5 mm in diameter). The mixed slurry was cast onto a 12 μm thick copper foil current collector and then put into vacuum oven to evaporate water at 70 °C for 4 hours. The sample was further vacuum-dried overnight at room temperature. The total electrode material loading in electrode was controlled at about 1.4~1.6 mg/cm^2, which exhibited average thickness of about 30 to 40 μm. Typical CR2032 coin cells with lithium foil (0.75 mm thick, 99.9%, Alfa Aesar) as the counter and reference electrode were assembled. The electrolyte was 1.0 M lithium hexafluorophosphate ($LiPF_6$) dissolved in a 1:1 (by volume) mixture of ethylene carbonate (EC) and dimethyl carbonate (DMC) with 5 vol% fluoroethylene carbonate (FEC) and 2 vol% vinylene carbonate (VC) as solid electrolyte interphase (SEI) stabilizers. The separator (Celgard 2320) was pre-soaked in electrolyte for at least three days. All fabrication process was carried out in Ar-filled glovebox with moisture and oxygen level less than 0.1 ppm.

After cycling, the coin cells were disassembled for post-mortem analysis. The electrodes were washed by DMC three times to remove residual salts and SEI layer on electrodes and then dried in vacuum overnight.

4.2.4 Electrochemical Testing

The batteries were cycled using galvanostatic discharge (lithiation)-charge (delithiation) method between 0.01 and 2.0 V (vs. Li/Li^+) at different current densities using Maccor cycler. The EIS tests (BioLogic Science, VMP3) were carried out at different state of charge (SOC) after cycling test. The perturbation voltage amplitude was 10 mV and the frequency range was from 100 kHz to 10 mHz. CV tests (Princeton applied research, VersaSTAT 4) were conducted at a scanning rate of 0.1 mV/s between 0.01 and 2.0 V (vs. Li/Li$^+$). For electrochemical analysis, all calculations of capacity were based on the weight of BP only.

4.3 Results and Discussion

4.3.1 Materials Characterization

Based on previous research on BP or other high capacity anodes, the material properties, including average particles size, homogeneity and electronic conductivity, play an important role in the electrochemical performance [34]. Figure 4.1 (a) and (b) compares SEM surface images at the same macro scale (> 50 μm) of as-fabricated fresh BPG-BM and BPG_soni electrodes. While BPG-BM shows a wide range of particle size and presents many large agglomerated particles, BPG_soni exhibits nano-sized BPG flakes which are uniformly distributed in the carbon buffer matrix. No agglomerated particles are observed in the BPG_soni. This proves the effectiveness of sonication in dispersing agglomerated particles. The overall surface roughness of BPG-BM is significantly higher than that of BPG_soni.

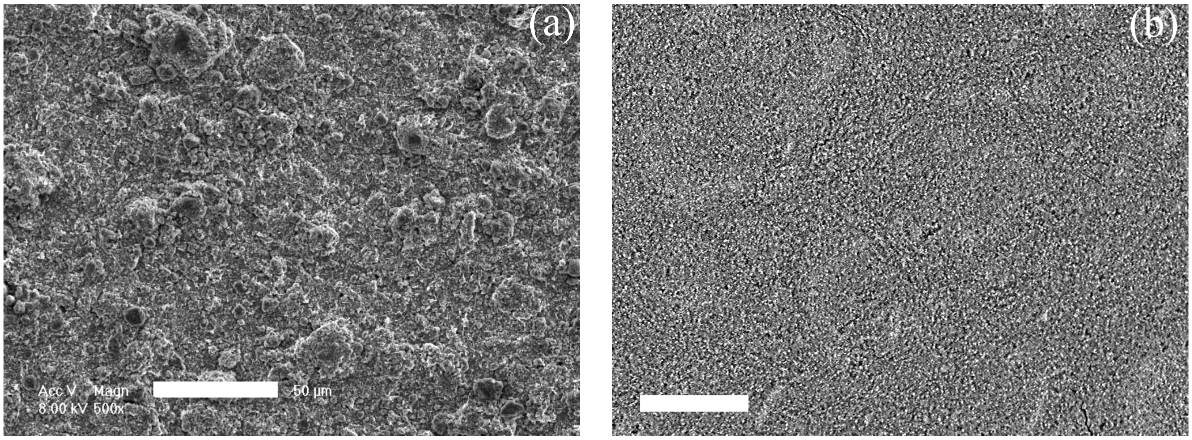

Figure 4.1 SEM images of electrode surface: (a) BPG_BM, scale bar = 50 μm, (b) BPG_soni, scale bar = 50 μm

As shown in Figure 4.2 (a) and (b), high magnification SEM images with corresponding EDS mapping provide another clear distinction between samples. For BPG_BM, some large BP particles (>5 μm) exist, which tend to have very weak connection to surrounding carbon (neither graphite, nor carbon black). Since particles larger than certain threshold are easily subjected to fracture upon cycling, the existence of large BP particles in BPG-BM is not beneficial in the electrochemical performance [35]. Particle fracture leads to not only consumption of Li-ions to form new SEI layer but also the loss of electrical contact with conductive carbon, reducing coulombic efficiency and reversible capacity. In contrast, BPG_soni has fewer large particles and phosphorene is homogeneously distributed inside the carbon network.

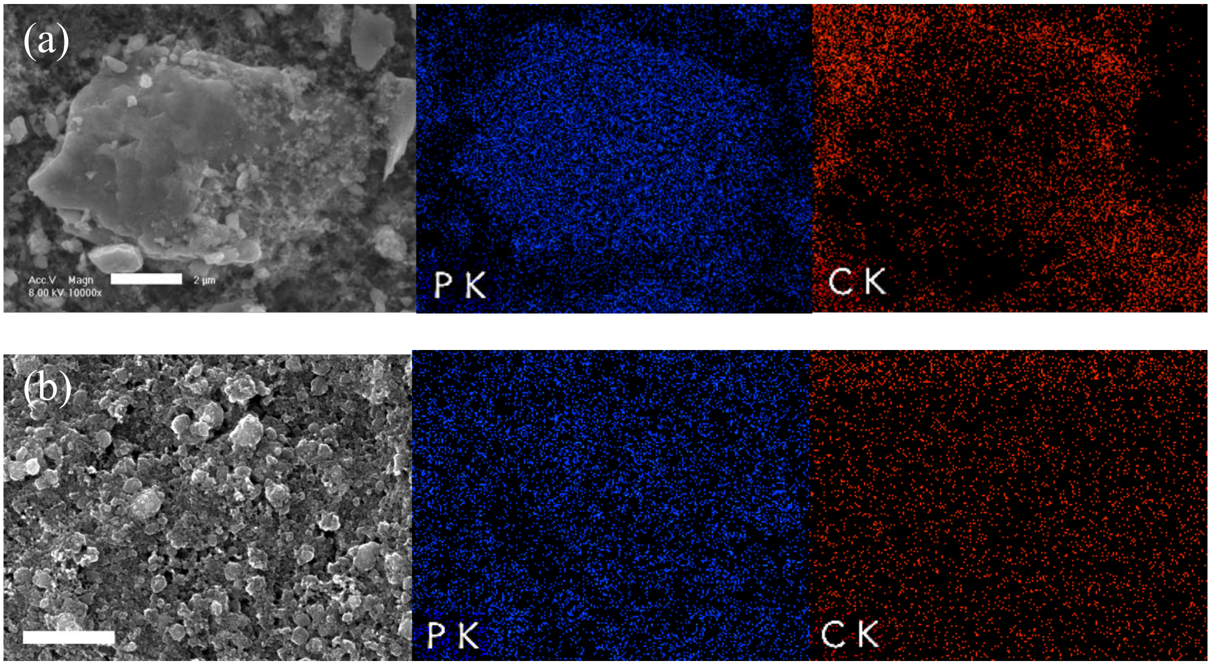

Figure 4.2 SEM images with the corresponding EDAX mapping: (a) BPG_BM electrode (scale bar = 2 µm) and (b) BPG_soni electrode (scale bar = 2 µm)

To compare particle size of two samples (BPG_BM vs. BPG_soni), the particle size distribution with corresponding statistics are provided in Figure 4.3 (e) and Table. 1. Overall, there are three distribution regions. (a) superfine nano-size region: 0.01 – 0.1 µm, (b) normal nano-size region: 0.1 – 0.8 µm, and (c) micron-size region: 1 – 5 µm. BPG_BM has more than 38 vol% of particles in region (c), while BPG_soni has only 13 vol% of micron-size particles. In region (b), BPG_soni has slightly higher volume ratio than BPG_BM. Note that particles in region (b) are very thin, as shown in the AFM result. More importantly, BPG_soni has a significant amount (33 vol%) of superfine nanosheets (< 0.1 μm). This can be directly ascribed to the exfoliation and dispersion effects induced by sonication. As demonstrated by AFM images in Figure 4.3 (b), very thin 2D structure is abundant in BPG_soni, proving production of phosphorene-graphene. The average thickness is about 10 nm. The average lateral size is between 0.5 μm to 1.0 μm, which is in good agreement with region (b) of BPG_soni in particle size analysis. These results demonstrate the synthetic route proposed in the present work successfully produce phosphorene-graphene nanosheets.

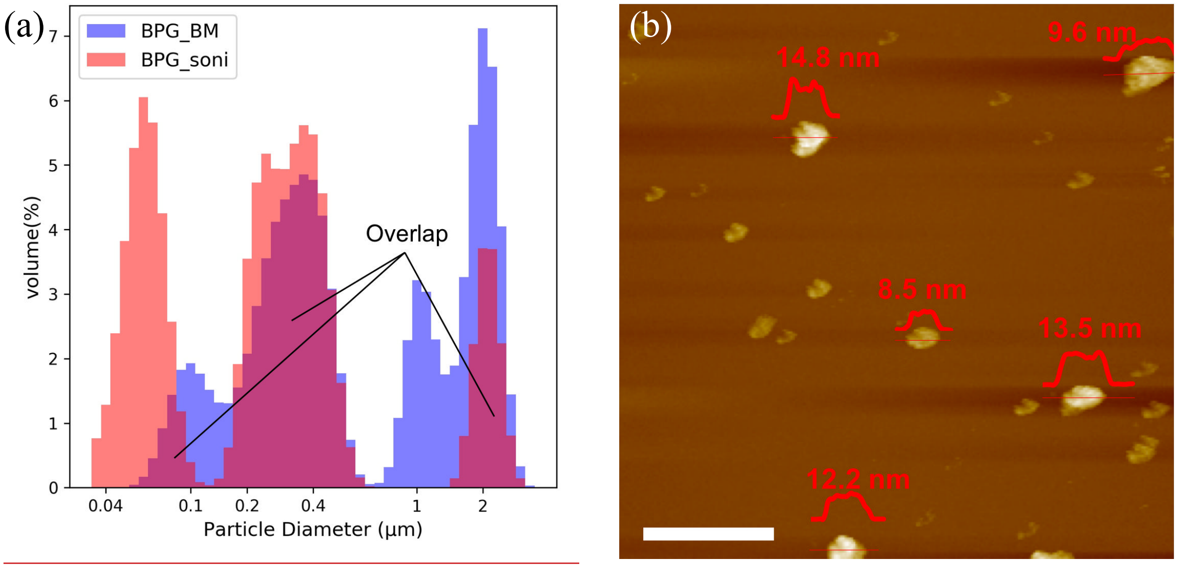

Figure 4.3 (a) particle size distribution of BPG_BM vs. BPG_soni; (b) AFM topography of BPG_soni (scale bar = 2 μm)

Table 4.1 Particle size distribution statistics

	Mean	Median	S.D.*	<10%	<25%	<50%	<75%	<90%
BPG_BM	0.888	0.414	0.776	0.134	0.248	0.414	1.672	2.082
BPG_soni	0.457	0.236	0.646	0.060	0.077	0.236	0.368	1.860

Unit: μm

*: standard deviation

The synthesized BPG_soni (i.e., phosphorene-graphene nanosheets) is not only small in size, but also maintains strong chemical bonds between phosphorene and graphene, as demonstrated by the following characterization results. It is commonly known that reduction in particle size is necessary to mitigate the mechanical degradation occurring in high capacity anode materials [36]. However, phosphorus-carbon materials also require robust chemical bonds of phosphorus and carbon, which is critical to improving the cycle performance. Thus, it is important to confirm whether BPG_soni materials produced by our approach can hold connections between phosphorene and graphene or not.

In Figure 4.4 (a) and Figure S 11, the STEM images of BPG_soni and BPG_BM with corresponding EDAX elemental mapping proves that the two samples are nanoscale mixture of phosphorus and carbon. The exfoliated phosphorene and graphene maintain coherent contact. In Figure 4.4 (b), the TEM image shows intimate contact of phosphorene and graphene with the corresponding lattice profiling. The outlined red regions show lattice spacing of 0.34 nm, matching the layer distance of graphene. The yellow regions show phosphorene lattice of different orientations. These results confirm that the exfoliated phosphorene and graphene don't exist separately, but well-connected with each other. The coexisting (020) and (014) planes of BP indicates the size of each single crystal in the structure is very small (~10 nm). Therefore, the entire region shows polycrystalline structure. The corresponding selected electron area diffraction (SEAD) pattern (inserted) shows concentric diffraction O-rings with random diffraction spots. The O-rings represent multilayer graphene. The random spots indicate the bonded orthorhombic BP [26].

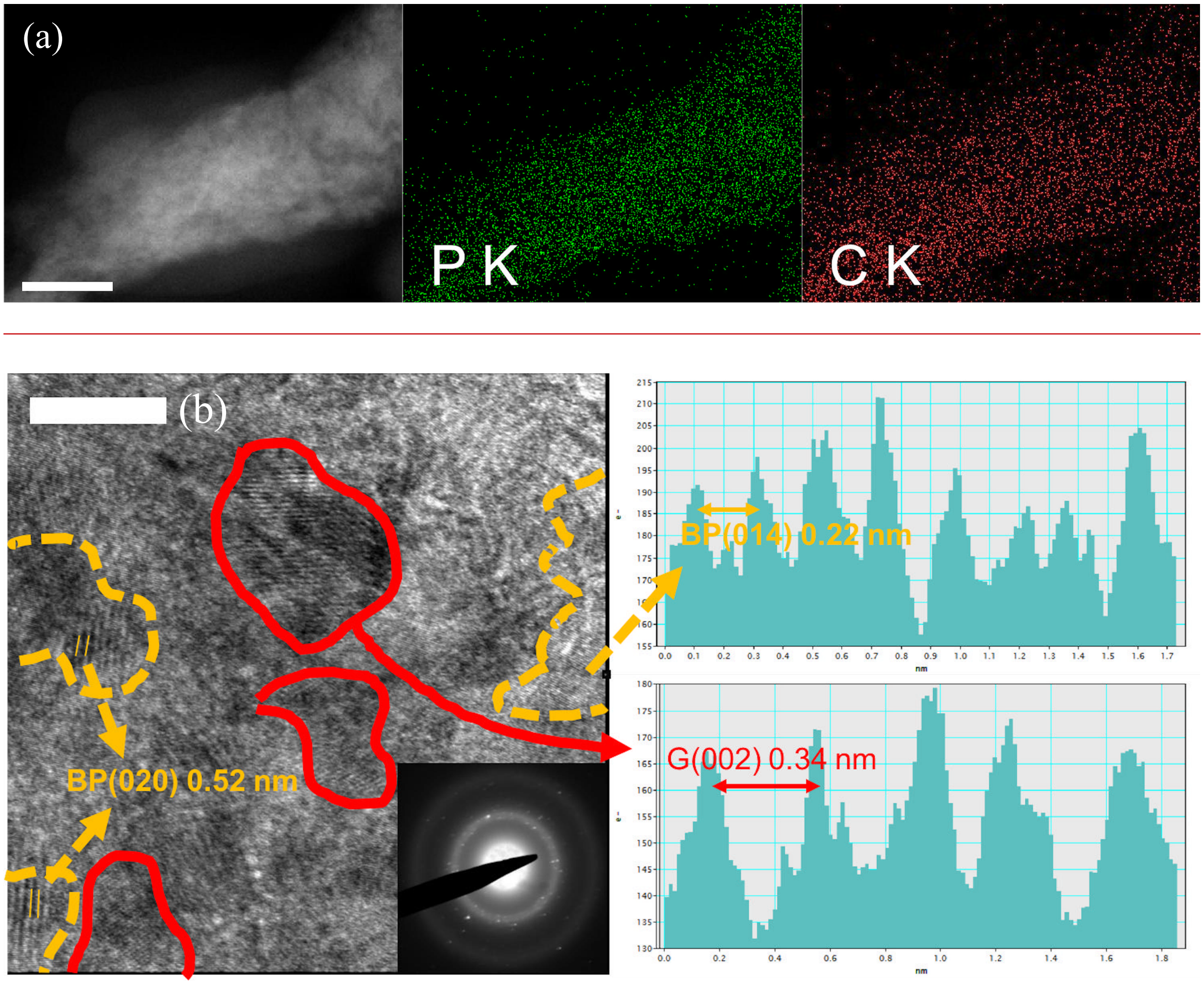

Figure 4.4 (a) Dark field STEM image of BPG_soni sample with the corresponding EDAX elemental mapping, scale bar = 20 nm; (b) high-magnification TEM image of BPG_soni with selected area Z-contrast profiles (The red-marked region shows graphene lattice structure. The yellow-marked region shows phosphorene lattice structure. scale bar = 10 nm)

High resolution XPS analysis is presented in Figure 4.5 (a)(b). In Figure 4.5 (c), the two major peaks located at 129.9 eV and 130.8 eV are assigned to P 2p3/2 and P 2p1/2. The ratio between them is close to theoretical stoichiometric value of 2:1, indicating the structure of phosphorene was maintained to most extent. The P-C bonds at 130.4 eV for 2p3/2 and 131.4 eV for 2p1/2 further quantify and confirm that they not only contact, but also chemically bonded. Same proportion of P-C bond was detected in C 1s XPS spectra at 283.5 eV in Figure 4.5 (d). The broad oxidized P (PO_x) and C=O/C-OH/C-O-C bonds suggest carbon and phosphorus were oxidized to some extent during HEMM and sonication processing.

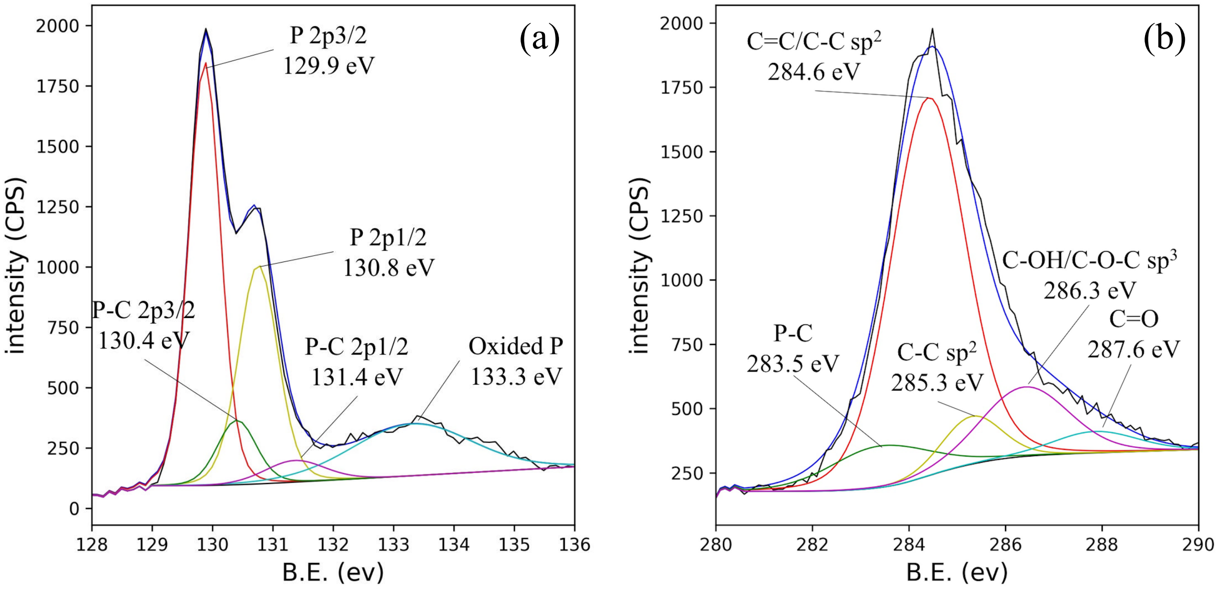

Figure 4.5 (a) P 2p and (b) C 1s XPS spectra of BPG_soni

A clear difference between BPG_soni and BPG_BM is observed from their XRD patterns in Figure 4.6. BPG_soni exhibits one broad peak near 23°, while BPG_BM one BP-related peak near 15° [020] and two peaks related to ball-milled graphite near 25° [002] and 45° [101] [37]. This result indicates that BPG_soni exhibits a different lattice structure with more amorphous regions compared with BPG_BM. Sonication process not only causes BPG exfoliation but also the change in BPG crystal structure. However, this is not the case for BP. The diffraction peaks of BP_soni are similar to BP_BM in terms of peak intensity and position, indicating the identical crystal structure for the two samples. In other words, BP lattice structure is not changed but its thickness is reduced to a few-layer phosphorene due to sonication effect. Thus, amorphization of BPG_soni is highly likely to be induced by interaction of phosphorene and graphene, not sonication itself. Formation of phosphorene-graphene heterostructure is the main reason for the lattice structural change.

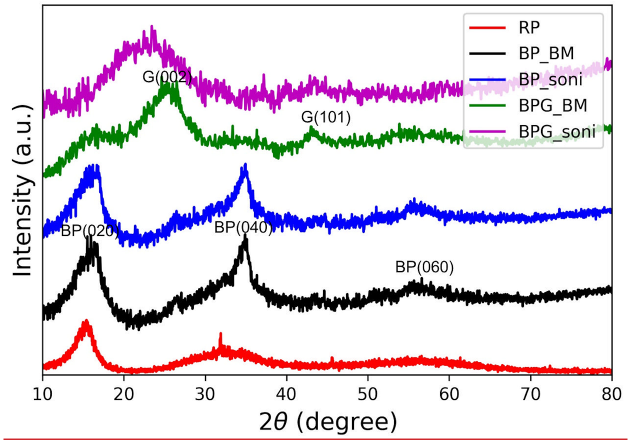

Figure 4.6 XRD patterns of red phosphorus (RP), ball milled BP (BP_BM), ball milled + sonication processed BP (BP_soni), BPG_BM, BPG_soni.

Although sonication induces phosphorene-graphene heterostructure but does not alter composition. Based on TGA result (Figure 4.7), BPG_soni has 47% weight ratio of phosphorus, which is very close to the initial of 50%. This indicates that phosphorus bonded to carbon homogeneously and coherently during HEMM process. And it remained after sonication process.

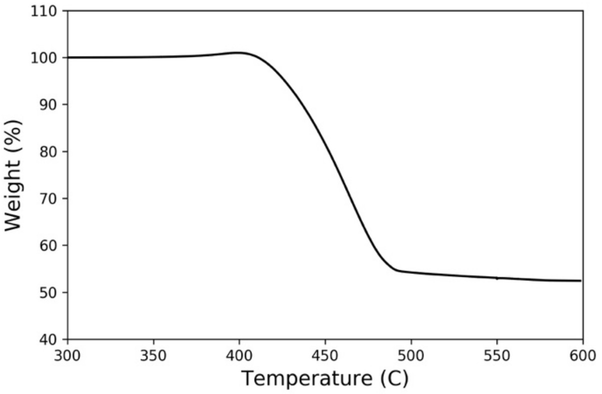

Figure 4.7 TGA test at 5° C/min for BPG_soni

In summary, sonication process contributes to dispersing agglomerate secondary particles while keeping a robust phosphorene-graphene heterostructure during exfoliation of bulk BPG_BM. Few-layer phosphorene nanosheets were encapsulated inside the carbon network, maintaining strong connection between phosphorene and graphene. Such an polycrystalline phosphorene-graphene heterostructure is expected to enhance the electronic conductivity and mitigate volume change-induced mechanical degradation during electrochemical reaction, which will be demonstrated in the following section.

To our best knowledge, this is the first time to apply a hybrid phosphorene-graphene directly exfoliated from ball-milled BPG composites to Li-ion battery application. This can be treated as a top-down method, distinguishing from traditional bottom-up methods in which phosphorene and graphene are separately obtained from bulk materials followed by combination of these materials in different ways. The methodology proposed here is highly scalable and cheap, without compromising the robust connection between phosphorene and graphene.

In the following section, the benefits of 2D phosphorene-graphene heterostructure (BPG_soni) in terms of electrochemical performance are discussed by comparing it with 3D BPG_BM.

4.3.2 Electrochemical Performance

Different types of BPC or BPG composites have been developed for LIBs in recent years. Representative capacity and cycling results are summarized, which can be found in a recent study [16]. Most of the previous studies used only low current densities to show the cyclability because their composites cannot avoid rapid capacity fade at high current densities.

In this section, high current densities (2 A/g for BPG_BM, 2, 4, 6 A/g for BPG_soni) are used for evaluation of BPG_soni to demonstrate its superiority as anode for high power LIBs. Figure 4.8 shows comparison of galvanostatic cycling tests and the corresponding coulombic efficiencies between BPG_BM and BPG_soni. For BPG_BM at 2 A/g, there is a huge capacity drop in the first 10 cycles. The initial reversible capacity is 1,980 mAh/g, which corresponds to 76.2% phosphorus utilization, and the coulombic efficiency is 81.1%. After only 10 cycles, the capacity of BPG_BM drops to 942 mAh/g and the coulombic efficiencies over 10 cycles is always smaller than 95%, indicating a large amount of irreversible capacity loss. After the first 10 cycles, the capacity continues declining to 271 mAh/g at the end of 100th cycle, but at a slower rate. The coulombic efficiencies are less than 98% until 100 cycles. In contrast, BPG_soni samples show outstanding electrochemical performance at high current rates, delivering better reversible capacity with stable cyclability. The initial reversible capacities at 2, 4, 6 A/g are 2,030, 2,003, and 1,597 mAh/g, while the initial coulombic efficiencies are 82.1%, 67.8%, and 63.3%, respectively. Note that BPG_soni has the 1st cycle coulombic efficiency (82.1%), which is close to that (81.1%) of BPG_BM at 2 A/g. This suggests that although BPG_soni has more fine particles than BPG_BM, it does not accelerate any side reactions including SEI formation initially.

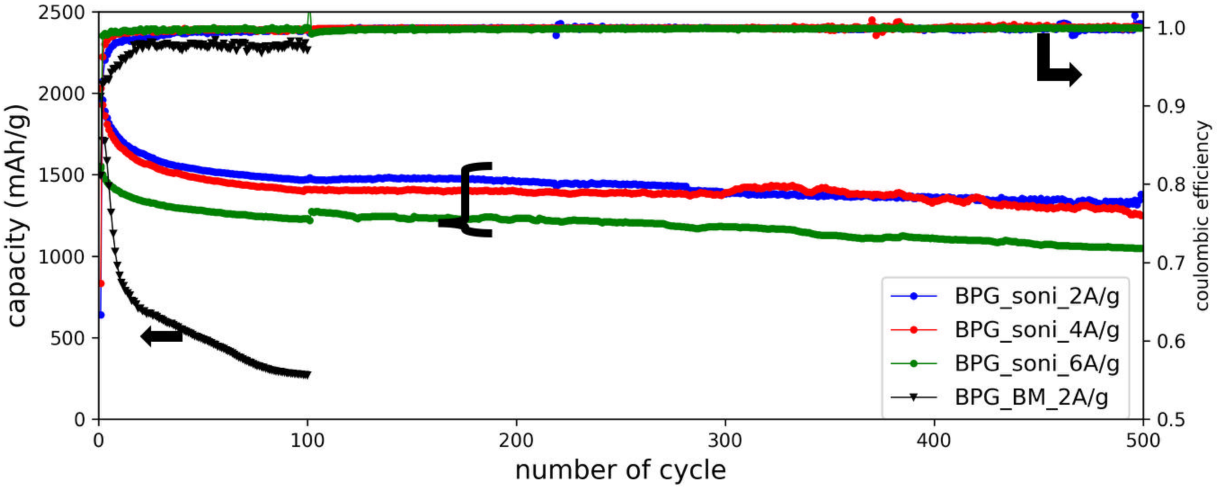

Figure 4.8 Discharge (delithiation) capacity and coulombic efficiency of BPG_BM and BPG_soni as a function of cycle number

More importantly, a clear distinction between BPG_soni and BPG_BM is found in their cycle performance and reversible capacity. BPG_soni did not suffer from rapid capacity fade, which observed in BPG_BM, at even higher current densities (4 A/g and 6 A/g). After initial several cycles, reversible capacity of BPG_soni becomes stable and the coulombic efficiency is always higher than 99.5%. The lithiation/delithiation process is highly reversible after stabilizing process (during initial cycles). This implies there is no dramatic structural degradation in BPG_soni and stable SEI layer does not deteriorate over cycles. This cycle stability could be correlated to the characteristics of phosphorene-graphene heterostructure. Phosphorene-graphene heterostructure is beneficial in withstanding large volume expansion/contraction, maintaining robust connection between phosphorene and graphene. As a result, BPG_soni retains more than 70% reversible capacity at the end of 500 cycles, even at high current densities.

To further explore reversible capacity at a different rate, stepwise cycling tests at various rates (0.2, 0.5, 1.0, 2.0, 5.0, 10.0 and 0.2 A/g) were carried out for BPG_soni and BPG_BM. The capacities and coulombic efficiencies are displayed in Figure 4.9. BPG_soni exhibited higher reversible capacities than BPG_BM at all current densities, delivering 2113, 1810, 1557 and 1222 mAh/g at elevated rates. Note that approximately 300 mAh/g is reduced as the current increases from 2.0 A/g to 5.0 A/g. In contrast, BPG_BM shows the capacity reduction of 1200 mAh/g at 5A/g and lower coulombic efficiency. This further demonstrates higher rate capability of BPG_soni than BPG_BM.

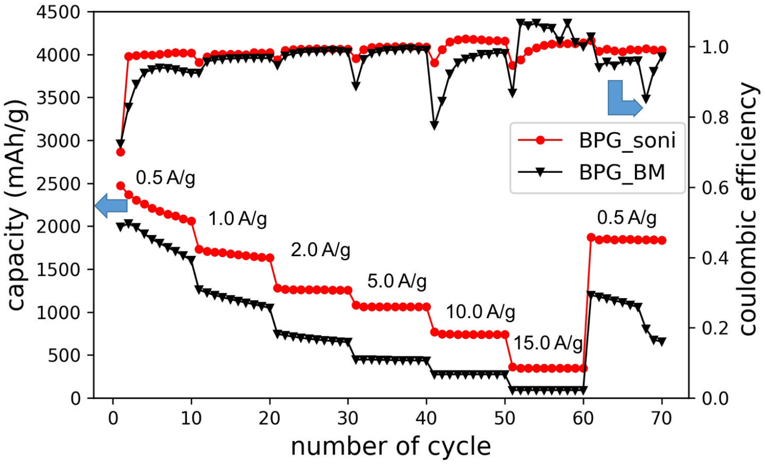

Figure 4.9 stepwise cycling tests for BPG_BM and BPG_soni at 0.2, 0.5, 1.0, 2.0, 5.0, 10.0 and 0.2 A/g

For BPG_BM sample, a relatively low rate (0.5 A/g) applied in initial cycles was helpful for stabilizing the cell, showing slower capacity drop compared with the case of a high rate (2 A/g in Figure 4.9). This also indicates BPG_BM has inferior rate performance than BPG_soni.

The galvanostatic CV (0.1 mV/s) and charge-discharge voltage (2 A/g) profiles of BPG_soni at different cycles are displayed in Figure 4.10 (a)(c), respectively. As shown in the CV profile, it is found that there is a broad cathodic peak at around 1.1 V at the 1st discharge cycle, which disappeared at subsequent cycles. This implies SEI formation process is mainly completed in the 1st cycle and no severe SEI growth or reformation is observed over subsequent cycles.[68] The lithiation process happens during 0.05-0.75 V (vs. Li/Li^+), while delithiation process occurs near a potential window of 1.0 – 1.5 V (vs. Li/Li^+). It is commonly known that BP is converted to LiP, Li_2P, Li_3P when the potential is lowered to 0.78 V, 0.63 V and 0 V [69]. The cathodic and anodic peaks in CV curve are broad. This is caused by the fact that ball milling synthesized BP doesn't have clear monocrystalline lattice structure. It's a mixture of polycrystalline and amorphous structure [54], also evidenced by XRD patterns in Figure 4.10 (c). After 20 cycles, the materials was completely activated and became stable. The main cathodic peak right shift from 0.6 V to 0.65 V. The main anodic peak left shift from 1.05 V to 1.0 V. The sharpening and shifting of peaks indicates rate enhancement in the kinetics reducing internal polarization [70]. The voltage hysteresis around 0.65 V (discharging) and 1.0 V (charging) of Figure 4.10 (c), matching well with CV peaks, is slightly higher than other publications [71], as much higher current density was used in our work, which results in larger polarization. After the initial stage, the cycling profile is very stable over cycles without severe polarization, indicating stability of the SEI layer.

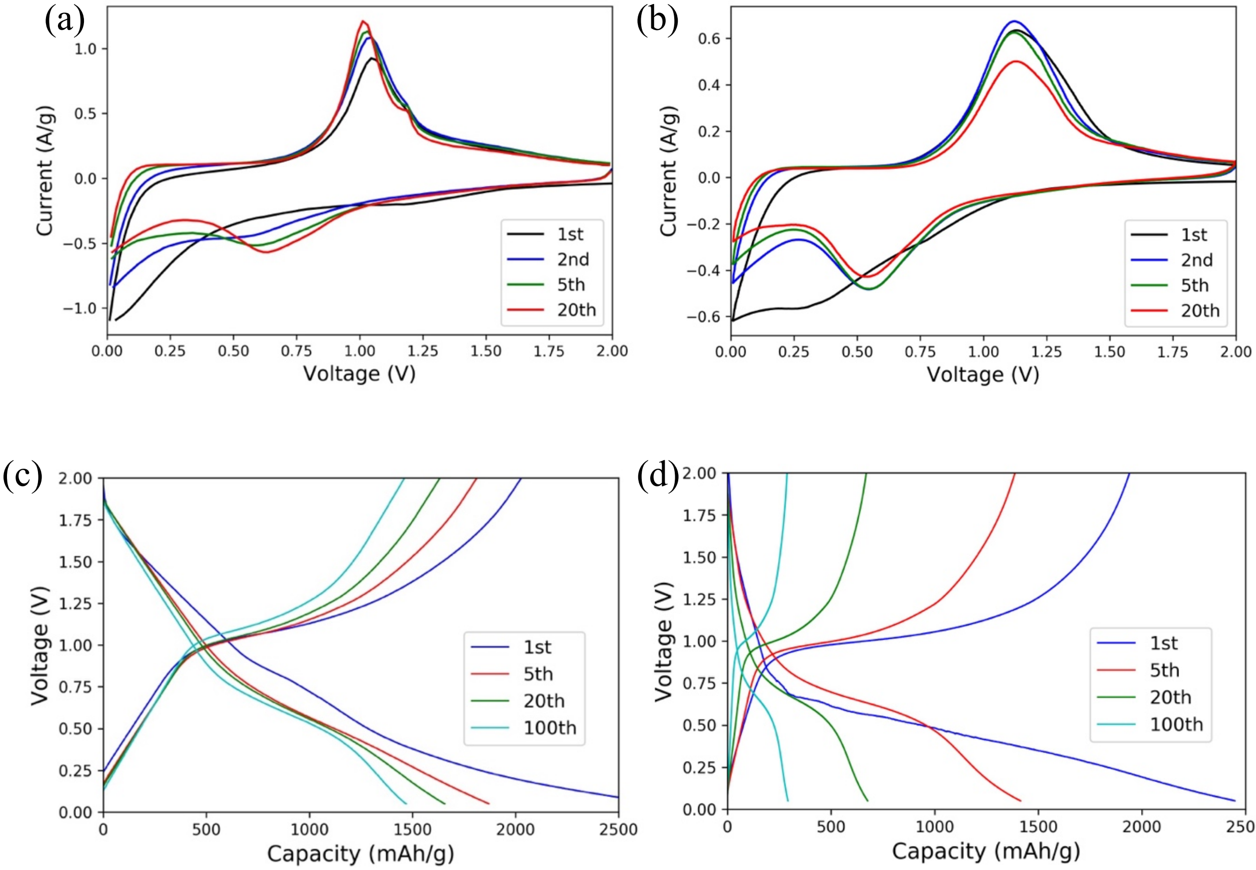

Figure 4.10 Cyclic voltammetry curves of (a) BPG_soni and (b) BPG_BM at 0.1 mV/s; Charge-discharge voltage curves of (c) BPG_soni at 2 A/g and (d) BPG_BM at 2 A/g.

For comparison, the CV and galvanostatic charge-discharge voltages profiles of BP_BM at 2 A/g are provided in Figure 4.10 (b)(d). The similar position of lithiation/delithiation CV peak imply the same electrochemical reaction mechanisms to BPG_soni. While its capacity dropped very quickly. And the flat and broad cathodic and anodic peaks in the CV curves implies electrochemical reaction happens inhomogeneously, mainly owing to BPG_BM has large composite particle size and uneven distribution.

It is important to point out BP_soni achieves stable cycle performance in despite of the increased overpotential induced by a higher current density (6 A/g). As shown in Figure S 12 (b), when the high current rate is used, a quick initial voltage drop and increase was clearly observed (voltage relaxation effect) before each charge and discharge process, respectively. This is attribute to the overpotential at the high current rate. This effect is more evident at the end of discharge than that of charge, which indicates that lithiation is slower than delithiation. The overpotential induced by a high current typically causes inhomogeneous electrochemical reaction and uneven material activation, lowering the reversible capacity. Nevertheless, BPG_soni shows stable cycle performance, maintaining moderate reversible capacity. This demonstrates fast relithation/delithiation process occurring BPG_soni and it survives such a harsh cycling condition without severe structural degradation. Due to shorter diffusion lengths of the heterostructured phosphorene-graphene nanosheets, BPG_soni is able to maintain cycle stability and structural stability at an extremely high current density.

To fully understand the difference between BPG_BM and BPG_soni, their electrochemical kinetics were systematically studied by EIS tests. In Figure 4.11, the EIS results of BPG_BM and BPG_soni after 1st cycle and 100th cycle are compared. These were cycled using 2 A/g and kept at 2.0 V (vs. Li/Li^+, fully charged status) before EIS testing. From high frequency (100 kHz) region to low frequency region (10 mHz), the Nyquist plot consisting of a depressed semicircle and an inclined line can be used to fit key components in the equivalent circuit in Figure 4.11 (b): the Ohmic resistance Re, the interfacial resistance (surface film coupled with charge transfer) at electrolyte and electrode interface Rct, the solid phase Warburg diffusion resistance Z_W, and the constant phase element CPE. The straight line of BPG_BM in low frequency region has a slope angle of 65° at the end of 1st cycle. After 100 cycles, there is no obvious change in the low-frequency straight line. BPG_soni sample has a slope of 75° initially and no change occurs after 100 cycles as well. This result indicates that ionic diffusion is not the primary contributor to capacity fade in both BPG_soni and BPG_BM. The low-frequency slopes of both samples deviate from the typical slope of 45° (semi-infinite diffusion), indicating finite-length Li-ion diffusion in nano-sized BPG particles. The larger low-frequency slope angle of BPG_soni demonstrated a shorter diffusion path than BPG_BM as well as the improved homogeneity of electrochemical reaction, which can promote faster Li^+ diffusion [72].

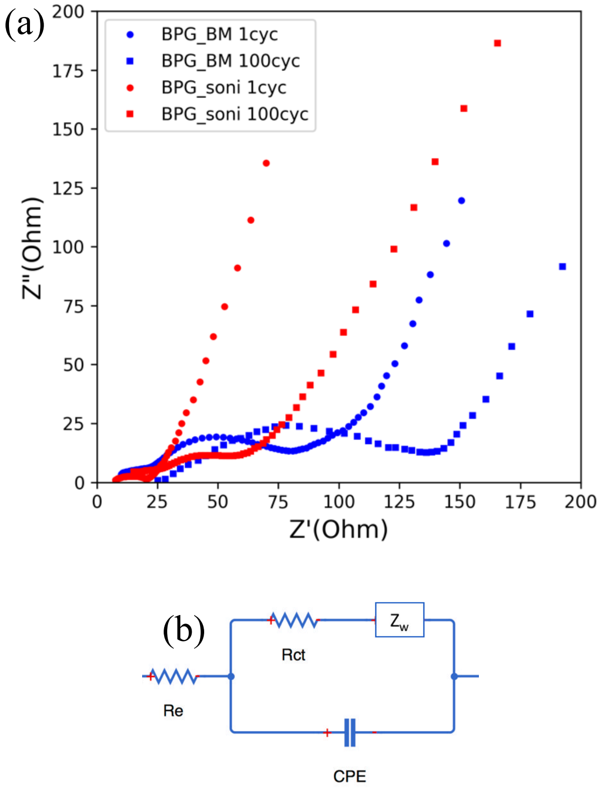

Figure 4.11 (a) Nyquist plots of (a) BPG_BM and BPG_soni after the 1st cycle and the 100th cycle; (b) Equivalent circuit model used to fit EIS data.

A clear distinction between two samples are observed in their charge transfer resistances, which can be approximated by the radius of semicircle in high-medium frequency region. The fitted *Rct* of BPG_BM increases from 38.34 Ω (after 1st cycle) to 72.27 Ω (after 100 cycles), while BPG_soni has a lower *Rct* of 15.45 Ω initially and the *Rct* increases to 49.28 Ω after 100 cycles. The smaller increase in interfacial resistance originates from the fact that no severe cracking or pulverization followed by SEI layer growth occurs at BPG_soni.

The superior cycle stability and rate performance of BPG_soni is attributed to the shorter diffusion length, homogenous electrochemical reaction, and no significant SEI growth.

To further understand the improved kinetics of BPG_soni, the resistance evolution of BPG_soni and BPG_BM was analyzed at different state of charge In Figure 4.12 (a)(b), the EIS of BPG_BM and BPG_soni were tested at 8 voltage stages: 1.5 V, 1.0 V, 0.5 V and 0.01 V in discharge (lithiation) process, and 0.5 V, 1.0 V 1.5 V and 2.0 V in charge (delithiation) process. To ensure stable and comparable electrochemical status, a low current rate of 0.2 A/g was used here. Generally speaking, most active materials can be activated during the 1st cycle formation process. In both samples, solid phase diffusion impedance, represented by the line slope at the low-frequency, gradually increases to the highest level when fully charged back. The final slope angle in BPG_soni is about 74°, which is larger than that of BPG_BM (63°). This is consistent with the above result (Figure 4.11(a)).

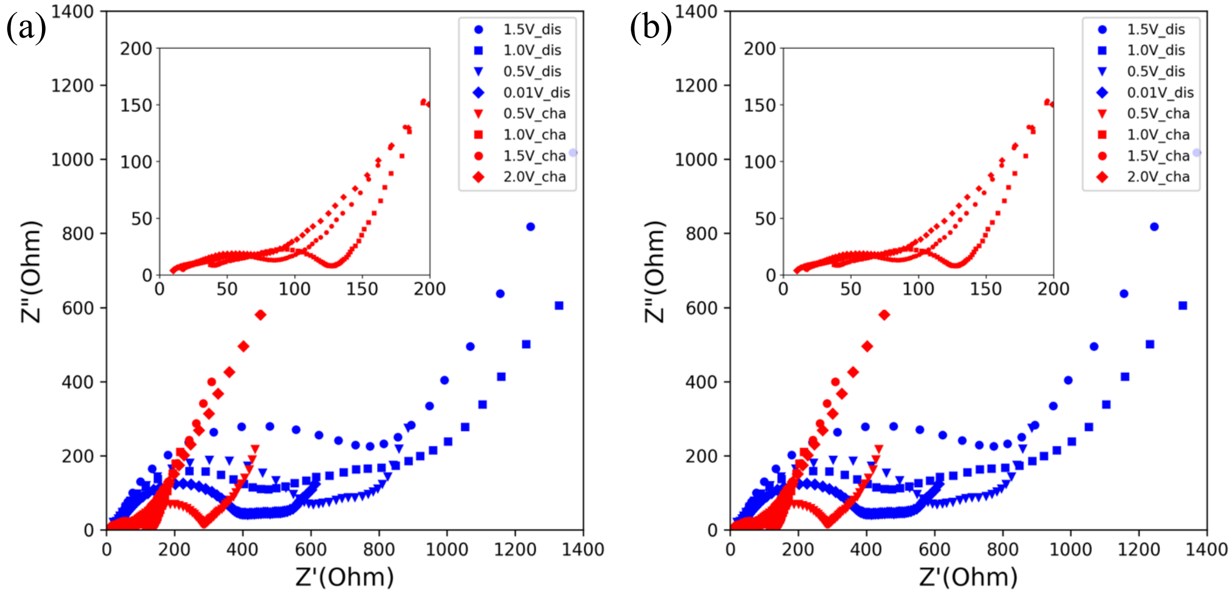

Figure 4.12 Nyquist plots of (a) BPG_BM during 1st cycle at different voltages, (b) BPG_soni during 1st cycle at different voltages.

Consistent with the above result, the difference between BPG_BM and BPG_soni mainly originates from interfacial resistance *Rct*. The *Rct* of uncycled two samples at open circuit voltage are close to each other. While during 1st discharge, the *Rct* of BPG_soni drops quickly to ~200 Ω at 0.01 V. The *Rct* of BPG_BM remains higher than 350 Ω. When fully charged back to 2.0 V, BPG_soni sample had a low *Rct* of 39 Ω, compared to BPG_BM of 86 Ω. More active reaction sites, short diffusion path, and good electronic connection of BPG_soni nanosheets are expected to facilitate fast kinetics and reduce electron/ion transfer/diffusion resistance.

Electrochemical reaction at relatively high rate is kinetically diffusion controlled. To better understand the origin of BPG_soni rate performance, a comparison study of diffusion coefficient is performed by GITT technology for the first discharge cycle. At the beginning of current pulse, a sudden drop of voltage come from Ohmic resistance IR. After establish stable concentration gradient, the voltage become stable and reach a semi-equilibrium stage. After removing current, the internal polarization relieves. Lithium ions diffuse uniformly within the active materials. This procedure is repeated until the battery reach full discharged stage.

The diffusion coefficient can be computed by:

$$D = \frac{4}{\pi\tau}\left(\frac{IV_m}{Z_A FS}\right)^2\left(\frac{\Delta E_s}{\Delta E_t}\right)^2, \left(\tau \ll \frac{L^2}{D}\right) \tag{4.1}$$

In which, D is the lithium ion diffusion coefficient in (cm^2s^{-1}). τ is pulse duration in (s). I is pulse current in (A). V_m is molar volume in (cm^3mol^{-1}). Z_A is charge number of lithium ion which is 1. F is Faraday constant. S is surface area of electrode in (cm^2). L is electrode thickness in (cm). ΔE_s is voltage gap between two current pulses. ΔE_t is voltage change excluding IR drop for each pulse.

The voltage profile and corresponding logarithm diffusion coefficient is plotted in Figure 4.13. Compared to BPG_BM sample, BPG_soni has faster ion diffusion at all discharge status. Higher surface area of BPG_soni provides more reaction sites at electrode and electrolyte interface, with short diffusion path in 2D structure. This directly evidences its superior rate capability.

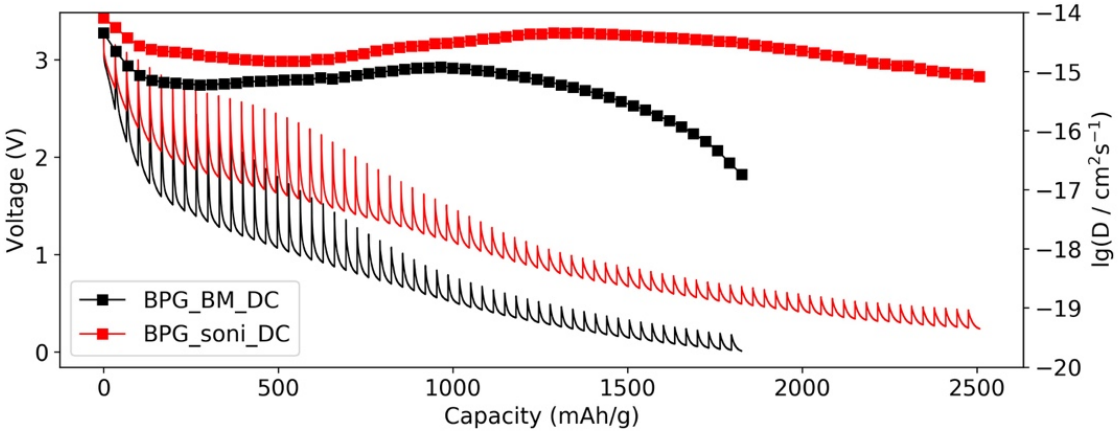

Figure 4.13 Voltage profiles using GITT cycling with logarithm diffusion coefficient in 1st discharge cycle

Thin film 2D materials is different from bulk material due to its surface pseudocapacitance property. Which is especially important for rate performance. Applying CV test with different scanning rates from 0.1 to 8.0 mV/s can quantify the proportion of capacitive contribution. The voltage profiles of BPG_soni and BPG_BM are shown in Figure S 13 (a)(b). i is the peak current for each voltage curve. v is scanning rate. Fitting coefficient a and b by taking log on both side, the b is a value between 0.5 and 1.0. The more b close to 1.0 is, the more surface controlled capacitive contribution. From Figure S 13(c)(d), BPG_soni has higher capacitive storage. Which agrees with the fact that BPG_soni has much higher surface area.

$$i = av^b \tag{4.2}$$

To further decompose the capacitor and diffusion-controlled storage modes, following formula is used.

$$i(V) = k_1 v + k_2 v^{1/2} \tag{4.3}$$

In which, $k_1 v$ represents capacitive contribution. $k_2 v^{1/2}$ is diffusion-controlled part. The two parameters k_1 and k_2 can be linearly fitted by each line in Figure S 14, respectively, and using the transformed formula:

$$i/v^{1/2} = k_1 v^{1/2} + k_2 \tag{4.4}$$

In Figure 4.14, enhanced capacitor effect is observed from BPG_soni, especially when scanning rate is high. Whereas traditional battery-type capacity dominates bulk BPG_BM. This difference highlights the superity of 2D materials' application in power type batteries. Surface redox reaction is also known for having less degradation and no volume change issue. For illustrative purpose, the detailed *I-V* curve is shown in Figure S 15 for both samples at scanning rate of 2.0 mV/s.

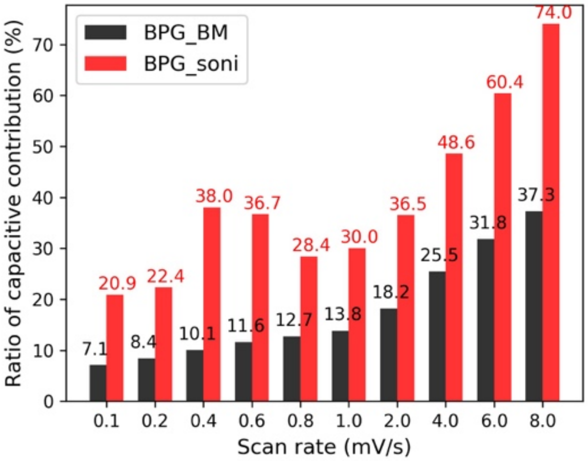

Figure 4.14 Proportion of capacitive contribution at different scanning rates

4.3.3 Cycled Cell Analysis

To unveil the underlying degradation mechanisms and the origin of different electrochemical performance of BPG_BM and BPG_soni, the cycled electrodes at 2 A/g were disassembled and analyzed systematically. In Figure 4.15 (a)(b), SEM images of the cycled electrode show their surfaces are significantly different to each other at the same magnitude. For BPG_BM sample, the original surface (in Figure 4.1(a)) becomes even more rough, with bubble-like pieces adhered to each other. Obvious cracks can be easily identified in BPG_BM. The higher resolution SEM image (Figure S 16 (a)) further proves that BPG_BM electrode suffers from serious pulverization during the volume change. There are numerous fine cracks inside the aggregated secondary particles. As shown in Figure S 16 (b)(c), the secondary particles experience not only electrode-level cracks but also particle-level cracks on the boundary connecting to surrounding region. According to the pattern, the particle-level crack is expected to form during the delithiation or electrode shrinkage process, which is a good agreement with a previous in-situ TEM study [34]. Since two types of cracking can cause electronic contact loss, structural instability at electrode level, inhomogeneous volume change rate, and more SEI accumulation, it is inevitable to avoid the fast capacity fade and impedance increase of BPG_BM. This indicates that ball milling process alone is not able to produce BPG exhibiting high rate performance.

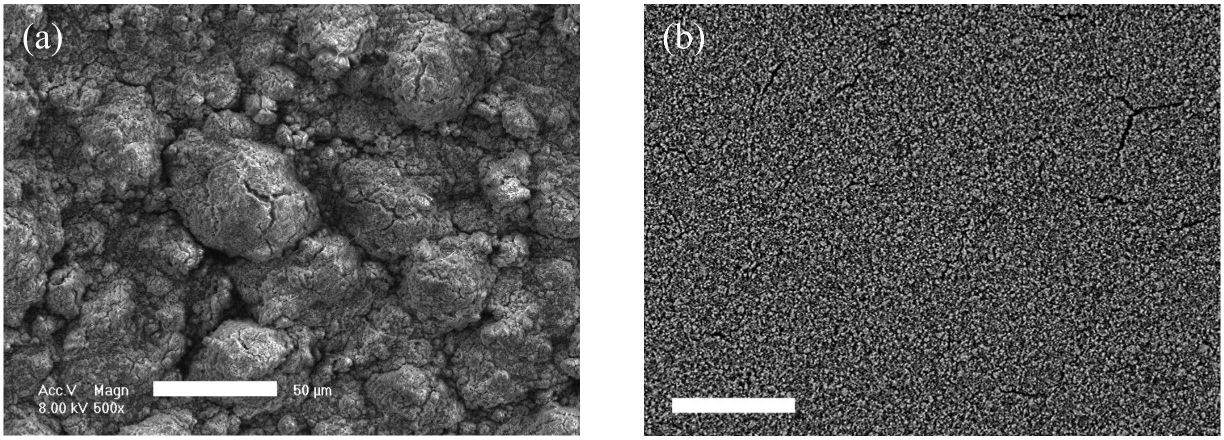

Figure 4.15 SEM surface image of (a) BPG_BM electrode after 100 cycles at 2A/g, (b) BPG_soni electrode after 100 cycles at 2A/g (scale bar = 50 µm)

In contrast, the cycled BPG_soni electrode still shows flat surface and coherent connection between phosphorene and graphene. There are minor line cracks at electrode level, as shown in Figure 4.15 (b). However, overall electrode keeps the original morphology and structure, demonstrating structural integrity of BPG_soni. In Figure S 17 (a)(b), the smooth surface and robust electrode structure maintains even at high current rates (4 A/g and 6 A/g), and a few more crack lines appear compared to Figure 4.15 (b). The crack lines highlighted by the 3D rendering image in Figure S 17 (c) are perpendicular to the surface and current collector. This means that they just separate the electrode as a “block by block” structure to accommodate volume change. Such pattern without obvious electronic contact loss would not affect the reversible capacity significantly. For high theoretical capacity anode materials, large volumetric change is inevitable during cycling. Generally, when a high current density is applied, inhomogeneous expansion and contraction will cause more serious structural damage [73]. Surprisingly, this issue is significantly mitigated by exfoliating 3-D bulk BPG_BM to 2-D nanosheet BPG_soni.

More insights can be extracted from the 3-D micro-CT results in Figure 4.16 (a)(b). The pulverized surface of BPG_BM is further confirmed from the reconstructed 3-D rendering image in Figure 4.16 (a). More importantly, the pulverization penetrates into the electrode and cause severe layer delamination, as shown in the grayscale segmentation image. Such a dramatic change does not occur at BPG_soni sample (Figure 4.16 (b)). In general, electronic contact loss caused by volume change is considered as a major reason for severe capacity loss for high capacity anodes, from the mechanical point of view [74]. However, this should be analyzed through multiscale levels, considering chemical bond breaking (nanoscale), isolation of active particles and conductive matrix (particle-scale), and electrode delamination (electrode-scale). Herein, we prove that the sonication-induced exfoliation not only addresses the robustness of BPG_soni at nanoscale, but also has a significant latent influence on the coherency of entire electrode. It is known that 3-D bulk BP particles have anisotropic volume expansion rates [75]. However, the expansion of phosphorene is confined to 2-D lateral directions only. With a constrain enforced by tightly bonded graphene, such an expansion can be further restricted. As a result, there is no inhomogeneity and local stress concentration in the electrode upon cycling. This is the reason for structural integrity of BPG_soni upon cycling at even high current rates.

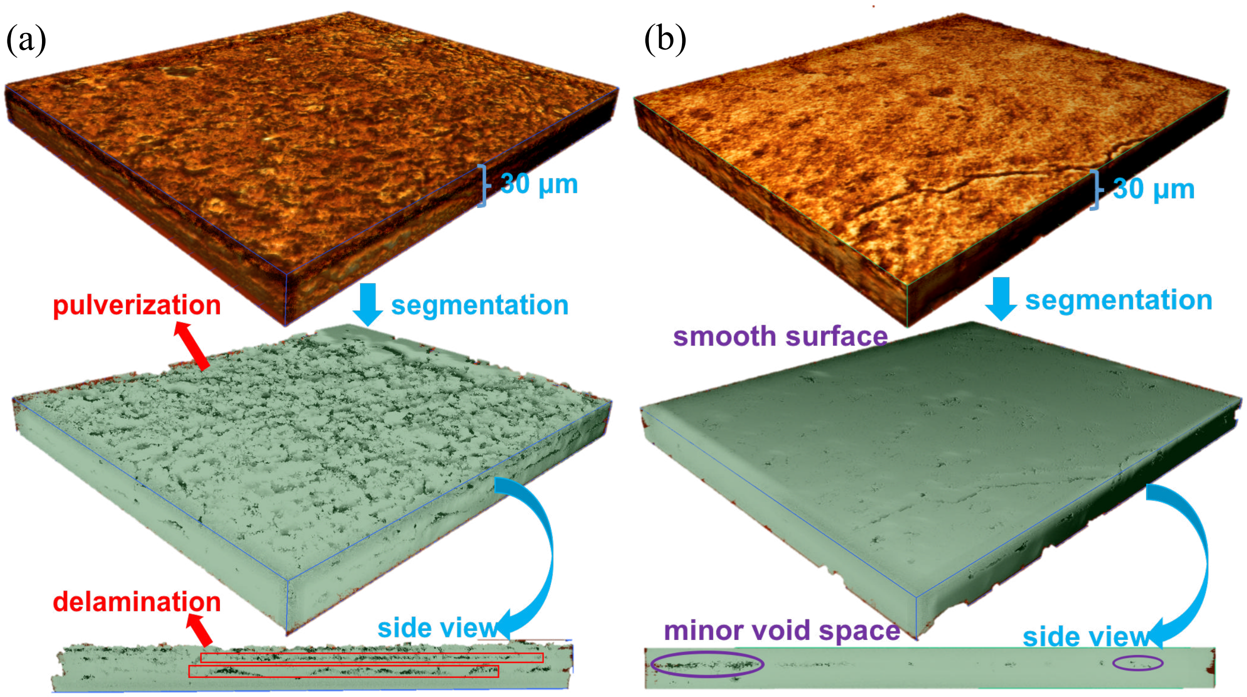

Figure 4.16 3D representation, threshold segmentation, and zoom-in side view of (a) BPG_BM electrode after 100 cycles at 2A/g, (b) BPG_soni electrode after 100 cycles at 2A/g

Based on the grayscale segmentation images, the quantitative analysis on the pore volume percentage versus the normalized thickness direction is provided in Figure 4.17, the visualized pore regions are shown in Figure S 18. Due to the intrinsic error in the electrode thickness measurement, the normalized thickness of 30 layers (0: surface to separator, 100%: interface to current collector) for two samples are used here. BPG_BM has average pore volume of 21.8%, while BPG_soni has the average of 10.2%. More importantly, the pores of BPG_BM distribute unevenly, concentrating near the top surface (due to pulverization and inhomogeneous expansion) and the electrode/current collector interface (due to delamination from different volume expansion rates). This uneven distribution of fractures severely occurs at a high current density cycling [76]. The electrode-scale electronic contact loss is expected to be the most deteriorative, making most capacity irreversible.

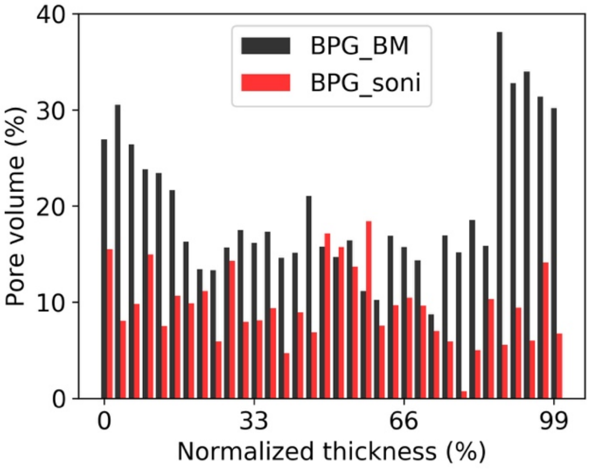

Figure 4.17 The percentage distribution of pore volume along normalized thickness for two cycled electrodes

Multiple mechanical degradations inside the electrode at different scales described above highly relate to the electrode mechanical strength. The two cycled samples were further characterized by micro-indentation tests with the maximum loading of 1000 μN. The representative force-displacement curves with setting parameters can be found in Figure S 19 and the results are summarized in Figure 4.18. Ten surface points were randomly selected to measure the elastic modulus and hardness of cycled BPG_soni and BPG_BM. The detailed analysis methods can be found in the previous studies [77, 78].

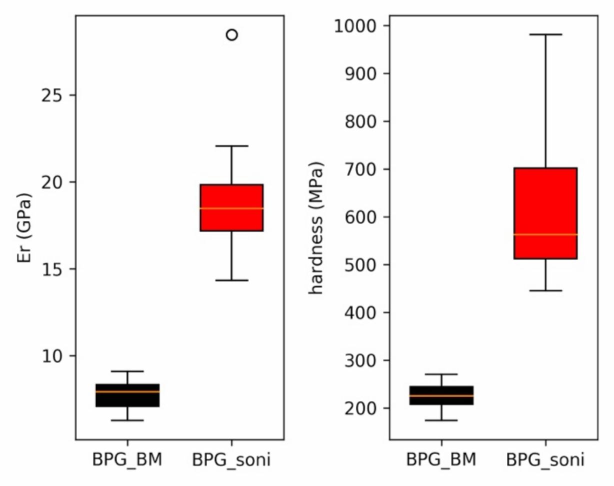

Figure 4.18 Elastic modulus and hardness comparisons for two cycled electrodes.

This mechanical strength results further prove the superior structural stability of BPG_soni. While BPG_BM is very weak and fragile after cycling due to surface pulverization, BPG_soni maintains a robust mechanical strength. This is attributed to significant differences in morphological and tomographic properties of cycled BPG_soni and BPG_BM electrodes.

In summary, the improved kinetics of BPG_soni have unveiled by comparing the counterpart BPG_BM and the relevant cracking and pulverization mechanisms are described in schematic diagram in Figure 4.19. BPG_soni enables fast Li-ion diffusion, homogeneous electrochemical reaction, and structural stability due to the characteristics of 2D nanosheets, thereby successfully improving electrochemical performance at even high current rates. Sonication process allows the agglomerated secondary particles formed during ball milling to disperse into fine primary particles while exfoliating to 2D nanosheets. As a result, BPG_soni is uniformly encapsulated inside carbon black network. During even high-rate cycling, the volume expansion/contraction of BPG_soni occurs homogeneously. There is no significant stress concentration at the electrode, thereby causing no crack/pulverization growth.

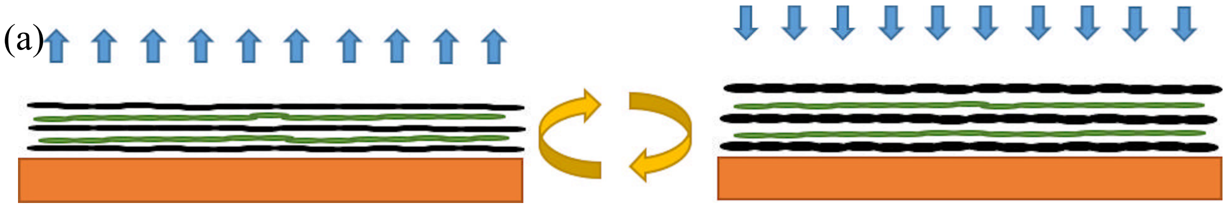

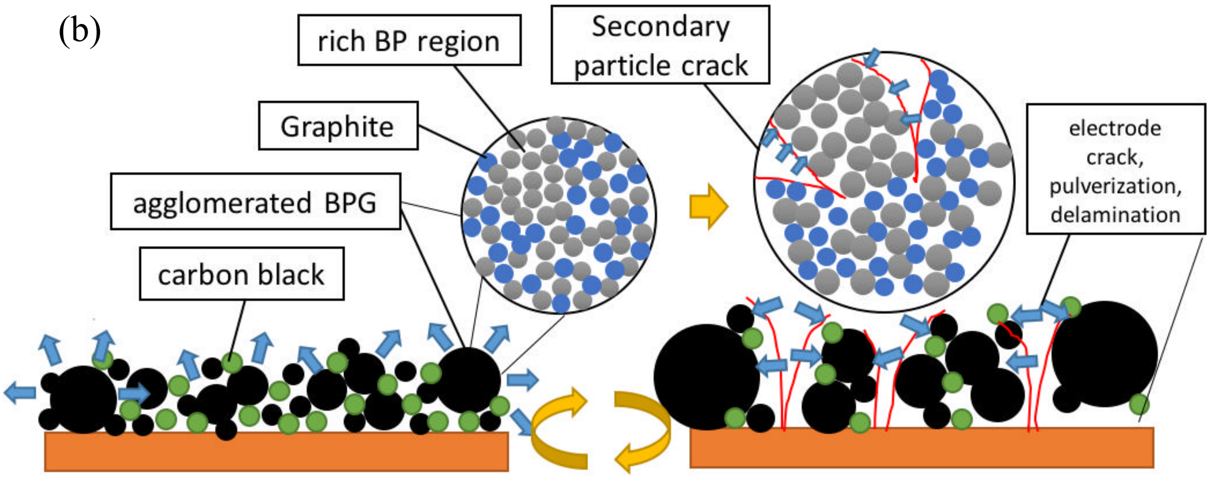

Figure 4.19 Schematic diagram of (a) volumetric change pattern for BPG_soni, and (b) volumetric change pattern and the associated degradation mechanisms for BPG_BM.

On the other hand, the entire electrode of BPG_BM (Figure 4.19(b)) is not homogenous, causing volume change to occur anisotropically in local regions. The cracks continue growing at multiple scales. Serious electrode-level powder pulverization and delamination, especially near the top surface and electrode/current collector interface, reducing the capacity significantly within a few cycles. For this reason, the electrode become vulnerable to any external forces. BPG_BM also has particle-level cracks. This is because some secondary particles which exceeds certain threshold size cannot sustain contractive force during delithiation [79]. Due to strong agglomeration behavior of particles during ball-milling process and its stochastic nature, the ball milling itself is difficult to control the particle size and produce homogenous composite particles. Particle-level cracking of BPG_BM could be due to inhomogeneous distribution BP and graphite in the composite form.

4.4 Summary

A novel top-down synthesis procedure, HEMM followed by probe ultrasonication, is proposed to produce 2D nanosheet phosphorene-graphene heterostructure for LIB anodes. The facile and cost-efficient synthesis method combines the advantage of two scalable methods using cheap RP as a precursor directly, not a bulk BP crystal. Compared to a ball milling-processed sample (BPG_BM), the additional sonication process achieves high homogeneity and nanoscale of 2-D BPG heterostructure without compromising the established chemical bonding, resulting in coherent electrode structure. The electrochemical cycling tests reveal that such an optimal structure indeed enhances the electrochemical kinetics, showing superior rate performance and cycle stability with high reversible capacities even at high current rates. The correlation between 2-D nanosheet BPG heterostructure stability and improved electrochemical performance is established, both qualitatively and quantitatively. The optimal composite morphology and thin film structure of BPG_soni are found to be mechanically robust in terms of electrode-level and secondary particle-level cracks and delamination. As a result, they experience slower capacity loss, less electronic contact loss and few SEI accumulation, even at elevated current densities. The long cycle life and high power density of sonication-modified BPG paves a practical way to realize phosphorene-based materials in battery industry.

Chapter 5

Incorporating Key Material Properties into Machine Learning Based Failure Prediction for The BP-based LIB

5.1 Introduction

Lithium-ion batteries (LIB) have been widely deployed as energy storage system, especially with prosperity of electric vehicles. Its low cost and high energy density are sharpening the energy industry [80]. However, the fast deterioration of battery has still been a major challenge so far. Coupled mechanical, chemical and electrochemical stresses get involved in the nonlinear degradation process [81]. In real production and commercial usage, accurate diagnosis of the state of health (SOH) is crucial [82]. SOH is defined as the ratio of remaining capacity to initial fresh capacity. The battery is usually thought to be dead when SOH < 75%. Under normal cycling condition, this failure will happen after long time operation. Modeling of lifetime is a long-standing topic in battery research community [83].

Many previous studies focus on SOH estimation through different strategies [84]. In which, model-based methods use electrical components to simulate the battery system, and then perform experiments to do parameterization. Remmlinger et al. [85] proposed an on-board model-based monitoring approach of SOH estimation. Li et al. [86] compared three filter-based methods with respect to computational efforts, robustness and long term performance. Chen et al. [87] used an empirical model calibrated by real-time measurement for prognostics. Physical or empirical models provide fundamental mechanistic understanding of degradation. However, diverse failure modes, complex working conditions and cell variability make it is hard to fully explore all working scenarios. Recently, data-driven methods based on machine learning algorithms become popular in material science and battery research [88-91]. Specifically, machine learning assisted failure estimation attracts great attention [92]. Wu et al. [93] combined importance sampling and forward feed neural network for online prediction. They defined remaining useful life (RUL) as the difference in voltage curves of constant current charge. Hu et al. [94] used more than 10 years cycling data to validate a k-nearest neighbor (kNN) regression based estimator. Support vector machine (SVM) based methods are also extensively studied in this field [95, 96]. Severson et al. [97] developed a novel feature extraction and processing approach to detect battery failure at early time. 124 commercial batteries were cycled using accelerating tests, providing most comprehensive dataset for battery data-driven research so far.

But existing data-driven models for battery have some inherent limitations. First, most studies only consider commercialized LIB [93, 97, 98]. Which is based on graphite for anode and transition metal oxide for cathode. Due to existing electrode materials has low theoretical capacity (372 mAh/g for graphite), it cannot satisfy the growing market demand. Various next generation high capacity with long lifetime electrode materials have been proved to be very promising [99]. Such materials have totally different reaction mechanisms with lithium ions. For example, Si has alloying lithium ions, rather than the intercalation for that of graphite. Therefore, the degradation modes are distinctive. High capacity induced extreme volume change makes failure prediction of next generation LIB even more challenging. Unfortunately, there is no data-driven research on this new field. Secondly, due to previous data-driven research for LIB relies on commercialized battery, typical studies exposed batteries to different working conditions from mild to stressed and compared performance difference. Those results can guide us how to use battery with extended lifetime, but fail to answer a more fundamental question: How can we optimize the materials or electrode design to increase battery lifetime. None of current data-driven research took electrode material properties into consideration, leaving great space for improvement. Finally, most studies combining experimental results with machine learning suffered from data sparsity issue. It's very costly to generate enough experimental data for advanced machine learning models, such as neural network. For a typical battery, either laboratory or commercialized, it takes several months or even years to cycle until terminal condition. Without enough data, it's easy to have overfitted models and unrealized results. There should be an universal framework to guide how to collect easy accessible features and make complete recording. So that the research community can share comparable works.

To address as-mentioned challenges, this work innovates in several aspects. Rather than graphite, the completely new anode material BP is considered. BP has high theoretical capacity of 2,596 mAh/g with long term stability [100, 101]. All materials were synthesized from raw powders in our own lab over past several years, ensuring the consistency and comparability. The coin cell fabrication process is under careful control without significant variability. Using half coin cells with lithium foil as counter electrode removes the degradation effect from cathode, simplifying the analysis. More than 90 cells were divided into 16 batches with different materials-level properties and synthesis conditions. The cycled results are summarized and processed for machine learning prediction. Beyond conventional cycling trajectory and capacity information, most important materials properties are extracted for modeling, thanks to the in-house fabrication enables us to track entire fabrication process.

The modeling results confirm the importance of incorporating materials properties in failure estimation. Such information can be measured before cycling, and used to guide materials synthesis and electrode fabrication. Not only do material properties indicate the speed of degradation, they can also help to choose the cycling procedure to prevent too aggressive cycling for specific batteries. For high capacity anode like BP, the degradation is more unpredictable.

5.2 Dataset Preparation and Feature Extraction

To make different electrodes comparable, the overall materials synthesis, electrode/coin cell fabrication, battery cycling test protocol are outlined in 2.2. In the BP synthesis process, 6 hour HEMM is used to transform RP to BP. The major difference is ball milling time for BPG composite synthesis, ranging from 1 to 24 hours. During electrode fabrication, processing variation introduces five major difference for electrode. First, the electrode thickness of 16 groups is from 22 to 100.6 µm, as shown in Figure S 20. The thickness is used as index to sort 16 batches. This is purposely controlled to study the effect of material loading on battery electrochemical performance. As a result, the specific material loading is between 1.91 to 5.57 mg/cm^2 shown in Table 5.1. It should be noted here that material loading doesn't increase linearly with electrode thickness, due to electrode porosity and density varies. The ratio between material loading and thickness can be implicitly treated as electrode porosity or compactness. The electrode composition influences material density as well. The second materials related difference is ratio of BP in the active material. This is studied alone in 2.3.3. A more comprehensive ratio coverage between 40% to 75% is considered here. It is expected to validate previous conclusion using the new richer dataset. The homogeneity of electrode is another important consideration in manufacturing. Homogeneous BP distribution ensures uniform volume change, preventing fracture and cracks growth. However, there is no direct value of electrode homogeneity can be measured easily. Instead, we use electrode surface roughness in Figure S 22 as an approximate indicator for electrode, because of their positive correlation. Inhomogeneous BP distribution usually causes the electrode surface to be very rough. Finally, we use an image processing software on electrode surface SEM images to measure the BP particle size distribution and average size. BP particles have lower electronic conductivity, compared to surrounding graphite and carbon black. The brighter region in SEM attributes to BP. The resulting average particles size is between 1.11 to 5.87 µm (Figure S 21), agreeing well with precise laser diffraction based measurement in 2.3.1. Compared to laser infraction based particle size measurement, image based method has much higher productivity. It only takes few minutes to take images from different perspectives and reconstruct 3D rendering. In electrochemical cycling, the only variable is the constant current density, between 0.025 to 2.5 C-rate (only using BP weight in calculation). This range mostly covers the interested current density of energy-type and power-type batteries. But it doesn't increase linearly, with heavy tail right skewness. The summary of as-mentioned variables for 16 groups battery is provided in Table 5.1. For more detailed characterization results, refer to Appendix 6.

Table 5.1 Key materials properties for 16 groups of BP-based LIB

# of group	***electrode thickness (µm)***	***material loading (mg/cm^2)***	***ratio of BP in active material***	***surface roughness (µm)***	***particle size(µm)***	***ball milling time (h)***
1	100.6	5.56	0.55	2.64	1.11	12
2	83.2	5.13	0.5	2.224	3.54	24
3	77.5	4.28	0.5	1.646	1.76	12
4	72.5	4.55	0.6	1.215	5.25	1
5	71.6	3.61	0.6	1.88	2.48	12
6	69.7	3.50	0.45	1.22	1.61	24
7	65.7	3.76	0.45	1.734	2.53	12
8	61.9	3.41	0.7	2.154	3.2	6
9	56.1	2.93	0.5	0.687	1.09	24
10	55.2	3.54	0.4	2.086	5.87	3

11	54.2	3.21	0.75	1.013	2.3	12
12	52.3	3.60	0.55	2.208	1.29	12
13	51.3	2.61	0.5	1.036	2.73	8
14	48.4	3.33	0.5	0.893	1.32	24
15	37.7	2.33	0.7	0.583	1.34	12
16	22	1.91	0.5	0.885	2.61	6

The first 50 cycles discharging capacity of 90 cells in 16 groups are plotted in Figure 5.1. The value is normalized based on 1st cycle capacity, or called SOH. It can be easily identified that different groups show distinctive degradation patterns with varying current densities. Overall, completely degraded samples (< 50% SOH after 50 cycles) usually show fast degradation in the first 10~20 cycles. This nonlinear property is rarely seen in commercialized graphite-based LIB, may corresponding to idiosyncratic degradation mechanisms associated with high capacity materials, which complicates the data-driven work. Therefore, in the modeling part, nonlinear classifiers are included.

Another interesting observations is slow materials activation especially for thicker samples (group 1~8) with high current densities. Initial capacity is normalized at 1.0, while later on remaining capacity will be higher. There exist many explanations for this phenomenon. First, the electrolyte may not soak electrode well initially, particularly for those thick and condense electrodes. During volume change upon charging/discharging, the gap between particles increases, allowing electrolyte to infiltrate into. The lagged material activation may mislead capacity degradation analysis. And initial higher volume change rate on the surface further introduces inhomogeneity problem, which could accelerate degradation afterward.

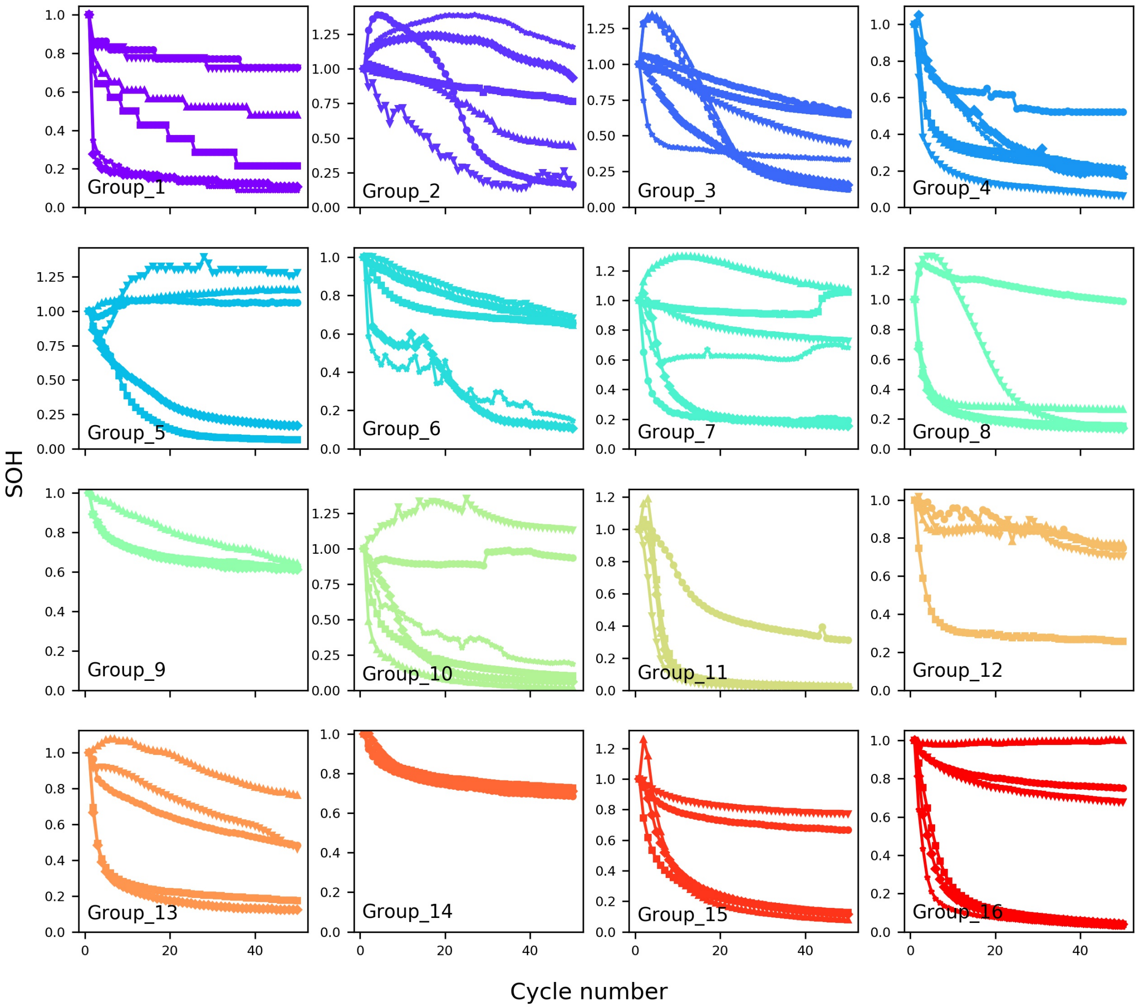

Figure 5.1 Normalized capacity profiles for 16 groups of BP-based LIB between 1st and 50th cycle

After obtaining the capacity profiles, three additional cycling related features are extracted. They are 1st cycle Coulombic efficiency, 1st-to-2nd cycle and 2nd-to-10th cycle capacity drop ratio. As less as cycling related information is used here to make the prediction model more meaningful. In classifying good/bad performers, a suitable threshold should be selected. In this work, the reason why 50 cycle is set as cutoff value is based on the fact that for ‘dead’ battery, which is defined to be less than 50% SOH, all of them reach ‘dead’ status far early before 50 cycles. While for ‘survival’ battery, the capacity degradation trend become stable quickly before 50 cycles as well. Including more cycles cannot add useful information but require much longer experiment time.

Meanwhile, our purpose is to use early cycling information with key materials related properties to predict if battery will fast degrade. Long run behavior is out of the scope for current work.

Aggregating the ten features and applying standardization scaler to make them have the same scale, the Pearson correlation heatmap is plotted in Figure 5.2. In which, there are some relationships worth highlighting. First, 1st cycle Coulombic efficiency has high positive correlation to 1st-to-2nd cycle capacity drop. This is not surprising, as low Coulombic efficiency usually indicates large irreversible capacity loss from forming the SEI layer. However, there is almost no relationship between 1st cycle Coulombic efficiency and 2nd-to-10th cycle capacity drop. This implies that initial capacity degradation mechanism in activation process is different from the one after stabilization. And including both 1st-to-2nd cycle and 2nd-to-10th cycle capacity drop ratios is necessary to represent two stages degradation.

When considering the relationship between material properties and electrochemical features, the most important feature is 2nd-to-10th cycle capacity drop ratio. It has positive correlation to electrode thickness, material loading, surface roughness and ball milling time, while negative correlation to BP ratio. The positive correlation between electrode thickness/material loading and 2nd-to-10th cycle capacity drop ratio is somehow confusing. Usually, thicker electrode with higher specific material loading is expected to suffer larger capacity drop. Here, the counterintuitive positive relationship comes from formerly mentioned slow activation process for thick electrode. If newly exposed active material compensates the capacity loss during 2nd-to-10th, overall the battery could show less capacity loss or even increase. Positive correlation between ball milling time and 2nd-to-10th cycle capacity drop ratio can be attributed to solid connection between BP and carbon prevent electrode structural change and relieve capacity loss. The benefit is more obvious at the stable cycling stage, as the positive correlation between ball milling time and 1st-to-2nd cycle capacity drop ratio is lower than that of 2nd-to-10th one. Finally, not surprising, higher BP ratio in active material will cause faster capacity drop, again particularly for the stable cycling stage. Which matches the conclusion in 2.3.3. From above analysis, 2nd-to-10th cycle capacity drop ratio contains more information that 1st-to-2nd one, and has latent relationship to selected materials features. The numerical correlation coefficient can be related to physical domain knowledge in most conditions. Some unexpected results provide unique insights thanks to the systematic perspectives.

When only studying 6 materials related properties and their relationships, there are also some points of interest. Surface roughness is selected mainly for quantifying electrode inhomogeneity. It has very high positive correlation to the thickness/material loading. Which means that it is difficult to make uniform thick electrode. Thick electrode is vulnerable to inhomogeneous particle distribution, badly mixed slurry and uneven solvent evaporation rate during electrode fabrication. Reducing particle size can effectively increase electrode homogeneity, given their positive correlation. Getting to the root of the matter, extending ball milling time can reduce particle size shown by negative correlation in Figure 5.2. This effect slightly contrasts to observation in 2.3.1 where long time ball milling processing is found to have less influence on particle size. The contradiction comes from different particle size measurements. In 2.3.1, particle size is measured by Micromeritics based on light scattering. As a result, the measured size corresponds to primary particles suspending in water. In this chapter, the particle size refers to post processing from SEM surface image by comparing brightness. Given bright BP and dark graphite contact closely with each other. The composite has no clear edge for primary particles. Therefore, only secondary particles can be distinguished. Although ultrahigh positive correlation between electrode thickness and material loading is detected as expected, both of them are kept in modeling part, due to their ratio indirectly indicates porosity and density of the electrode. Finally, negative correlation between ball milling time and BP ratio doesn’t have any physical meaning as these two parameters are manually chosen.

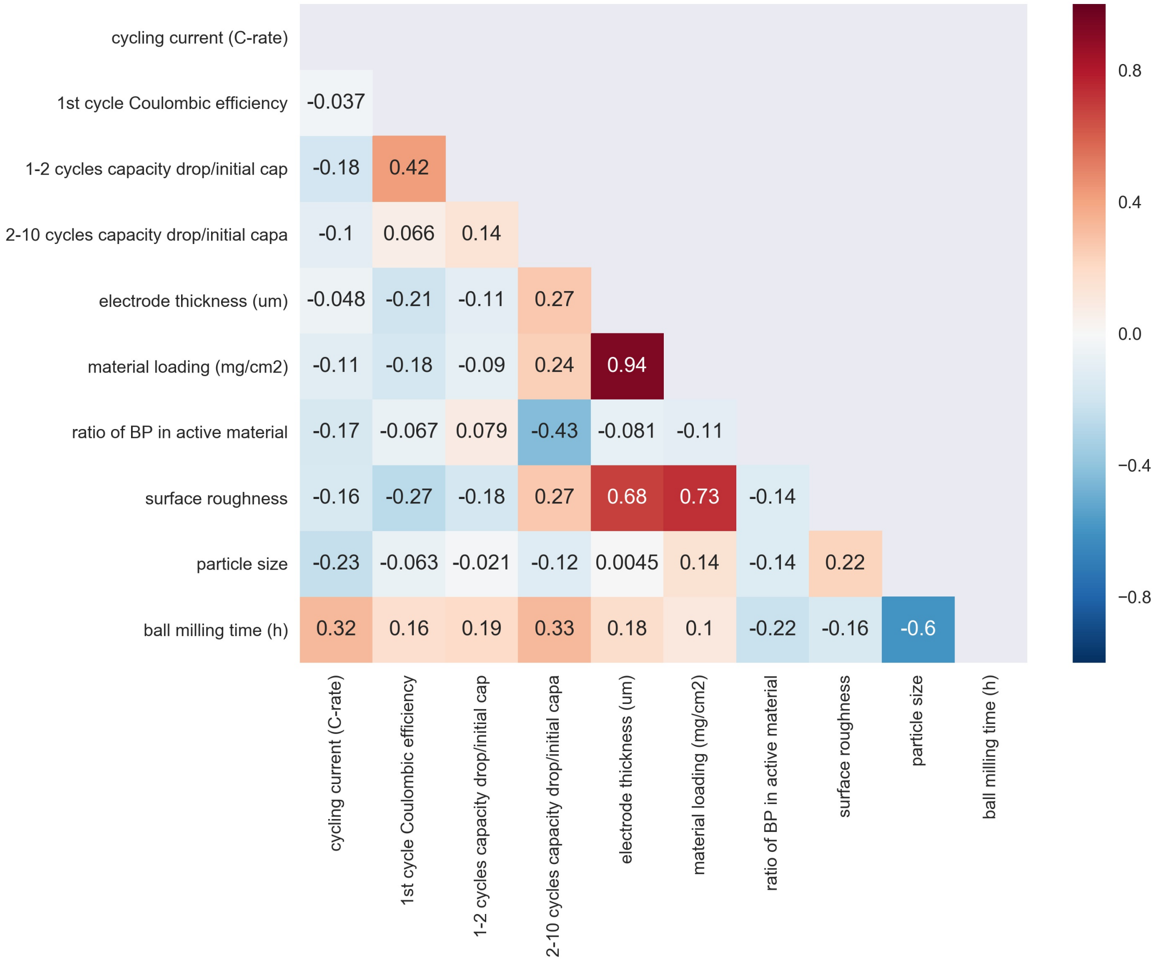

	cycling current (C-rate)	1st cycle Coulombic efficiency	1-2 cycles capacity drop/initial cap	2-10 cycles capacity drop/initial capa	electrode thickness (um)	material loading (mg/cm2)	ratio of BP in active material	surface roughness	particle size	ball milling time (h)
cycling current (C-rate)										
1st cycle Coulombic efficiency	-0.037									
1-2 cycles capacity drop/initial cap	-0.18	0.42								
2-10 cycles capacity drop/initial capa	-0.1	0.066	0.14							
electrode thickness (um)	-0.048	-0.21	-0.11	0.27						
material loading (mg/cm2)	-0.11	-0.18	-0.09	0.24	0.94					
ratio of BP in active material	-0.17	-0.067	0.079	-0.43	-0.081	-0.11				
surface roughness	-0.16	-0.27	-0.18	0.27	0.68	0.73	-0.14			
particle size	-0.23	-0.063	-0.021	-0.12	0.0045	0.14	-0.14	0.22		
ball milling time (h)	0.32	0.16	0.19	0.33	0.18	0.1	-0.22	-0.16	-0.6	

Figure 5.2 Correlation matrix of Pearson coefficients between selected features

5.3 Using Machine Learning Models to Predict Battery Failure

5.3.1 Modeling

In 5.2, pairwise feature correlations are analyzed as a preliminary step to check if it’s compatible with the physicochemical knowledge. While, we don’t find the ultimate relations between those features with battery failure behaviors. Besides validating pure experimental observation in Chapter 2, we aim to build models that are able to predict the degradation of battery in different group using extracted features.

Here we use 50% SOH after 50 cycles as threshold to separate ‘dead’ and ‘alive’ batteries. This is lower than traditional setting of 80%. The main reason is high capacity BP anode has much faster capacity drop. And it happens in the initial several cycles. This forms a typical binary classification machine learning problem, where many mature algorithms can be leveraged to fit the same dataset but provide different insights.

In the training process, to make robust prediction, the original dataset is feed for a 5-fold cross validation. The ratio between training and testing set is 80%:20% in each iteration. Here, five groups of classification models are fitted, shown in Table 5.2. The *Accuracy* is defined as average accuracy in testing set over 5 folds. The *F1 score* is the harmonic mean of precision and recall, also average over 5 folds. Standard deviation is added correspondingly. In the *Hyperparameters* column, key hyperparameters achieving best *Accuracy* and *F1 score* are provided. Overall for individual models. The model performance is consistent, not subject to great change with parameter tuning.

Table 5.2 Accuracy and F1 score with different classifiers

classifier	*Accuracy*	*F1 score*	*Hyperparameters*
Logistic regression(l1)	0.87±0.04	0.86±0.04	“C”: 5.0, “penalty”: “l1”
Logistic regression(l2)	0.86±0.04	0.85±0.05	“C”: 1.0, “penalty”: “l2”
SVC(rbf)	0.82±0.07	0.81±0.08	“C”: 1.0
LinearSVC(l1)	0.87±0.04	0.86±0.04	“C”: 1.0, “penalty”: “l1”
LinearSVC(l2)	0.87±0.06	0.87±0.06	“C”: 1.0, “penalty”: “l2”
KNN	0.82±0.04	0.82±0.05	“n_neighbors”: 5

Random forest	0.86±0.04	0.86±0.05	“n_estimators”:100 “max_depth”: 3

The optimized models deliver good and similar prediction performance. For *Logistic regression* (l1/l2 regularized) and LinearSVC (l1/l2 regularized), the overall prediction accuracy and F1 score are higher than 0.85, with moderate standard deviation. As Both of them are known for linear models, the good performance matches our domain knowledge that the selected predictors have monotonically directional influence on battery degradation. For example, higher BP ratio is always associated with worse performers. This is the same to the observation in 2.3.3. High BP ratio samples have boosted initial capacity but fast degradation, due to dramatic volume change, fewer electronic connection and more SEI deposition. Previously, only qualitative description can be obtained. Using the data-driven models, it is easy to quantitatively compare the importance of different features and their relationship.

5.3.2 Results and Interpretation

The logistic regression with L1 penalty (Least Absolute Shrinkage and Selection Operation or LASSO) is known for reducing the coefficients of features without explanation power to be zero. In the Figure 5.3(a), the coefficients of features are plotted. The relative amplitude provides the significance of corresponding feature. The sign tells directional information. Here the 2^{nd}-to-10^{th} cycle capacity drop ratio is removed. It has too strong influence on the model results. Because most dead batteries actually loss 50% SOH after the initial 10-20 cycles. Including 2^{nd}-to-10^{th} cycle capacity drop ratio conflicts our intention to use preliminary features before degradation to predict degradation. The coefficients importance with 2^{nd}-to-10^{th} cycle capacity drop ratio is shown in Figure S 23.

First, in material properties group, surface roughness and materials loading are found to be non-influential. This is not surprising. First, surface roughness is only measured at five local points on the electrode at sub-micro scale. This may not be able to reflect the entire electrode condition. Surface roughness is just used as a substitute for the inhomogeneity of electrode. But the scope of inhomogeneity is far beyond surficial property. It involves compositional, morphological and physicochemical reaction inhomogeneity. It is hard to wrap up all of them into a single factor. And some of them are difficult to be quantified. For material loading, it is highly correlated to electrode thickness. Both of them have little influence in the LASSO model. This can be attributed to their narrow range as shown in Figure S 20. To make the electrode practical, we keep the thickness (material loading as well) in a reasonable range, between 20 to 100 µm. Which is comparable to commercialized graphite anode with about 50 to 100 µm thickness. So either positive effect from thin electrode or negative effect from thick electrode will not be apparent. In the electrochemical features group, 1st cycle Coulombic efficiency is not very important. This further consolidates previous observation that 1st cycle activation process is distinctive to stable cycles afterward. However, our target is to predict terminal failure here. But even though as mentioned features are numerically trivial in the LASSO, it's dangerous to conclude that they are useless at all. The model itself is subject to limited data points obtained from experiment. It doesn't account for all possibilities. Meanwhile, LASSO results are very sensitive to the magnitude of regularizer. Increasing penalty term can easily shrink more descriptors, while decreasing penalty term exaggerate their effects. The regularizer is selected to achieve best validation outcome and match predominant experimental knowledge.

Long ball milling time, small particle size and low BP ratio mitigate battery degradation. Which are not beyond original understanding. But the relative degree of influence between particle size and BP ratio worth noting. Particle fracture and electrode cracks are observed in Figure 2.9 and Figure 2.11. Indeed, particle fracture is just micron-scale degradation and electrode crack is more macro-scale phenomenon. If particle size is related to particle fracture and BP ratio to electrode crack, we can quantitatively compare electrode crack has twofold influence more than particle level break. When optimize an electrode, suitable macro-scale design to prevent electrode pulverization is more effective than many expensive nano-engineering on single particle.

After battery is assembled, the only parameter can be tuned is just the cycling density. The importance of cycling density is confirmed in Figure 5.3(a). It's smaller than BP ratio and almost equal to ball milling time and particle size. Which means that only reducing current density to expect maintain a long cycling lifetime battery is impossible, without good materials quality. This result justifies again the importance of incorporating materials predictors in the data-driven framework.

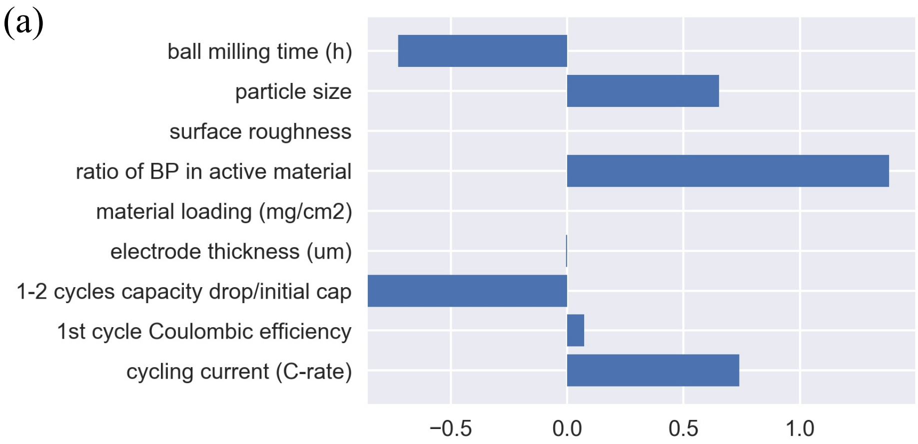

(b)

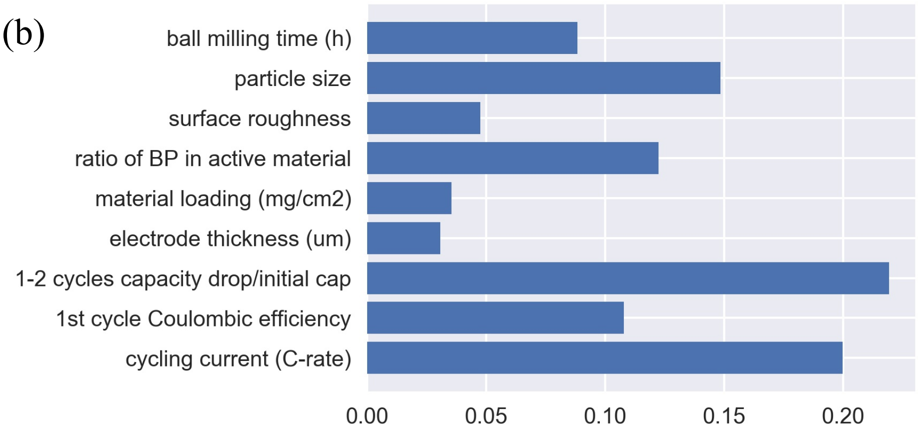

Figure 5.3 Coefficients fitted from the (a) logistic regression on l1 penalty (LASSO) and (b) Random Forest

Above analysis is only based on the linear model LASSO. However, the relations among different features could be nonlinear. And we purposely want to make most of all features information. Therefore, random forest with maximum depth 3 are fitted here. At each tree node, Gini index is selected as the splitting criterion to pick up feature with highest purity gain, from subset of 6 random features. The feature importance is spread out as shown by Figure 5.3 (b).

The reduced features in LASSO, such as surface roughness and materials loading, appear in RF. Admittedly, they are still small in magnitude compared to other features. Which cross validates two models. But particle size in RF is found to be more important than BP ratio. Which contradicts to LASSO results. This contrast comes from the way how RF deals with continuous and discrete variables. For particle size, it is a continuous variable between 1.09 and 5.87 µm. While BP ratio is manually selected discrete value. For a single decision tree, it can split using a continuous feature multiple time, so that the cumulative information gain will be large. It only splits once if the discrete feature is used. As a result, the importance will be biased to continuous feature like particle size.

When comparing material feature group and cycling feature group, RF treats cycling features be more important. Both 1-2 capacity drop ratio and current density are dominant to material features. This can be attributed to the coupled effect in cycling features. As the selected materials properties are physically independent to each other and represent different aspects, electrochemical cycling features are more inherently related. RF is able to detect the implicit relation and better than linear model from this perspective.

5.4 Summary

Correct estimation of LIB degradation requires in-depth understanding of the experimental observations, physical mechanisms and numerical modeling. In this chapter, we extend our study of BP material from a new perspective, using so far the most comprehensive cycling test results to systematically investigate the influence of multiple materials properties on the battery degradation, assisted by early cycling electrochemical information.

After collecting 90 cycled batteries, 16 batches are formed according to their synthesis procedure. Here, we purposely differentiate the batches by varying some key electrode-level and particle-level material qualities, like electrode thickness, material loading, active materials ratio, electrode homogeneity, average particle size and ball milling time. These features are found to be influential for battery failure in Chapter 2-4. However, there is no generic framework to include all of them and compare individual's contribution. Pairwise correlation analysis reveals latent relations between key material property and early cycling features. The 2^{nd}-to-10^{th} cycle capacity drop ratio contains most information for the stable cycling phase. Its strong correlation between several material characteristics can be explained by mechanistic knowledge.

To further quantify effects of different features and make prediction, multiple linear and non-linear machine learning models are trained here. The accuracy and precision of prediction are high in most models. This indicates the effectiveness of selected features. Because of the easiness of obtaining those features, the analytics framework can be extended to estimate the electrode failure trend of the BP or other high capacity materials based LIB at early cycling stage. Meanwhile, the quantitative analysis enables us to rank and compare the importance of different features and provide optimization suggestions. Linear model (such as LASSO) and non-linear model (such as RF) show similar sensitivity to materials properties. In which, active material ratio, particle size and ball milling time are three major influencers.

Chapter 6

Conclusions and Future Work

6.1 Summary

In this dissertation, a new anodic material used in LIB, black phosphorus, is studied with respect to material fundamental, synthesis optimization, degradation analysis and electrochemical characterization. It paves the way of large scale commercializing BP in renewable energy industry at moderate cost with superb performance.

In Chapter 2, HEMM, the most widely used synthesis method for BP, is improved. Parametric study on BP weight ratio shows a low ratio of BP ($BP_{0.3}G_1$) is structurally stable with solid P-C bonding. Upon cycling induced volume expansion and contraction, P-C bond maintains electronic contact and prevents capacity loss. Distinctive morphological and structural change between $BP_{0.3}G_1$ and $BP_{0.9}G_1$ after cycling proves that electrochemical performance is highly related to electrode composition and mechanical stability. Fast degradation is usually associated with electrode cracks and particle fractures. Additionally, other factors, such as electrolyte additives, ball milling time and material loading, affect the cycling performance as well. FEC additive can stabilize the SEI formation. Which affects the initial activation process significantly. The procedure combining shaker-model and planetary-mode ball milling technologies is proposed to synthesize optimal BPG composite. The resultant achieves superior high initial capacity and long term reversibility. HEMM process forms strong P-C bonding while PBM makes homogeneous composite. Alternative BP degradation mechanisms are BP oxidation and the formation of impurity phase, like Cu_3P, during fabrication.

Using HEMM-synthesized BP as precursor, a pulse laser assisted liquid phase exfoliation technique is developed in Chapter 3. The new method is scalable and cost efficient. More important, the intrinsic ambient instability of phosphorene is partially solved by using polycrystalline BP as starting materials. The retained polycrystalline structure after exfoliation is more durable to humidity and oxygen exposure, compared to pristine monocrystalline phosphorene. Liquid phase processing brings additional protective layer onto the phosphorene, further isolating moisture and air contact. These advantages make it practical to use the phosphorene in battery application.

An innovative top-down hybrid exfoliation method for phosphorene and graphene is developed in Chapter 4. This alters the tradition of exfoliating graphene and phosphorene separately and then combine with loose connection. The promising advantage of new two-down method is that the solid P-C chemical connection can be established first using HEMM and then subject to liquid exfoliation without breaking. The connection condition is previously determined to be very important for good battery performance. We leveraged multiple advanced characterization methods to support the hypothesis. The modified method produces fine, homogeneous and intimately contacted phosphorene and graphene. Consequently, the composite materials show super high reversible capacity and more than 500 stable cycles at elevated current densities. Through GITT, EIS and CV electrochemical characterizations, we found fast ion solid phase transport, low overpotentials and pseudo capacitive effect together contribute to the kinetics improvement. Meanwhile, negligible structural change before and after cycling ensure little capacity fade. There is no obvious crack observed. And the electrode’s mechanical strength property doesn’t change.

Based on experimental studies, a comprehensive dataset for BP-based LIB is collected in Chapter 5. The extracted material and cycling related features are used for fitting data-driven models to predict the degradation behavior of battery. The high accuracy and precision prove the effectiveness of selected features. By correlation analysis, strong relationship between material property and electrochemical performance can be detected. Empirical physical law based understanding for battery failure is quantified and validated by the numerical results. It can be concluded that introducing customized material properties is very necessary, different from other pure cycling results based models, especially for early anomaly detection. By comparing different descriptors' importance from linear and nonlinear models, some suggestions for further optimizing material synthesis and electrode design are provided.

6.2 Future Work Outlook

BP is prototyped to be the next generation anode material in LIB in this dissertation. There are some additional steps before use it in the real working scenario. So far, the safety issue is not considered in this work. In the RF transformation process, oxygen should be strictly avoided. Although BP is much more stable than RP and white phosphorus, it is still ignitable when temperature is high. When compositing with carbon source, like graphite and carbon black, this problem is even more serious. Direct modifying the material to prevent fire is not easy. Suitable case and module design are vital to ensure battery safety. Another common problem for phosphorene is high surface area induced consumption of electrolyte. In research area, the amount of electrolyte is not a major concern when assembling coin cell. It is usually excessive. But in reality, extra electrolyte will reduce battery volumetric specific capacity and increase cost. Choosing suitable electrolyte with proper additives for BP-based LIB should be researched accordingly. Finally, data-driven models for battery degradation prediction using state-of-the-art machine learning models is a rising field. But very few works focus on alternative materials other than graphite. Considering the dramatic difference in reaction mechanism and volume change mode, previous models built on graphite data cannot be directly transferred to BP. More available data and comparable experiment set up are necessary to flourish this exciting field.

Appendix

Appendix 1. Other Possible Failure Mechanisms in BP-based Anode

As demonstrated, mechanical failure was mainly responsible for the capacity fade observed in BP-based anodes. However, there are still unknown failure/degradation mechanisms that need to be explored. Herein, we briefly discuss two possible mechanisms that might underlie the poor cycle life of BP-based anodes. Although further research will be required to understand how these mechanisms are correlated with the cycle performance of BP-based an- odes, it is worthwhile to discuss these issues to have a better understanding of the BP-based anode.

The pristine BP surface is hydrophobic, but it changes to hydrophilic progressively through oxidation [102]. It was observed that air moisture can be adsorbed on the surface of BP-based electrodes due to the highly hydrophilic nature of BP. Upon exposure to air, the smooth surface of BP electrode changes to an extremely rough surface with many defects. However, the BP electrode stored in an Ar-filled glove box did not show any changes in the surface (Figure S 1). This suggests that the BP-based anode is prone to degrade upon exposure to ambient conditions. It should be mentioned that the adsorption behavior of the BP electrode occurred in a short period of time. As shown in the microscope images (Figure S 2), the surface of BP electrode was blurred quickly because the height of the surface was considerably changed by adsorbing moisture. These results suggest that oxygen and moisture-free synthesis environment is very important to obtain high purity of BP. More importantly, these suggest that the capacity degradation of BP-based anodes might be correlated to the electrode's structural disruption induced by BP's hydrophilic nature upon oxidation. It is generally accepted that a significant amount of oxygen and moisture is generated in a battery cell due to electrolyte decomposition or side reactions. Not only large volume change but also BP's hydrophilic nature by oxidation might affect the mechanical degradation of BP-based anodes. Since $BP_{0.9}G_1$ has a higher amount of BP than $BP_{0.3}G_1$, stronger hydrophilic nature of $BP_{0.9}G_1$ might affect the mechanical degradation. In fact, we observed that the cycled $BP_{0.9}G_1$ electrode was severely wrinkled and bent upon exposure to air.

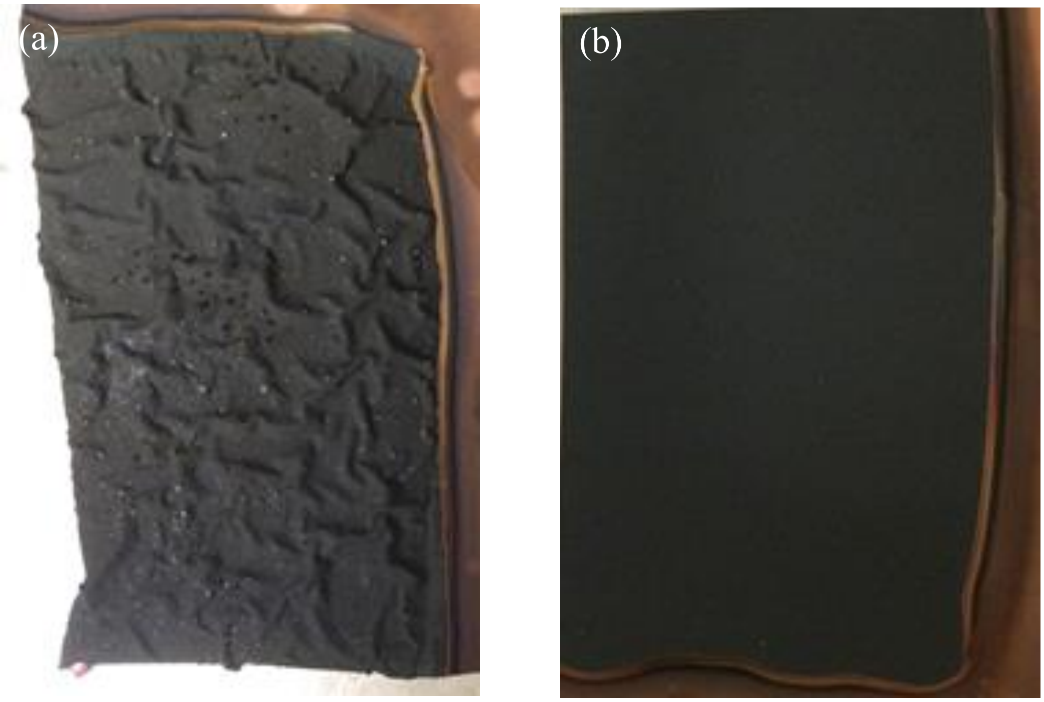

Figure S 1. Comparison of the BP electrode stored in air and the BP electrode stored in glovebox: (a) BP electrode after storage for 2 weeks in air, (b) BP electrode after storage for 2 weeks in glovebox.

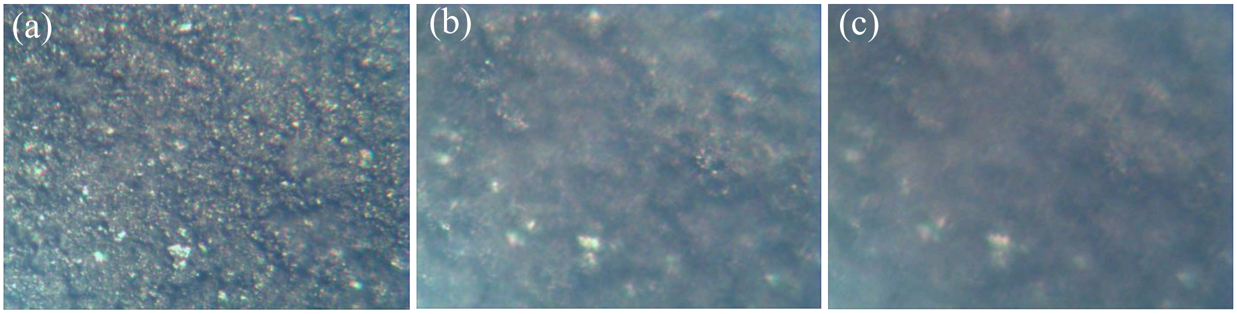

Figure S 2. The change in the microscope image of BP electrode over time: (a) Original state, (b) after 20 h in air, (c) after 48 h in air

Formation of Cu_3P might be another reason for the mechanical failure of BP-based electrodes. As discussed in a previous study [25], the electrode preparation procedure should be done carefully to avoid the formation of Cu_3P on the Cu current collector. In our study, we found that electrode drying temperature and time, BP particle size, and the type of binder contribute to the formation of Cu_3P in the BP-based anode (Figure S 3). At the particle level, the formation of Cu_3P might be beneficial in terms of electrochemical performance since Cu_3P is also an electrochemically active material with lithium. At the electrode level, however, the formation of Cu_3P could be detrimental in terms of mechanical stability of the electrode. It was observed that the significant formation of Cu_3P phase wrinkles the BP-based electrode and causes many defects. This might be due to the strong attraction force induced by locally formed Cu_3P in the BP electrode. It is worthwhile to mention that more attention should be paid to P-C composites with a high ratio of P when the electrode is made. Since a P-C composite with a high content of P (like $BP_{0.9}G_1$) contains a considerable amount of P, it is more susceptible to Cu_3P phase formation than a P-C composite with a low ratio of P. Further studies are needed to understand the correlation between Cu_3P formation and the mechanical degradation of BP-based electrodes.

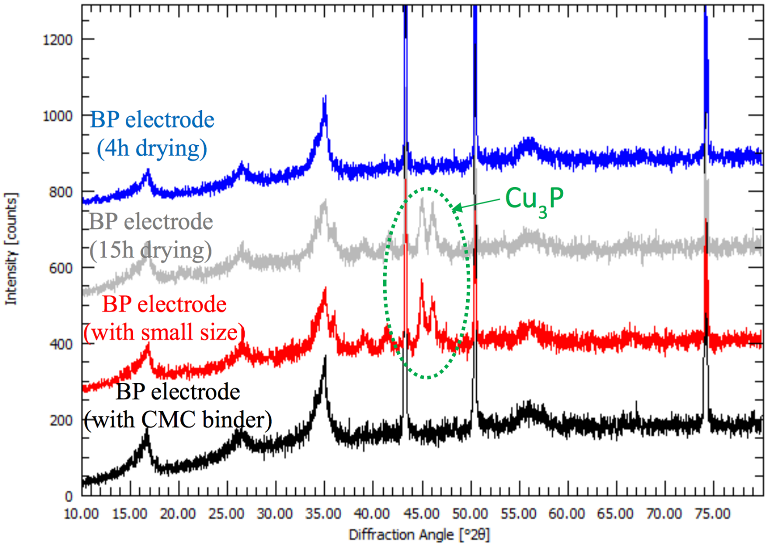

Figure S 3. Cu_3P phase formation of BP electrodes at different conditions.

Appendix 2. Effects of Electrolyte Additive on Cyclability

To quantitatively evaluate how much BP-G electrochemical performance could be improved by electrolyte additive, both $BP_{0.3}G_1$ and $BP_{0.9}G_1$ electrodes were cycled with and without FEC additive. FEC is a well-known electrolyte additive that contributes to the formation of a robust FEC-derived SEI layer that is much thinner and denser than an FEC-free SEI layer, helping this layer to withstand the stress caused by large volume expansion/contraction upon lithiation/delithiation [103].

Figure S 4(a) shows the cycle performance of $BP_{0.9}G_1$ electrodes with and without FEC additive. The use of FEC additive did not improve the dramatic capacity fade of $BP_{0.9}G_1$, indicating that the formation of a robust and flexible FEC-derived SEI layer did not mitigate its mechanical degradation. This further confirms that mechanical failure, rather than SEI, was the predominant degradation mechanism implicated in the capacity fade of $BP_{0.9}G_1$, consistent with our earlier work [101]. For $BP_{0.9}G_1$, only the initial reversible capacity increased with the use of FEC additive. This could be because the FEC-derived SEI layer permits faster Li-ion transport at the electrode/electrolyte interface, thereby enhancing the utilization of BP-G active materials within a given amount of time [103].

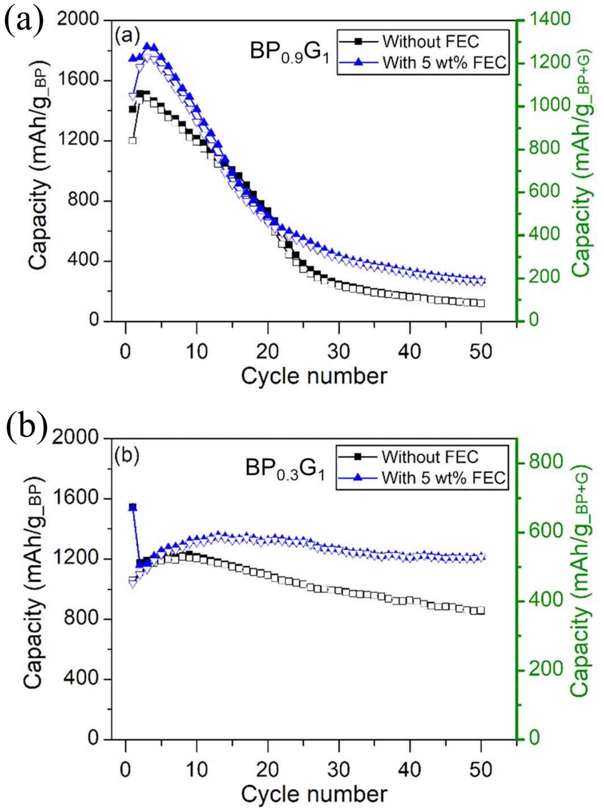

Figure S 4. Cycle performance of 6h-HEMM BP-G composites with (blue) and without (black) FEC additive. (a) $BP_{0.9}G_1$ and (b) $BP_{0.3}G_1$ were cycled between 2.0 – 0.01 V (vs. Li^+/Li) at the same C-rate (C/7, which corresponds to 200 mA/g for $BP_{0.3}G_1$ and 270 mA/g for $BP_{0.9}G_1$). The active material (BP + G) loading was between 3.5 to 4.0 mg/cm^2. Open and closed symbols represent charge (delithiation) and discharge (lithiation) capacities, respectively. The specific capacity is displayed based on either BP weight (left axis, black) or BP + G weight (right axis, green).

For $BP_{0.3}G_1$ (Figure S 4(b)), capacity retention was notably improved with FEC additive. The specific capacity (delithiation) of the FEC- containing cell reached 1357 mAh/g (BP weight-based) at the 13th cycle and had retained 1213 mAh/g upon the 50th cycle, showing an approximate 90% capacity retention. In contrast, the FEC-free cell achieved a maximum capacity of 1222 mAh/g at the 6th cycle, but the capacity dropped to 853 mAh/g at the end of cycling, showing an approximate 70% capacity retention. The slight increase in reversible capacity during the initial cycles could be due to a slower electrolyte wetting rate caused by thicker BP-G electrodes with high active material loadings and the significant amount of hydrophobic carbons present in $BP_{0.3}G_1$.

The improvement in capacity retention of the FEC-containing cell suggests that the capacity fade of $BP_{0.3}G_1$ mainly occurred at the electrode/electrolyte interface, with the dominant degradation mechanism being SEI growth caused by further electrolyte decomposition, rather than electrical contact loss caused by severe particle cracking or pulverization. If cracking or pulverization of particles was pronounced in $BP_{0.3}G_1$, FEC should not have affected cycle performance, as it did for $BP_{0.9}G_1$. Nevertheless, minor cracks present in some large $BP_{0.3}G_1$ particles may also contribute to further electrolyte decomposition and the subsequent formation of a thick SEI layer.

The improvement in capacity retention can thus be attributed to the characteristics of the FEC-derived SEI layer, which has excellent mechanical stability that allows it to withstand considerable stress during the lithiation/delithiation process and possesses superior passivation that mitigates further side reactions between anode and electrolyte. To investigate how the FEC additive improved the capacity retention of $BP_{0.3}G_1$, the EIS spectra of FEC-free and FEC-containing cells were evaluated after the 50th cycle. As shown in Figure S 5(a), the impedance spectra display depressed semicircles in the high-medium frequency range, representative of SEI layer resistance (R_{SEI}) and charge transfer resistance (R_{ct}), and an inclined line in the low-frequency range assigned to solid-state diffusion inside particles. Distinct differences between FEC-containing and FEC-free cells were observed in the depressed semicircles. Based on the equivalent circuit model (Figure S 5(b)) used to fit the EIS data, the R_{SEI} and R_{ct} of the FEC-containing cell were lower than those of the FEC-free cell after 50 cycles. This indicates that the thick SEI layer formation and sluggish charge transfer reaction occurring in $BP_{0.3}G_1$ was alleviated by the use of FEC additive. In an FEC-free cell, thick SEI layers formed due to severe electrolyte decomposition resulting from unstable SEI layers and minor cracks in particles. In contrast, the

FEC-containing cell maintained stable SEI layers, suppressing SEI growth and improving interfacial kinetics. Although the FEC-free cell exhibited higher interfacial resistances (R_{SEI} and R_{ct}) than the FEC-containing cell, it still showed well-defined semicircles in the high-mid frequency range and a similar slope for the inclined line in the low-frequency range to those of FEC-containing cells. This indicates that $BP_{0.3}G_1$ has no severe structural disruptions or electrical contact loss, maintaining charge transfer and solid-state ion diffusion processes. This further proves that the capacity degradation of $BP_{0.3}G_1$ is governed by the interfacial phenomena rather than by the electrical contact loss caused by particle cracking or pulverization.

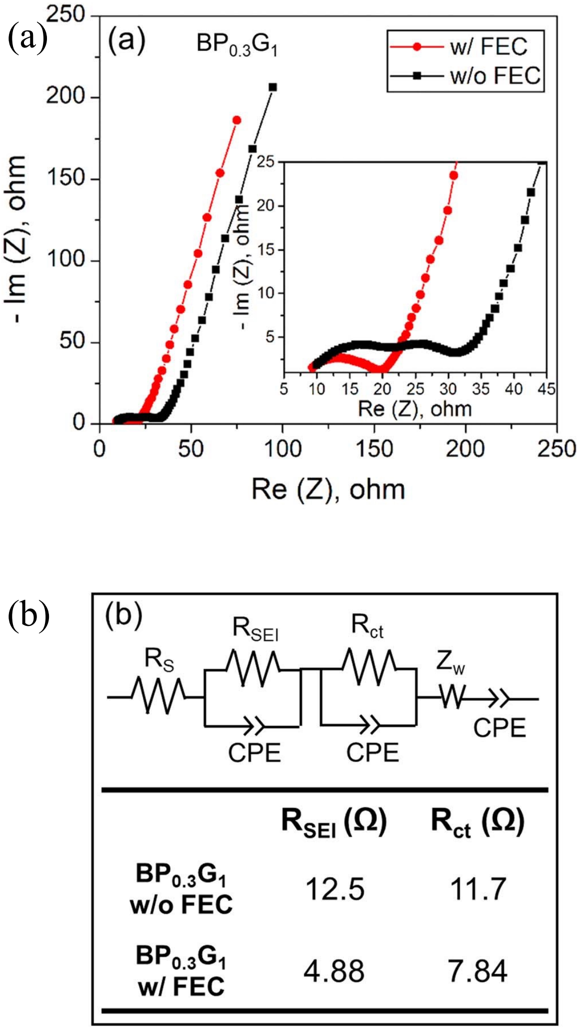

	R_{SEI} (Ω)	R_{ct} (Ω)
$BP_{0.3}G_1$ w/o FEC	12.5	11.7
$BP_{0.3}G_1$ w/ FEC	4.88	7.84

Figure S 5. (a) EIS spectra of $BP_{0.3}G_1$ electrodes after 50 cycles with (red) and without (black) FEC additive. (b) Equivalent circuit model used to fit the EIS spectra and the resulting interfacial resistance values.

Notably, the use of FEC additive had no influence on first cycle coulombic efficiency and initial reversible capacity of $BP_{0.3}G_1$, as shown in Figure S 4(b). The first cycle coulombic efficiency (69%) and initial reversible capacity (1058 mAh/$g_{\_BP}$) of FEC-free cells were similar to those (68% and 1039 mAh/$g_{\_BP}$) of FEC-containing cells.

Appendix 3. Effects of Ball Milling Time on Cyclability

Ball milling time is considered the most important parameter for synthesizing composite materials with HEMM [104]. Previous studies have used different ball milling times, which might explain the significant differences in P-C electrochemical performances among them [68]. Several processing variables affect HEMM process: type of milling, material of milling media, ball-to-powder ratio (BPR), milling atmosphere, milling time, milling speed, and size of milling media, and the ball milling time used in one study is thus not directly comparable with that used in another study [68]. Ball milling times, along with other HEMM synthesis conditions, must be consistent if comparisons are to be made.

We explored the different HEMM-produced BP-G composites and how the ball milling process therein affected electrochemical performance by synthesizing $BP_{0.3}G_1$ composites with different ball milling times and comparing their cyclability, initial reversible capacity, and first cycle coulombic efficiency. No electrolyte additive was used in the cells which might have confounded these assessments.

As shown in Figure S 6, increases in ball milling time were associated with improvements to both initial reversible capacity and first cycle coulombic efficiency in $BP_{0.3}G_1$. The first discharge (lithiation) and charge (delithiation) capacities of $BP_{0.3}G_1$ composites ball-milled for 6 h, 12 h, and 24 h were 1583/1105, 2104/1638, and 2440/1978 mAh/g (based on the weight of BP), respectively. The corresponding first cycle coulombic efficiencies were 69.8, 77.8, and 81.1%, respectively. These data indicate that longer HEMM allowed complete bonding of ball-milled disordered and/or nano-porous carbons to BP particles, thereby improving the activation of BP material. Shorter ball milling times resulted in a portion of BP particles remaining locally isolated from, or only loosely connected to, ball-milled carbons; these were not involved in the electrochemical reaction due to their low electronic conductivity. These isolated BP particles were also likely to be subject to severe mechanical degradation and the associated contact loss, further lowering the first cycle coulombic efficiency.

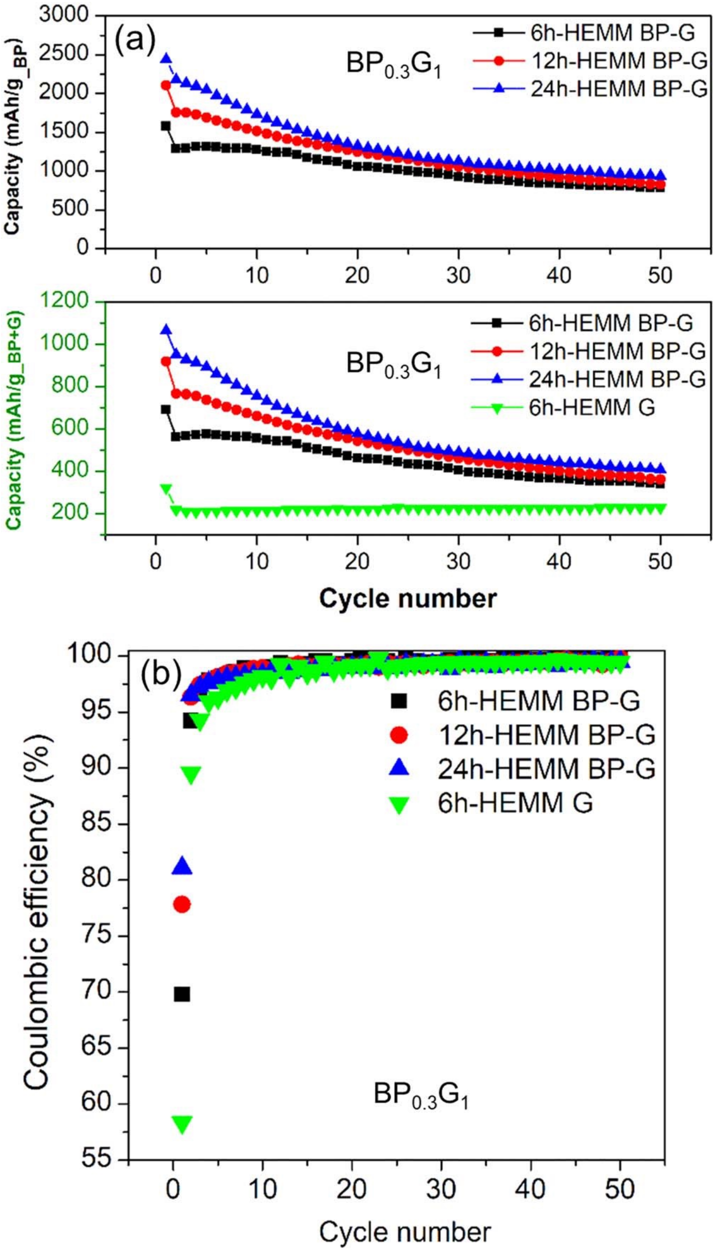

Figure S 6. (a) Cycle performance and (b) coulombic efficiency of $BP_{0.3}G_1$ composites synthesized with different HEMM synthesis times: 6h-HEMM (black square), 12h-HEMM (red circle), and 24h-HEMM (blue triangle). For comparison, 6h-HEMM synthesized graphite was included in the plot (green down-triangle). Cells were cycled without FEC additive between 2.0 – 0.01

V (vs. Li^+/Li) with a current density of 200 mA/g. The active material (BP + G) loading was between 4.0 to 4.4 mg/cm^2. The specific capacity (discharge, lithiation) is displayed based on either BP weight [top subfigure in (a)] or BP + G weight [bottom subfigure in (a)].

The strong connection between ball-milled carbon and BP (BP-G form) that accompanied with increased ball milling time was evaluated by comparing the electronic conductivities among BP-G composites ball-milled for different lengths of time. For comparison, the electronic conductivities of BP, graphite, and BP/G mixture electrodes are listed in Table S 1. As expected, the synthesized BP exhibited much lower electronic conductivity than graphite. As the graphite content in BP/G mixtures increased, the electronic conductivity of BP/G mixtures increased due to enhanced inter-particle conductivity via contributions from the graphite particles. However, it should be noted that the inner-particle conductivity of BP particles is not improved by the simple mixing process. The 6h-HEMM synthesized $BP_{0.3}G_1$, wherein the composition is the same as BP/G (44:56 wt%) mixture, had much lower conductivity (0.16 S/cm) than the corresponding BP/G mixture (4.87 S/cm), but much higher conductivity than BP. This is because BP are chemically bonded to carbon to generate BP-G composite particles (BP-G form), which improved the inner-particle conductivity although the inter-particle conductivity was lower. The BP-G particles no longer retain the original conductivities of BP or graphite because of their structural and bond changes. That is, the lowered electronic conductivity upon ball milling is the consequence of the material change from BP/G mixture to BP-G composite, indicating strong bonds between BP and carbon.

Table S 1. Electronic conductivity of BP, graphite, and two different BP/G mixtures

Active material	Composition	Conductivity (S/cm)
BP ball-milled for 6h	92.5:7.5 (AM: PvdF)	N/A (beyond the measurement range)
Pristine graphite	92.5:7.5 (AM: PvdF)	5.26×10^0
BP/G mixture (70:30 wt.%)	80:10:10 (AM:CB:PvdF)	1.36×10^0

BP/G mixture (44:56 wt.%)	80:10:10 (AM:CB:PvdF)	4.87×10^{0}

The difference between the BP/G mixture and BP-G composite forms in the BP-G electrode can be further elucidated with SEM images and EDAX analyses (Figure S 7). With sufficient ball milling time, the BP-G electrode contained predominantly the BP-G composite from wherein carbon and phosphorus were homogeneously distributed without any clear boundaries between the two elements, indicating that carbon and phosphorus were co-localized and bonded (Figure S 7 (a)). In contrast, the EDAX image of the BP/G mixture form showed that phosphorus was locally concentrated, with distinct boundaries between carbon and phosphorus elements (Figure S 7 (b)). With insufficient ball milling time, the BP/G mixture form, wherein BP particles are not chemically bonded to ball-milled carbons but simply mixed with graphite, was observable in the BP-G electrode and typically seen near large BP particles (>5 μm).

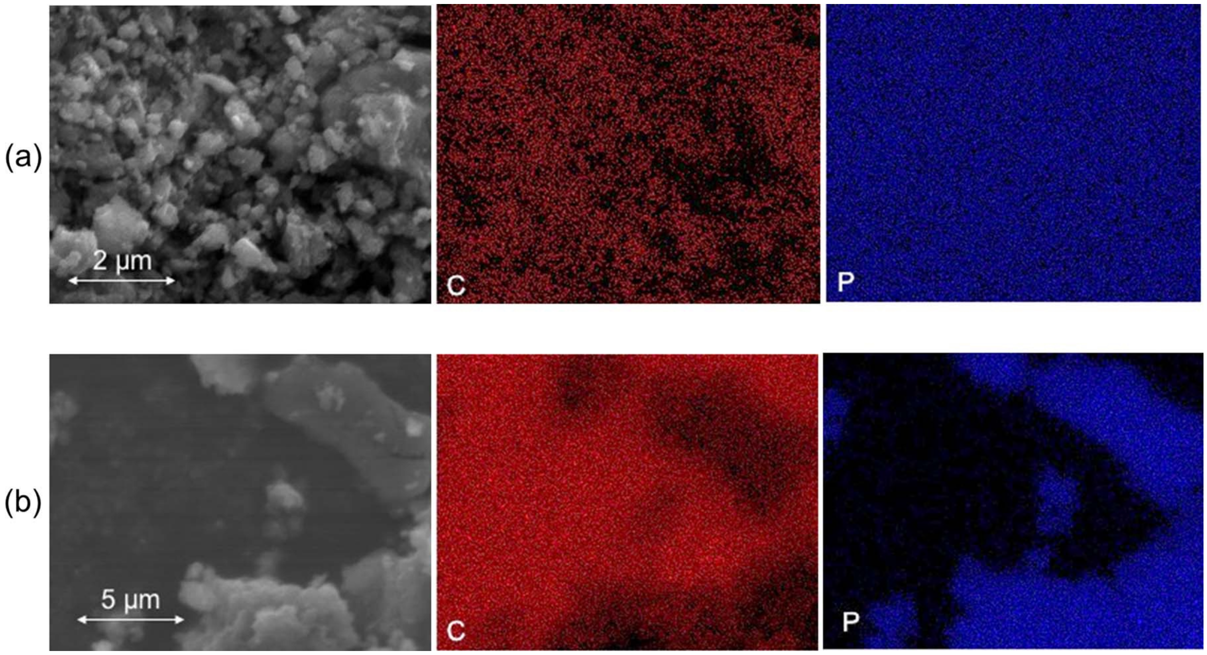

Figure S 7. SEM images of BP-G and the corresponding EDAX mapping of carbon (red) and phosphorus (blue): (a) BP-G form and (b)BP/G form co-exist in BP-G composite.

The change from BP/G to BP-G form was also supported by the observed XRD patterns. As shown in Figure S 8, the XRD pattern of the BP/G mixture shows discrete diffraction peaks related to both BP and graphite. After 6 h of ball milling, the two main diffraction peaks ([002] and [004]) corresponding to graphite almost disappeared, and the three main peaks related to BP ([020], [021], and [111], JCPDS 01-073-1358) significantly diminished. After 12 h of ball milling, the diffraction peaks associated with BP completely disappeared, leaving only an asymmetrical, broadened peak near 25°. This is not simply due to the particle amorphization induced by the milling process but also the formation of new BP-G composites with amorphous phase and P-C bonds. As reported in our previous work [101], BP remains its crystalline phase and related intensities are not reduced during ball milling, unlike what is observed in graphite [105]. During ball milling, the graphite crystalline structure changes to an amorphous structure, wherein [002] and [100] peaks are greatly diminished and broadened [105, 106]. If no chemical bonds between phosphorus and carbon were formed in BP-G particles, clear BP-related peaks would have presented in the BP-G samples, similar as the BP/G mixture sample. As suggested by previous studies, some P-P bonds in BP were bro- ken down to form new P-C bonds in the BP-G composite [29, 31]. The formation of P-C bonds in $BP_{0.3}G_1$ is further supported by the appearance of a new peak near 43° (marked with diamond symbols) after ball milling. This new peak could be a unique feature of $BP_{0.3}G_1$ structure suggesting a new P-C bond. Notably, $BP_{0.9}G_1$ exhibited a different XRD pattern that did not contain the new peak observed in $BP_{0.3}G_1$. This indicates that different types of P-C bonds are formed in BP-G composites depending on their composition, as suggested by previous theoretical studies [31, 32].

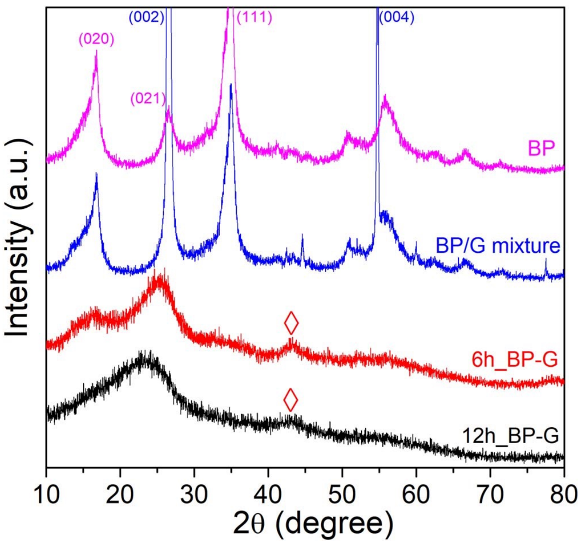

Figure S 8. XRD patterns of BP, BP/G mixture, 6h-HEMM $BP_{0.3}G_1$, and 12h-HEMM $BP_{0.3}G_1$

Although increases in ball milling time improved initial reversible capacity and first cycle coulombic efficiency of $BP_{0.3}G_1$, it did not improve the cycle performance (Figure S 6). The remaining capacity of the $BP_{0.3}G_1$ ball-milled for 24 h was only 934 mAh/g$_{\_BP}$ (407 mAh/g$_{\_BP+G}$) at the end of 50 cycles, slightly higher than the other samples. This suggests that improved links between phosphorus and carbon (i.e., a complete transformation of BP/G to BP-G form) can increase initial reversible capacity and first cycle coulombic efficiency of BP-G, but not cycle performance. For comparison, the capacity (220 mAh/g) of the 6h-HEMM graphite (reference cell) is also shown, demonstrating that BP-G particles did contribute to total cell capacity.

Appendix 4. Effects of Modifications to Ball Milling Process on Cyclability

Two different synthetic approaches were employed to reduce the size of BP-G particles while maintaining the strong bonds between phosphorus and carbon. The first approach was to apply an additional wet ball milling step after BP-G synthesis using a dual asymmetric centrifuge-type mixer to overcome the intrinsic limitations of a shaker/mixer mill. Although a shaker/mixer mill can be beneficial in producing BP materials with greater crystallinity than a planetary-type mill, it does not effectively reduce particle size nor produce homogeneous particles.

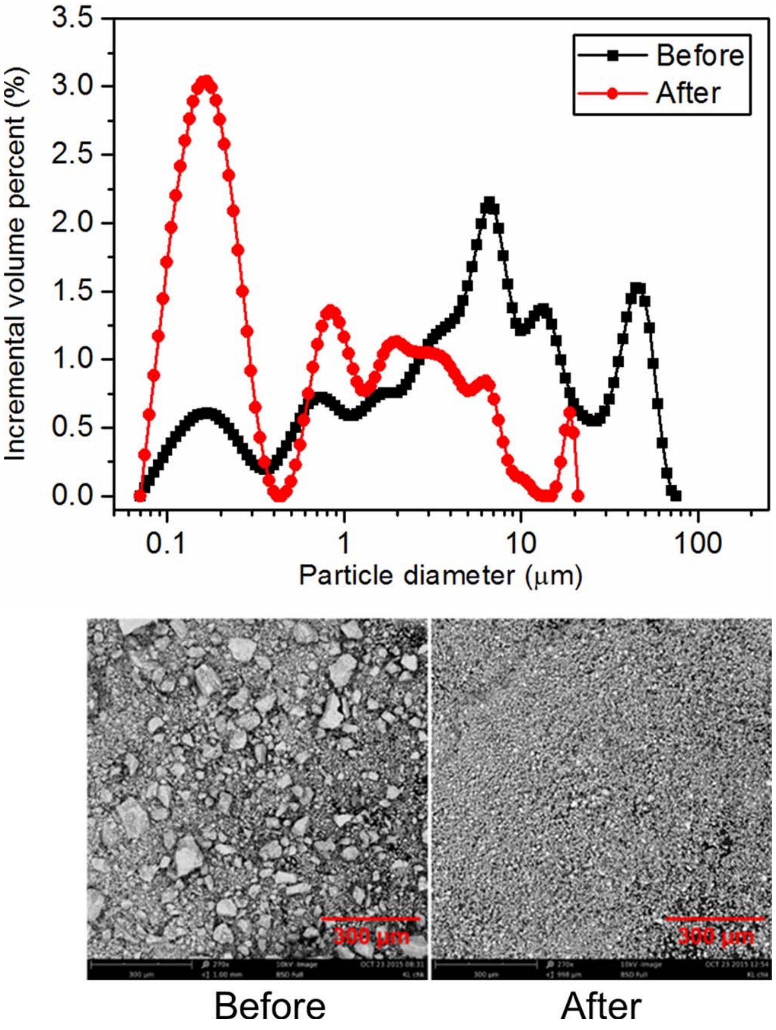

Figure S 9. Change in particle size distributions after additional wet ball milling

As shown in Figure S 9, the additional wet ball milling process increased the homogeneity of BP particle size by reducing the particle size. The mean particle size of BP (11.8 μm, $d_{50} = 5.7$ μm) was significantly reduced to 0.8 μm ($d_{50} = 2.1$ μm) after the wet ball milling process. Large BP particles virtually disappeared, and considerable numbers of nano and submicron-sized particles were generated. Despite the reduction in particle size, however, the cycle performance of $BP_{0.3}G_1$ improved only slightly, and rather the initial reversible capacity worsened (Figure S 10). The $BP_{0.3}G_1$ processed by 6h-HEMM combined with wet ball milling showed a gradual decrease in reversible capacity (903 mAh/g, after the first cycle) to 568 mAh/g at the end of the 50th cycle. This capacity loss (37.1% drop) was slightly better than that (39.2%) observed for $BP_{0.3}G_1$ synthesized without the additional wet ball milling. However, the reversible capacity of $BP_{0.3}G_1$ was reduced, and the first cycle coulombic efficiency dropped slightly (70% vs. 66%). This is probably due to the poor electrolyte impregnation in a dense electrode with a high active material loading. The nano and submicron-sized BP-G particles produced by wet ball milling likely lead to a reduction in porosity and an increase in active material loading of the electrode. This strongly affects electrolyte transport into the pore networks of the electrode active material, with concomitant effects on the electrode wetting rate. Indeed, it was observed that the active material loading of $BP_{0.3}\,G_1$ electrode greatly increased after wet ball milling to 5.4 mg/cm^2 from 3.9 mg/cm^2, indicating that the lower reversible capacity of $BP_{0.3}G_1$ was a consequence of the denser electrode. The greater surface areas of nano and submicron-sized BP-G particles also contribute to slower electrolyte wetting.

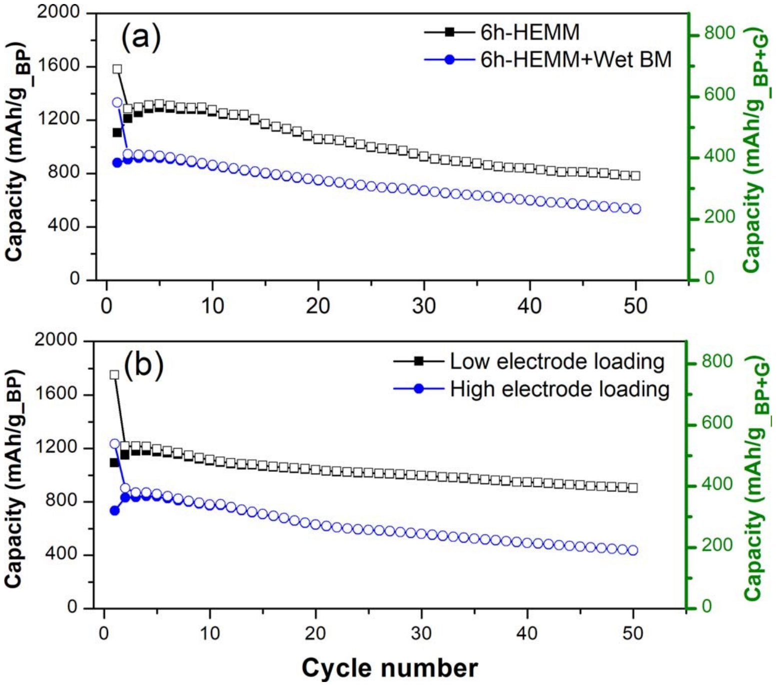

Figure S 10. (a) Cycle performance of 6h-HEMM $BP_{0.3}G_1$ (black square) vs. 6h-HEMM followed by wet ball milling processed $BP_{0.3}G_1$ (blue circle); (b) cycle performance of 12h-HEMM $BP_{0.3}G_1$ with a high (5.0 mg/cm^2, blue, circle) and low (1.9 mg/cm^2, black, square) active material (BP+G) loading. Cells were cycled without FEC additive between 2.0 – 0.01 V (vs. Li^+/Li) with a current density of 200 mA/g. Open and closed symbols represent discharge (lithiation) and charge (delithiation) capacities, respectively. The specific capacity is displayed based on either BP weight (left axis, black) or BP + G weight (right axis, green).

We set out to confirm these speculations by exploring the effect of active material loading on the electrochemical performance of $BP_{0.3}G_1$ in further depth. $BP_{0.3}G_1$ electrodes with different active material loadings were prepared with varying thicknesses of electrodes. As shown in Figure S 10, active material loading had a significant influence on reversible capacity and cyclability. The electrode with low active material loading (1.9 mg/cm^2) showed higher reversible capacity (1217 mAh/g after the first cycle) and significantly better cycle performance (capacity loss of 25%) than those of the electrode with high active material loading (5.0 mg/cm^2). This result confirms that decreases in reversible capacity and capacity retention of $BP_{0.3}G_1$ after wet ball milling were mainly caused by increased active material loading in the electrode. Notably, the cycle performance observed for high loading (capacity loss of 52%) was significantly improved by low active material loading (capacity loss of 25%), indicating that active material loading parameters exert a stronger effect on the cyclability of BP-G than other factors such as FEC additive or ball milling time.

Appendix 5. Additional Material and Cycling Characterizations in Chapter 4

For BPG_BM sample, the composition condition is actually not in a particle-by-particle manner. Instead, phosphorus and carbon are mixed and connected at nanoscale/atomic as the Figure S 11 shown. Which is the foundation of obtaining hybrid phosphorene-graphene in Figure 4.4.

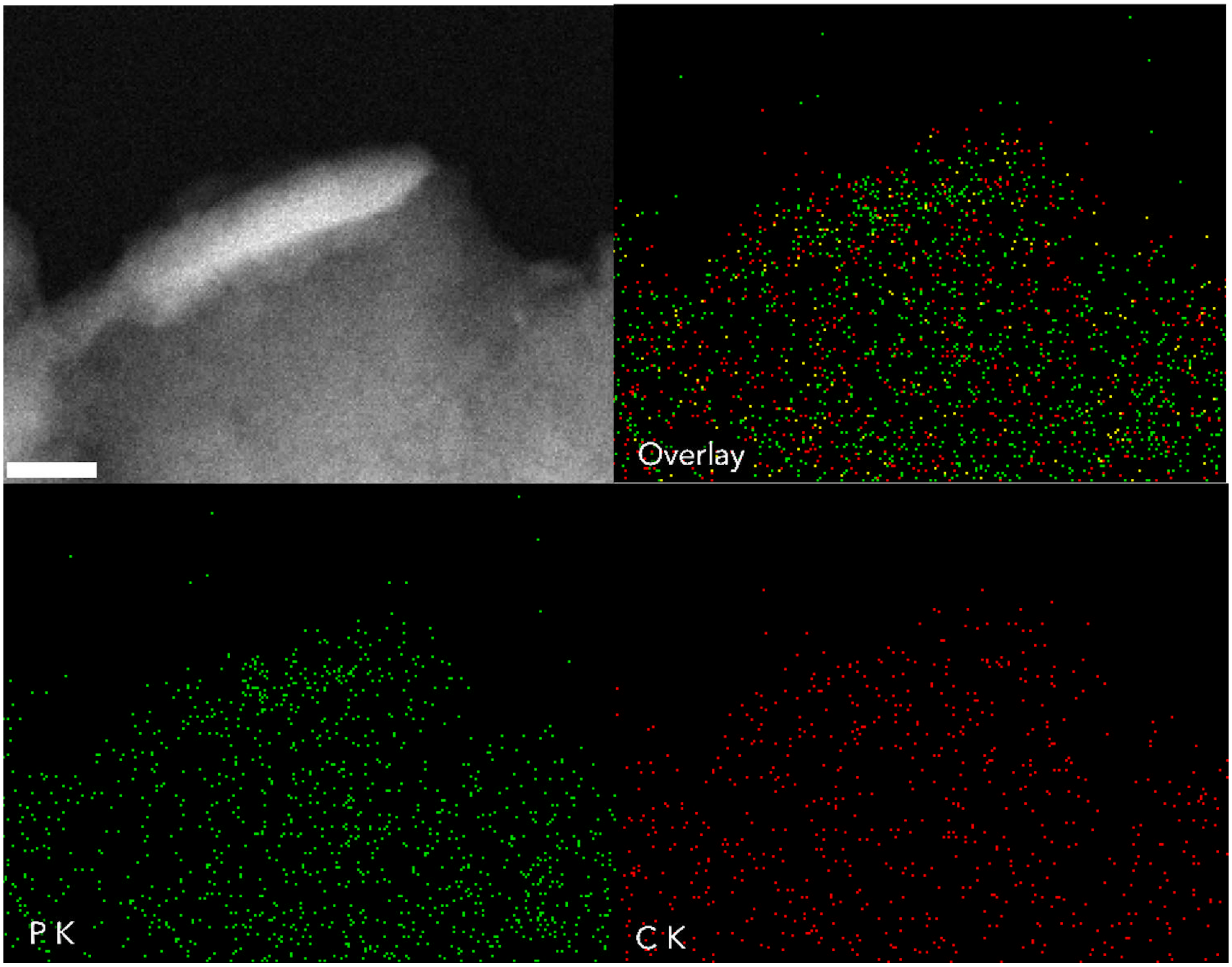

Figure S 11. Dark field STEM image of BPG_BM sample with the corresponding EDAX elemental mapping, scale bar = 20 nm

The cycling profile at 4 A/g (Figure S 12(a)) and 6 A/g (Figure S 12(b)) are similar to Figure 4.10(c), indicating that BPG_soni is not sensitive to current density. It is always able to deliver stable capacity over long term cycling. But when current density is very high at 6 A/g, initially there will be more fluctuation. Fortunately, the battery system become stable soon. The following trend is constant with relatively low current density samples.

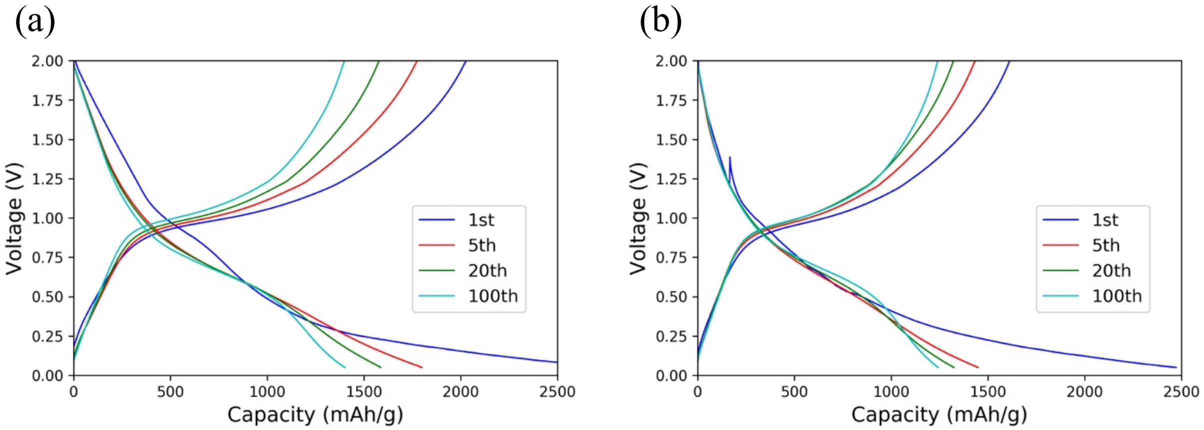

Figure S 12. charge-discharge curves of BPG_soni at (a) 4 A/g, (b) 6 A/g

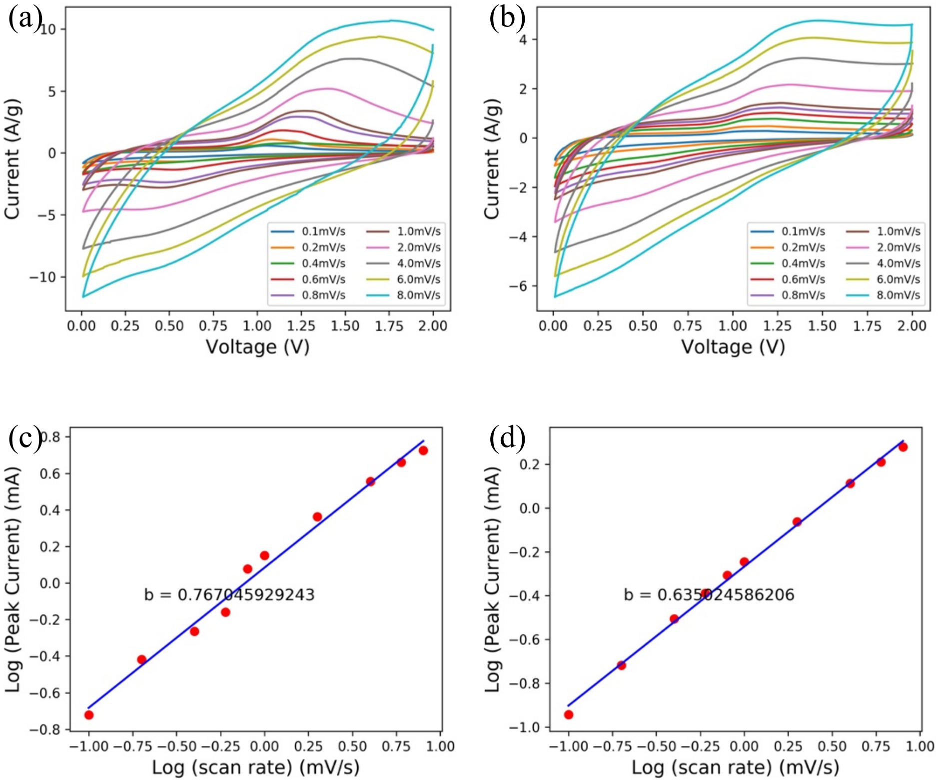

Figure S 13. CV profile scanned at rates from 0.1 to 8.0 mV/s: (a) BPG_soni, (b) BPG_BM; log(v)-log(i): (c) BPG_soni; (d) BPG_BM

Using increasing scanning rate to separate the capacitive effect from total capacity, the CV profiles of BPG_BM and BPG_soni are shown in Figure S 13(a)(b). Apparently, higher scanning rate produce higher peak current in the anodic and cathodic cycles. The positions of peak current shift, showing higher overpotential. Regressing peak current against scan rate, the coefficient can qualitatively describe the degree of capacitive contribution according to Equation (*4.2*). The coefficient closer to 1.0, the more capacitor influence. The comparison in Figure S 13(c)(d) clearly shows stronger capacitive effect in BPG_soni.

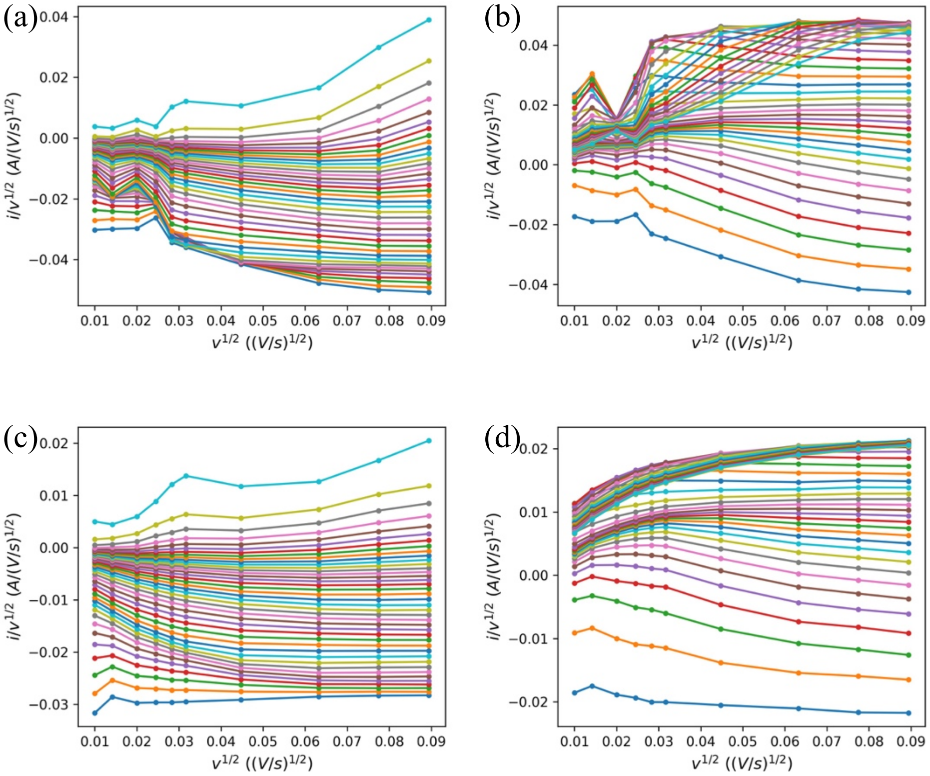

Figure S 14. $v^{1/2}$-$i/v^{1/2}$ plot at different potentials 0.01-2.0 V for (a) BPG_soni anodic; (b) BPG_soni cathodic; (c) BPG_BM anodic; (d) BPG_BM cathodic.

To quantify the proportion of capacitive contribution, the discretized curves in Figure S 14 at each voltage stages are used to fit the coefficients k_1 and k_2 in Equation (*4.4*). Inversely, the decomposed capacitive capacity is shown in Figure S 15, where the green region is fitted capacitive part. The outside void part is diffusion-controlled capacity storage. Integrating the area of green region and dividing by total area, the final proportion of capacitive capacity at different CV scanning rate is summarized in Figure 4.14.

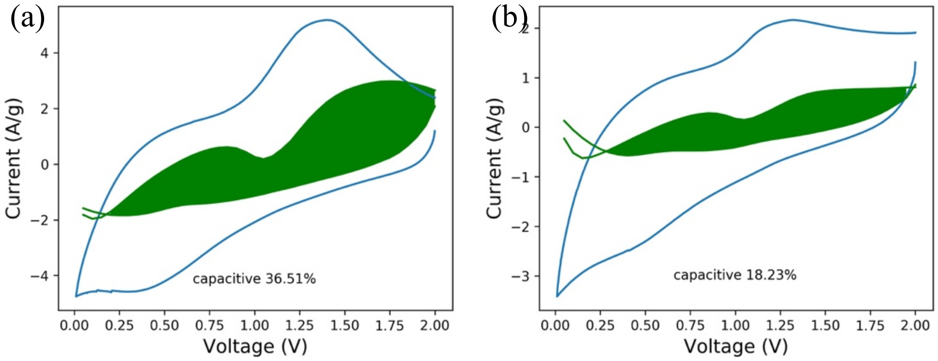

Figure S 15. Example of capacitive contribution at 2.0 mV/s for (a) BPG_soni; (b) BPG_BM.

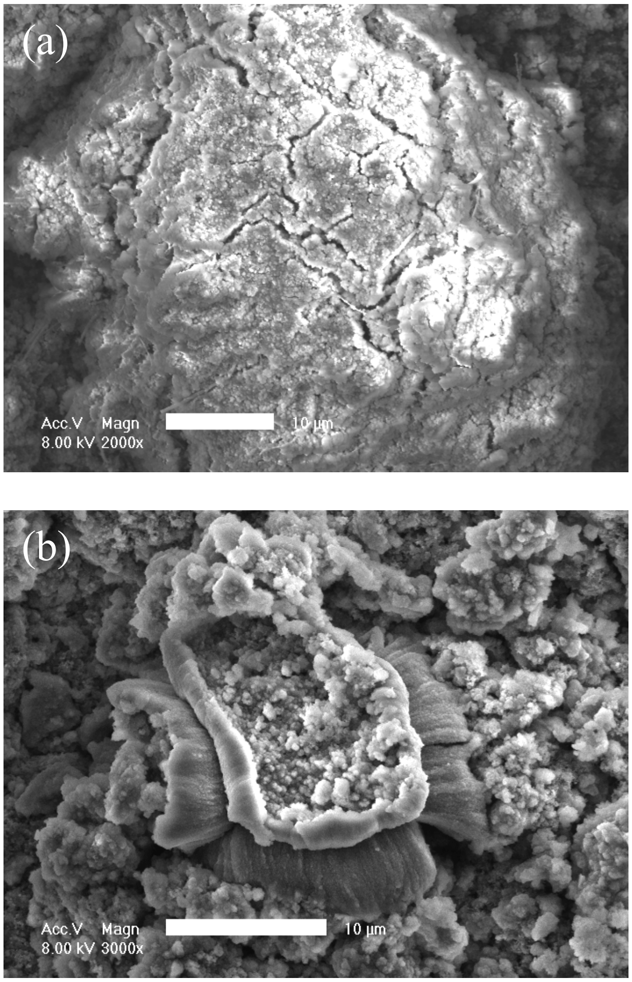

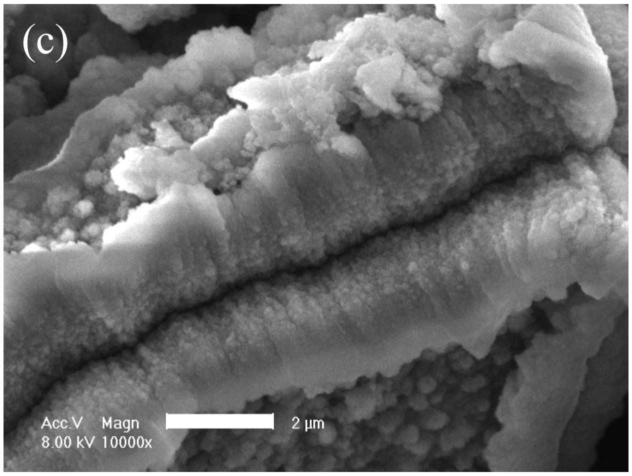

Figure S 16. (a) zoom-in SEM images of surface pulverization in BPG_BM (scale bar = 10 μm), (b)(c) more secondary particle cracks in BPG_BM (scale bar = 2 μm).

Cycled BPG_BM is full of cracks and fractures in Figure S 16. Moreover, the zoom-in cracks pattern in Figure S 16 (b)(c) shows that the agglomerated secondary particles cannot sustain the local tensile stress during delithiation. Therefore, control the primary particle size is not critical. The size and morphology of agglomerated secondary particle should have higher priority to be optimized. On the other hand, the cycled BPG_soni samples still have smooth surface with a little crack in Figure S 17 (a)(b). And crack perpendicularly penetrates until the current collector in Figure S 17 (c). So it doesn't damage electronic connection significantly with trivial influence on capacity.

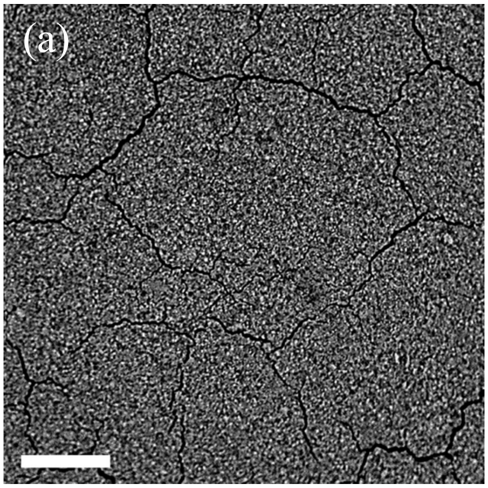

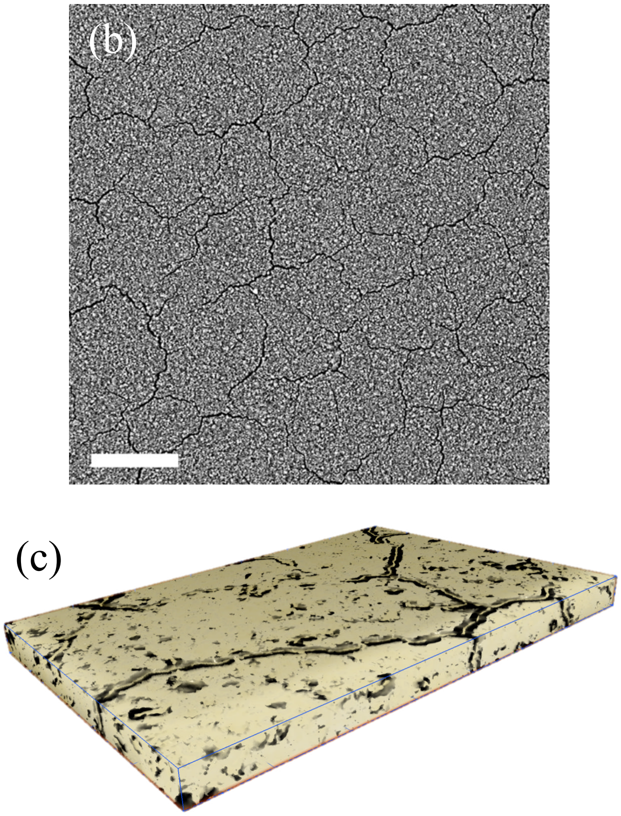

Figure S 17. SEM images of BPG_soni electrode surface after 100 cycles at (a) 4 A/g, (b) 6 A/g (scale bar = 50 μm). (c) 3D representation of highlighted line crack patterns.

Processing the Micro-CT data to filter out the pore volume inside the cycled electrode, BPG_BM is full of pores shown in Figure S 18(a). It implies that many particles or material blocks don’t contact with each other any more. The sparse and isolated pore region in Figure S 18(b) shows the structural continuity and robustness of BPG_soni.

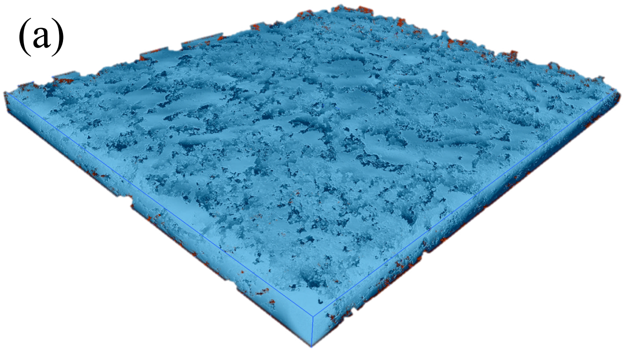

(a)

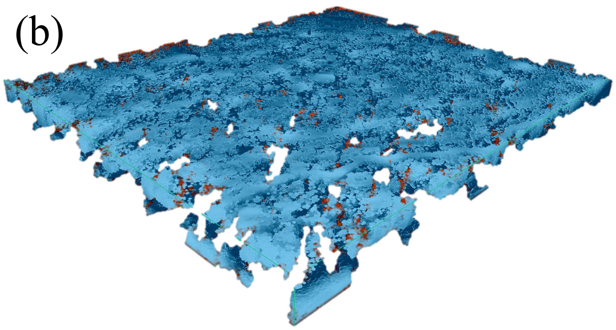

(b)

Figure S 18. Grayscale segmented continuous pore region for (a) BPG_BM electrode at 2 A/g after 100 cycles, (b) BPG_soni electrode at 2 A/g after 100 cycles.

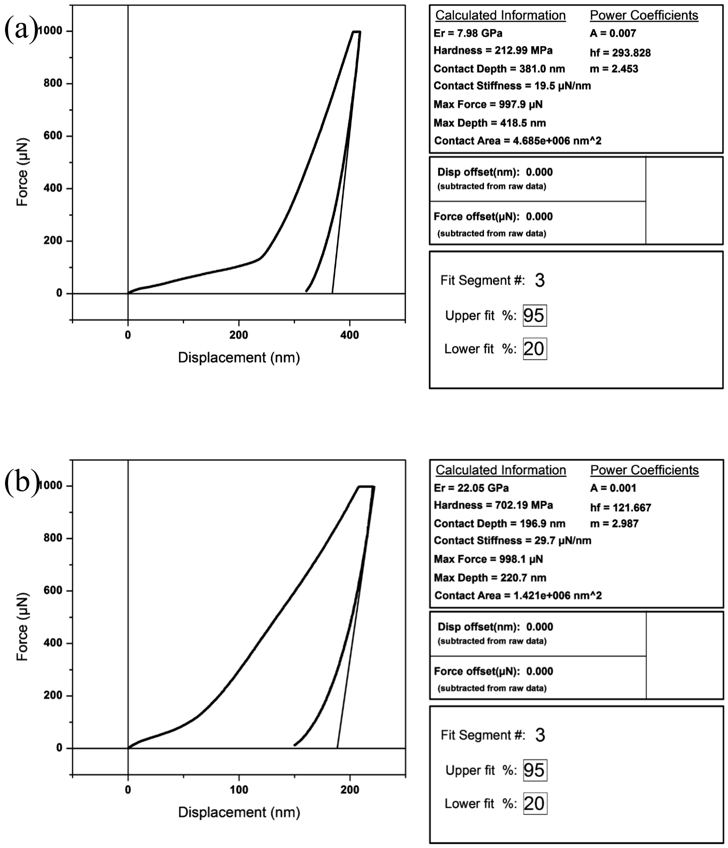

(a)

Calculated Information
Er = 7.98 GPa
Hardness = 212.99 MPa
Contact Depth = 381.0 nm
Contact Stiffness = 19.5 μN/nm
Max Force = 997.9 μN
Max Depth = 418.5 nm
Contact Area = 4.685e+006 nm^2

Power Coefficients
A = 0.007
hf = 293.828
m = 2.453

Disp offset(nm): 0.000
(subtracted from raw data)

Force offset(μN): 0.000
(subtracted from raw data)

Fit Segment #: 3
Upper fit %: 95
Lower fit %: 20

(b)

Calculated Information
Er = 22.05 GPa
Hardness = 702.19 MPa
Contact Depth = 196.9 nm
Contact Stiffness = 29.7 μN/nm
Max Force = 998.1 μN
Max Depth = 220.7 nm
Contact Area = 1.421e+006 nm^2

Power Coefficients
A = 0.001
hf = 121.667
m = 2.987

Disp offset(nm): 0.000
(subtracted from raw data)

Force offset(μN): 0.000
(subtracted from raw data)

Fit Segment #: 3
Upper fit %: 95
Lower fit %: 20

Figure S 19. Representative loading-displacement curves and mechanical analysis results of (a) BPG_BM electrode at 2 A/g after 100 cycles, (b) BPG_soni electrode at 2 A/g after 100 cycles.

Appendix 6. Additional Material Characterizations for BP-based LIB in Chapter. 5

The 16 groups are sorted by electrode thickness shown in Figure S 20. It can be seen that side views of each group are similar due to the same ratio of active material, carbon black, PvdF binder. The cutting process may slightly damage the cross-sectional view. But it won't influence the thickness measurement at all.

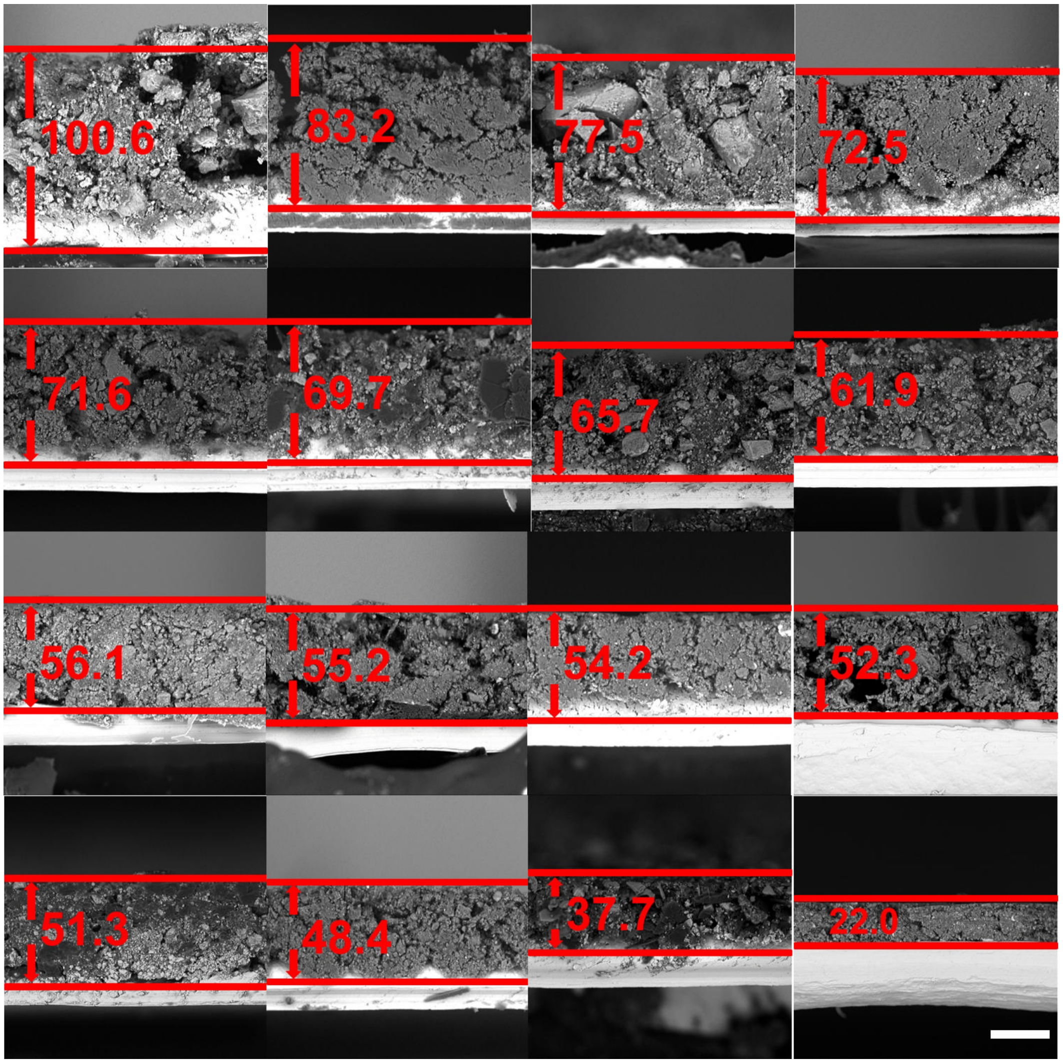

Figure S 20. Cross-sectional view and thickness of group 1~16 electrodes (scale bar = 20 μm)

Using difference in brightness of phosphorus particles and graphite/carbon black to identify phosphorus particles is a common image processing method. The marked regions in Figure S 21 are extracted phosphorus. Then the mean lateral size is computed by averaging all particles in the view. The so-called size measured here is attributed to secondary, due to primary BP particles are very small and close to connect to each other.

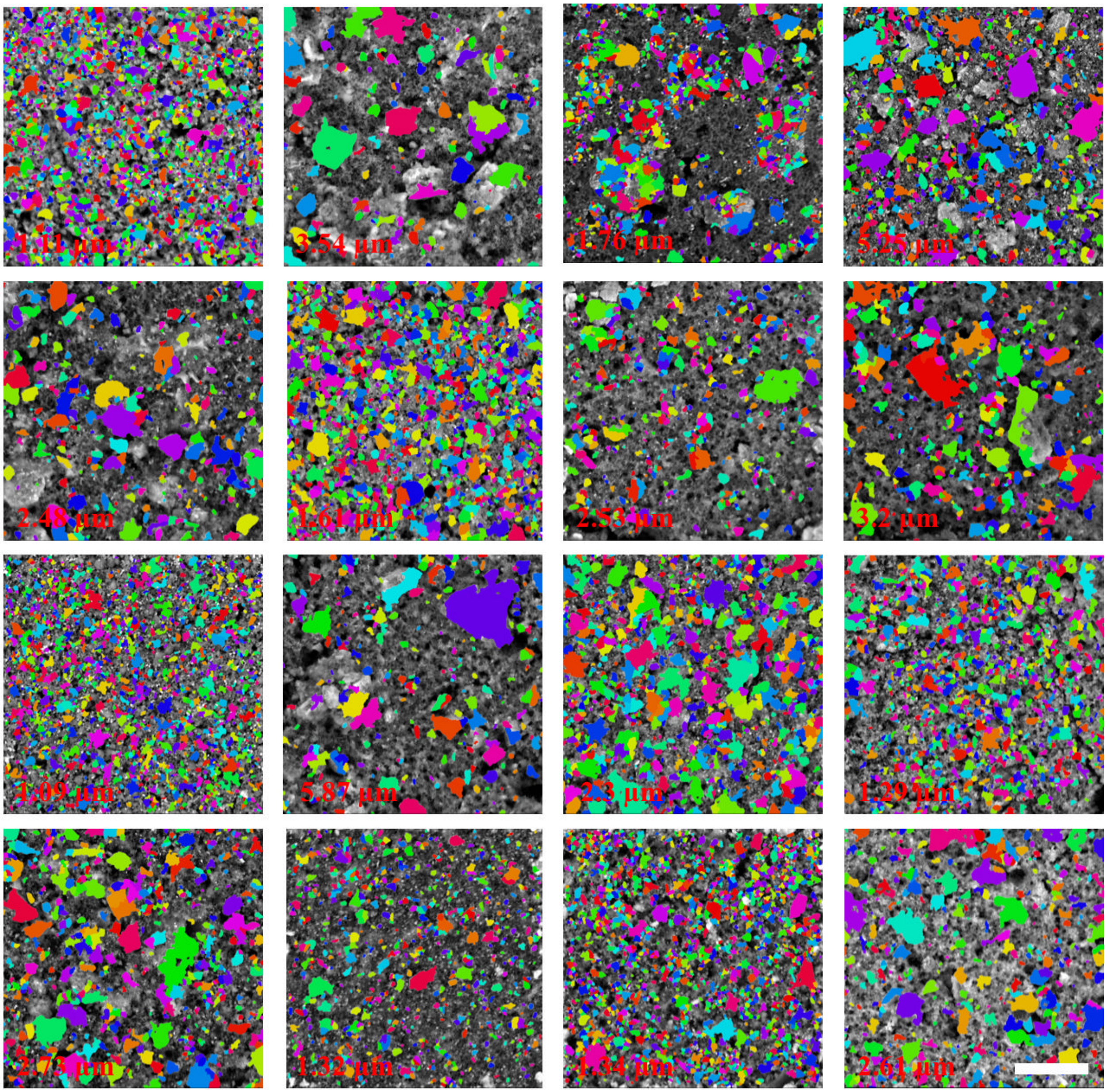

Figure S 21. Particle size extraction of group 1~16 electrodes (scale bar = 10 µm, the inserted value is average particle size)

The 3D height profile of electrode surface can be reconstructed from four perpendicular perspectives in SEM. Then average roughness is calculated by five lines drawn on the surface. Without losing generality, the five lines are always distributed from southwest the northeast on the plane. The process is repeated three times to ensure results not be biased to local point. The rough surface often come from large agglomerated particles, shown by the red peak-like structure. So, the roughness value can also be used to infer the existence of large secondary particles.

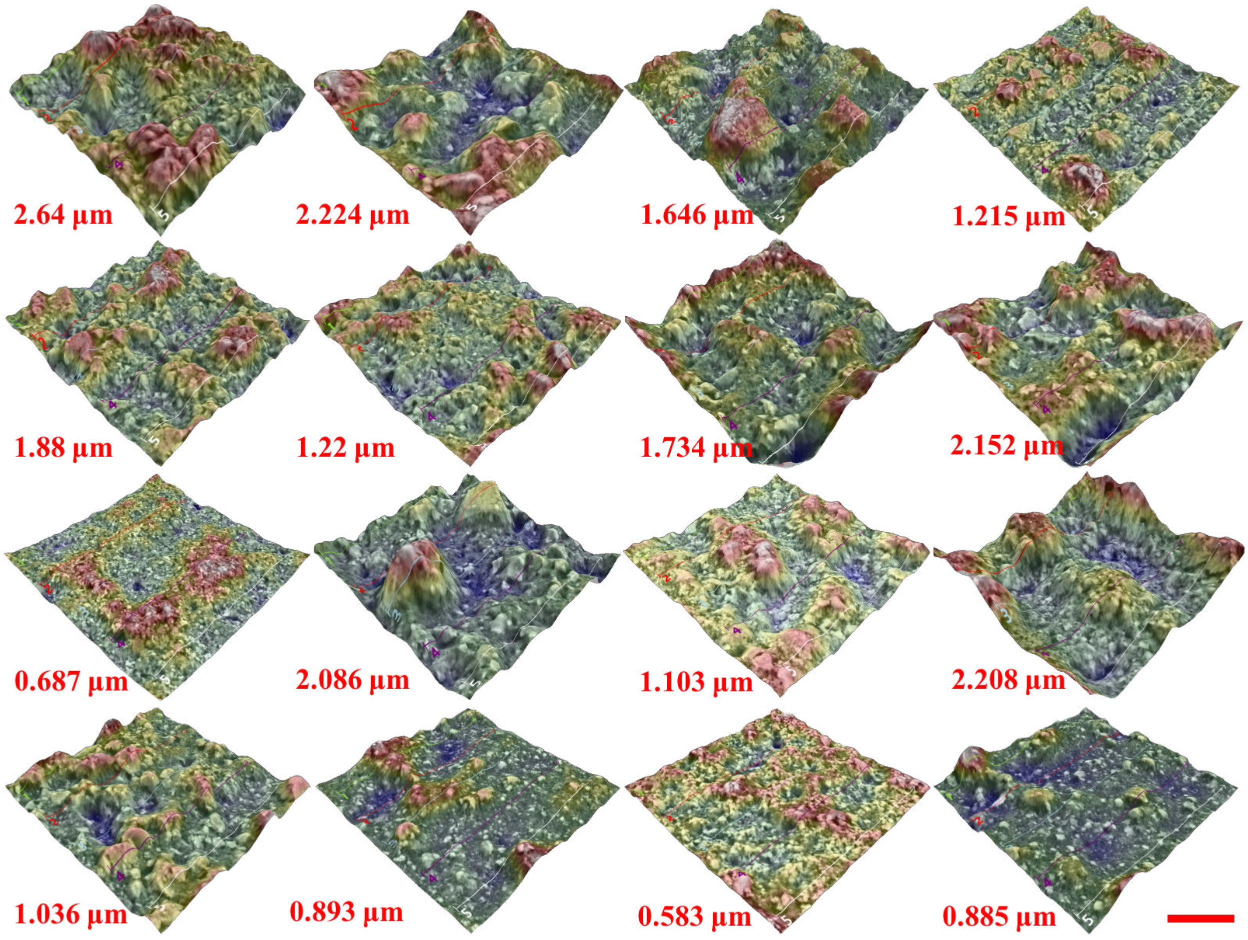

Figure S 22. Surface roughness of group 1~16 electrodes (scale bar = 10, scale bar = 10 μm, the inserted value is average roughness)

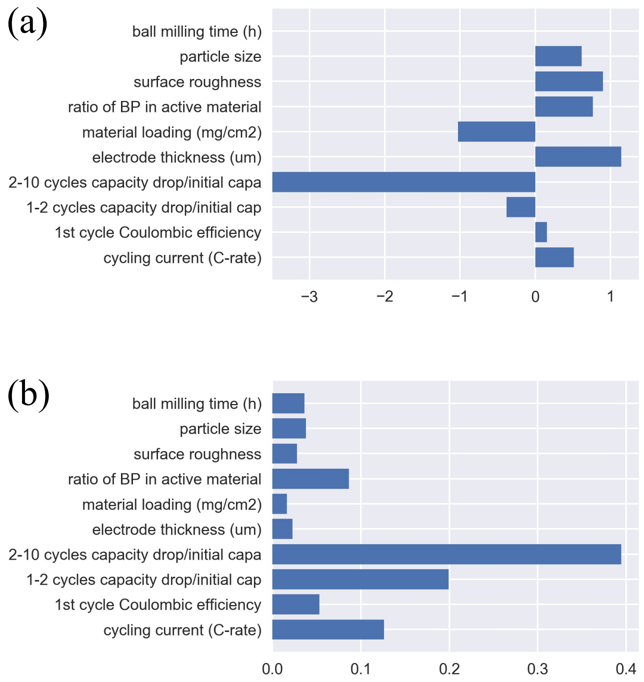

Figure S 23. Coefficients fitted from the (a) logistic regression on l1 penalty (LASSO) and (b)Random Forest with 2nd-to-10th cycle capacity drop ratio

After adding the 2nd-to-10th cycle capacity drop ratio into the machine learning models, it will dominate and cover up all other variables. It leaks too much information about degradation or even directly means the battery already fails. It must be removed from the original feature space to make model and interpretation meaningful.

Bibliography

1. Yoshio, M., R.J. Brodd, and A. Kozawa, *Lithium-ion batteries*. Vol. 1. 2009: Springer.
2. Zheng, H., et al., *Hard carbon: a promising lithium-ion battery anode for high temperature applications with ionic electrolyte.* RSC Advances, 2012. **2**(11): p. 4904-4912.
3. De las Casas, C. and W. Li, *A review of application of carbon nanotubes for lithium ion battery anode material.* Journal of Power Sources, 2012. **208**: p. 74-85.
4. Yang, S., H. Song, and X. Chen, *Electrochemical performance of expanded mesocarbon microbeads as anode material for lithium-ion batteries.* Electrochemistry communications, 2006. **8**(1): p. 137-142.
5. Yu, S.H., et al., *Conversion reaction -based oxide nanomaterials for lithium ion battery anodes.* Small, 2016. **12**(16): p. 2146-2172.
6. McDowell, M.T., et al., *25th anniversary article: understanding the lithiation of silicon and other alloying anodes for lithium -ion batteries.* Advanced Materials, 2013. **25**(36): p. 4966-4985.
7. Bridgman, P., *TWO NEW MODIFICATIONS OF PHOSPHORUS.* Journal of the American Chemical Society, 1914. **36**(7): p. 1344-1363.
8. Shirotani, I., *Growth of large single crystals of black phosphorus at high pressures and temperatures, and its electrical properties.* Molecular Crystals and Liquid Crystals, 1982. **86**(1): p. 203-211.
9. Lange, S., P. Schmidt, and T. Nilges, *Au3SnP7@ black phosphorus: an easy access to black phosphorus.* Inorganic chemistry, 2007. **46**(10): p. 4028-4035.
10. Sun, H., et al., *First-principles study of thermal expansion and thermomechanics of single-layer black and blue phosphorus.* Physics Letters A, 2016. **380**(24): p. 2098-2104.
11. Li, W., et al., *Ultrafast and directional diffusion of lithium in phosphorene for high-performance lithium-ion battery.* Nano letters, 2015. **15**(3): p. 1691-1697.
12. Luo, Z., et al., *Anisotropic in-plane thermal conductivity observed in few-layer black phosphorus.* Nature communications, 2015. **6**: p. 8572.
13. Qiao, J., et al., *High-mobility transport anisotropy and linear dichroism in few-layer black phosphorus.* Nature communications, 2014. **5**: p. 4475.
14. Xia, F., et al., *Two-dimensional material nanophotonics.* Nature Photonics, 2014. **8**(12): p. 899.
15. Ling, X., et al., *The renaissance of black phosphorus.* Proceedings of the National Academy of Sciences, 2015. **112**(15): p. 4523-4530.
16. Fu, Y.Q., et al., *Advanced Phosphorus-Based Materials for Lithium/Sodium-Ion Batteries: Recent Developments and Future Perspectives.* Advanced Energy Materials, 2018. **8**(13): p. 28.
17. Mayo, M., et al., *Ab initio study of phosphorus anodes for lithium-and sodium-ion batteries.* Chemistry of Materials, 2016. **28**(7): p. 2011-2021.
18. Ramireddy, T., et al., *Phosphorus-carbon nanocomposite anodes for lithium-ion and sodium-ion batteries.* Journal of Materials Chemistry A, 2015. **3**(10): p. 5572-5584.

19. Park, C.M. and H.J. Sohn, *Black phosphorus and its composite for lithium rechargeable batteries.* Advanced Materials, 2007. **19**(18): p. 2465-+.
20. Sun, J., et al., *Formation of stable phosphorus–carbon bond for enhanced performance in black phosphorus nanoparticle–graphite composite battery anodes.* Nano letters, 2014. **14**(8): p. 4573-4580.
21. Xu, F., et al., *Scalable shear-exfoliation of high-quality phosphorene nanoflakes with reliable electrochemical cycleability in nano batteries.* 2d Materials, 2016. **3**(2): p. 12.
22. Sun, L.Q., et al., *Electrochemical Activity of Black Phosphorus as an Anode Material for Lithium-Ion Batteries.* Journal of Physical Chemistry C, 2012. **116**(28): p. 14772-14779.
23. Sun, J., et al., *Formation of Stable Phosphorus-Carbon Bond for Enhanced Performance in Black Phosphorus Nanoparticle-Graphite Composite Battery Anodes.* Nano Letters, 2014. **14**(8): p. 4573-4580.
24. Qian, J.F., et al., *Reversible 3-Li storage reactions of amorphous phosphorus as high capacity and cycling-stable anodes for Li-ion batteries.* Chemical Communications, 2012. **48**(71): p. 8931-8933.
25. Stan, M.C., et al., *Puzzling out the origin of the electrochemical activity of black P as a negative electrode material for lithium-ion batteries.* Journal of Materials Chemistry A, 2013. **1**(17): p. 5293-5300.
26. Nagao, M., A. Hayashi, and M. Tatsumisago, *All-solid-state lithium secondary batteries with high capacity using black phosphorus negative electrode.* Journal of Power Sources, 2011. **196**(16): p. 6902-6905.
27. Liu, H., et al., *Semiconducting black phosphorus: synthesis, transport properties and electronic applications.* Chemical Society Reviews, 2015. **44**(9): p. 2732-2743.
28. Hardwick, L.J., et al., *An investigation of the effect of graphite degradation on irreversible capacity in lithium-ion cells.* Journal of The Electrochemical Society, 2008. **155**(6): p. A442-A447.
29. Claeyssens, F., et al., *Phosphorus carbides: theory and experiment.* Dalton Transactions, 2004(19): p. 3085-3092.
30. Kim, Y., et al., *An Amorphous Red Phosphorus/Carbon Composite as a Promising Anode Material for Sodium Ion Batteries.* Advanced Materials, 2013. **25**(22): p. 3045-3049.
31. Claeyssens, F., et al., *Solid phases of phosphorus carbide: An ab initio study.* Physical Review B, 2009. **79**(13): p. 134115.
32. Hart, J.N., N.L. Allan, and F. Claeyssens, *Predicting crystal structures ab initio: group 14 nitrides and phosphides.* Physical Chemistry Chemical Physics, 2010. **12**(30): p. 8620-8631.
33. Mauger, A. and C. Julien, *Nanoscience supporting the research on the negative electrodes of Li-ion batteries.* Nanomaterials, 2015. **5**(4): p. 2279-2301.
34. Xia, W., et al., *Visualizing the electrochemical lithiation/delithiation behaviors of black phosphorus by in situ transmission electron microscopy.* The Journal of Physical Chemistry C, 2016. **120**(11): p. 5861-5868.
35. Han, X., et al., *Carbon-coated Si micrometer particles binding to reduced graphene oxide for a stable high-capacity lithium-ion battery anode.* Journal of Materials Chemistry A, 2016. **4**(45): p. 17757-17763.
36. Xu, F., et al., *In situ TEM visualization of superior nanomechanical flexibility of shear-exfoliated phosphorene.* Nanoscale, 2016. **8**(28): p. 13603-13610.

37. Sun, J., et al., *A phosphorene-graphene hybrid material as a high-capacity anode for sodium-ion batteries.* Nature Nanotechnology, 2015. **10**(11): p. 980-U184.
38. Qiu, M., et al., *Current progress in black phosphorus materials and their applications in electrochemical energy storage.* Nanoscale, 2017. **9**(36): p. 13384-13403.
39. Dhanabalan, S.C., et al., *Emerging Trends in Phosphorene Fabrication towards Next Generation Devices.* Advanced Science, 2017. **4**(6): p. 32.
40. Li, W., et al., *Shape and size controlled synthesis of uniform iron oxide nanocrystals through new non-hydrolytic routes.* Nanotechnology, 2016. **27**(32): p. 324002.
41. Walia, S., et al., *Defining the role of humidity in the ambient degradation of few-layer black phosphorus.* 2d Materials, 2017. **4**(1): p. 8.
42. Wang, G.X., et al., *Degradation of phosphorene in air: understanding at atomic level.* 2d Materials, 2016. **3**(2): p. 7.
43. Island, J.O., et al., *Environmental instability of few-layer black phosphorus.* 2d Materials, 2015. **2**(1): p. 6.
44. Avsar, A., et al., *Air-Stable Transport in Graphene-Contacted, Fully Encapsulated Ultrathin Black Phosphorus-Based Field-Effect Transistors.* Acs Nano, 2015. **9**(4): p. 4138-4145.
45. Kim, J.S., et al., *Toward air-stable multilayer phosphorene thin-films and transistors.* Scientific Reports, 2015. **5**: p. 7.
46. Xing, C.Y., et al., *Graphene oxide/black phosphorus nanoflake aerogels with robust thermo-stability and significantly enhanced photothermal properties in air.* Nanoscale, 2017. **9**(24): p. 8096-8101.
47. Tang, X., et al., *Fluorinated Phosphorene: Electrochemical Synthesis, Atomistic Fluorination, and Enhanced Stability.* Small, 2017. **13**(47): p. 10.
48. Guo, Z.N., et al., *Metal-Ion-Modified Black Phosphorus with Enhanced Stability and Transistor Performance.* Advanced Materials, 2017. **29**(42): p. 8.
49. Luo, W., et al., *Surface chemistry of black phosphorus under a controlled oxidative environment.* Nanotechnology, 2016. **27**(43): p. 10.
50. Guo, Z.N., et al., *From Black Phosphorus to Phosphorene: Basic Solvent Exfoliation, Evolution of Raman Scattering, and Applications to Ultrafast Photonics.* Advanced Functional Materials, 2015. **25**(45): p. 6996-7002.
51. Hanlon, D., et al., *Liquid exfoliation of solvent-stabilized few-layer black phosphorus for applications beyond electronics.* Nature Communications, 2015. **6**: p. 11.
52. Diouf, B. and R. Pode, *Potential of lithium-ion batteries in renewable energy.* Renewable Energy, 2015. **76**: p. 375-380.
53. Guo, Z., et al., *From black phosphorus to phosphorene: basic solvent exfoliation, evolution of Raman scattering, and applications to ultrafast photonics.* Advanced Functional Materials, 2015. **25**(45): p. 6996-7002.
54. Zhang, J., H. Shin, and W. Lu, *Highly ambient stable few-layer black phosphorene by pulsed laser exfoliation and HEMM.* Chemical Communications, 2019.
55. Sun, J., et al., *A phosphorene–graphene hybrid material as a high-capacity anode for sodium-ion batteries.* Nature nanotechnology, 2015. **10**(11): p. 980.
56. Chen, L., et al., *Scalable Clean Exfoliation of High -Quality Few -Layer Black Phosphorus for a Flexible Lithium Ion Battery.* Advanced materials, 2016. **28**(3): p. 510-517.
57. Huang, Z., et al., *Layer -tunable phosphorene modulated by the cation insertion rate as a sodium -storage anode.* Advanced Materials, 2017. **29**(34): p. 1702372.

58. Zhang, Y., et al., *An Air-Stable Densely Packed Phosphorene–Graphene Composite Toward Advanced Lithium Storage Properties.* Advanced Energy Materials, 2016. **6**(12): p. 1600453.
59. Xu, G.-L., et al., *Nanostructured black phosphorus/Ketjenblack–multiwalled carbon nanotubes composite as high performance anode material for sodium-ion batteries.* Nano letters, 2016. **16**(6): p. 3955-3965.
60. Del Rio Castillo, A.E., et al., *Exfoliation of few-layer black phosphorus in low-boiling-point solvents and its application in Li-ion batteries.* Chemistry of Materials, 2018. **30**(2): p. 506-516.
61. Liu, H., et al., *Sandwiched Thin-Film Anode of Chemically Bonded Black Phosphorus/Graphene Hybrid for Lithium-Ion Battery.* Small, 2017. **13**(33): p. 1700758.
62. Shin, H., J. Zhang, and W. Lu, *Material structure and chemical bond effect on the electrochemical performance of black phosphorus-graphite composite anodes.* Electrochimica Acta, 2019.
63. Pan, L., et al., *Molecular level distribution of black phosphorus quantum dots on nitrogen-doped graphene nanosheets for superior lithium storage.* Nano Energy, 2016. **30**: p. 347-354.
64. Shuai, H., et al., *Electrochemically Exfoliated Phosphorene–Graphene Hybrid for Sodium-Ion Batteries.* Small Methods, 2019. **3**(2): p. 1800328.
65. Ciesielski, A. and P. Samorì, *Graphene via sonication assisted liquid-phase exfoliation.* Chemical Society Reviews, 2014. **43**(1): p. 381-398.
66. Guo, G.-C., et al., *Pristine and defect-containing phosphorene as promising anode materials for rechargeable Li batteries.* Journal of Materials Chemistry A, 2015. **3**(21): p. 11246-11252.
67. Sun, X. and Z. Wang, *Sodium adsorption and diffusion on monolayer black phosphorus with intrinsic defects.* Applied Surface Science, 2018. **427**: p. 189-197.
68. Song, J., et al., *Chemically bonded phosphorus/graphene hybrid as a high performance anode for sodium-ion batteries.* Nano letters, 2014. **14**(11): p. 6329-6335.
69. Park, C.M. and H.J. Sohn, *Black phosphorus and its composite for lithium rechargeable batteries.* Advanced materials, 2007. **19**(18): p. 2465-2468.
70. Favors, Z., et al., *Stable cycling of SiO 2 nanotubes as high-performance anodes for lithium-ion batteries.* Scientific reports, 2014. **4**: p. 4605.
71. Luo, Y., et al., *TiO2-Nanocoated Black Phosphorus Electrodes with Improved Electrochemical Performance.* ACS applied materials & interfaces, 2018. **10**(42): p. 36058-36066.
72. Kim, H.-W., et al., *Glucosamine-derived encapsulation of silicon nanoparticles for high-performance lithium ion batteries.* Journal of Materials Chemistry A, 2014. **2**(35): p. 14557-14562.
73. McDowell, M.T., S. Xia, and T. Zhu, *The mechanics of large-volume-change transformations in high-capacity battery materials.* Extreme Mechanics Letters, 2016. **9**: p. 480-494.
74. Vetter, J., et al., *Ageing mechanisms in lithium-ion batteries.* Journal of power sources, 2005. **147**(1-2): p. 269-281.
75. Qiu, M., et al., *Current progress in black phosphorus materials and their applications in electrochemical energy storage.* Nanoscale, 2017. **9**(36): p. 13384-13403.

76. Zhao, K., et al., *Fracture of electrodes in lithium-ion batteries caused by fast charging.* Journal of Applied Physics, 2010. **108**(7): p. 073517.
77. Oliver, W.C. and G.M. Pharr, *An improved technique for determining hardness and elastic modulus using load and displacement sensing indentation experiments.* Journal of materials research, 1992. **7**(6): p. 1564-1583.
78. Oliver, W.C. and G.M. Pharr, *Measurement of hardness and elastic modulus by instrumented indentation: Advances in understanding and refinements to methodology.* Journal of materials research, 2004. **19**(1): p. 3-20.
79. Hu, Y., X. Zhao, and Z. Suo, *Averting cracks caused by insertion reaction in lithium–ion batteries.* Journal of Materials Research, 2010. **25**(6): p. 1007-1010.
80. Schmuch, R., et al., *Performance and cost of materials for lithium-based rechargeable automotive batteries.* Nature Energy, 2018. **3**(4): p. 267.
81. Etacheri, V., et al., *Challenges in the development of advanced Li-ion batteries: a review.* Energy & Environmental Science, 2011. **4**(9): p. 3243-3262.
82. Zhang, J. and J. Lee, *A review on prognostics and health monitoring of Li-ion battery.* Journal of power sources, 2011. **196**(15): p. 6007-6014.
83. Berecibar, M., et al., *Critical review of state of health estimation methods of Li-ion batteries for real applications.* Renewable and Sustainable Energy Reviews, 2016. **56**: p. 572-587.
84. Ramadesigan, V., et al., *Modeling and simulation of lithium-ion batteries from a systems engineering perspective.* Journal of the electrochemical society, 2012. **159**(3): p. R31-R45.
85. Remmlinger, J., et al., *On-board state-of-health monitoring of lithium-ion batteries using linear parameter-varying models.* Journal of Power Sources, 2013. **239**: p. 689-695.
86. Li, S., et al., *A comparative study of model-based capacity estimation algorithms in dual estimation frameworks for lithium-ion batteries under an accelerated aging test.* Applied energy, 2018. **212**: p. 1522-1536.
87. Chen, C. and M. Pecht. *Prognostics of lithium-ion batteries using model-based and data-driven methods*. in *Proceedings of the IEEE 2012 Prognostics and System Health Management Conference (PHM-2012 Beijing)*. 2012. IEEE.
88. Raccuglia, P., et al., *Machine-learning-assisted materials discovery using failed experiments.* Nature, 2016. **533**(7601): p. 73.
89. Xue, D., et al., *Accelerated search for materials with targeted properties by adaptive design.* Nature communications, 2016. **7**: p. 11241.
90. Butler, K.T., et al., *Machine learning for molecular and materials science.* Nature, 2018. **559**(7715): p. 547.
91. Yuan, R., et al., *Accelerated Discovery of Large Electrostrains in BaTiO3‐Based Piezoelectrics Using Active Learning.* Advanced Materials, 2018. **30**(7): p. 1702884.
92. Wu, L., X. Fu, and Y. Guan, *Review of the remaining useful life prognostics of vehicle lithium-ion batteries using data-driven methodologies.* Applied sciences, 2016. **6**(6): p. 166.
93. Wu, J., C. Zhang, and Z. Chen, *An online method for lithium-ion battery remaining useful life estimation using importance sampling and neural networks.* Applied energy, 2016. **173**: p. 134-140.
94. Hu, C., et al., *Data-driven method based on particle swarm optimization and k-nearest neighbor regression for estimating capacity of lithium-ion battery.* Applied Energy, 2014. **129**: p. 49-55.

95. Patil, M.A., et al., *A novel multistage Support Vector Machine based approach for Li ion battery remaining useful life estimation.* Applied Energy, 2015. **159**: p. 285-297.
96. Nuhic, A., et al., *Health diagnosis and remaining useful life prognostics of lithium-ion batteries using data-driven methods.* Journal of power sources, 2013. **239**: p. 680-688.
97. Severson, K.A., et al., *Data-driven prediction of battery cycle life before capacity degradation.* Nature Energy, 2019. **4**(5): p. 383.
98. Berecibar, M., et al., *Online state of health estimation on NMC cells based on predictive analytics.* Journal of Power Sources, 2016. **320**: p. 239-250.
99. Choi, J.W. and D. Aurbach, *Promise and reality of post-lithium-ion batteries with high energy densities.* Nature Reviews Materials, 2016. **1**(4): p. 16013.
100. Shin, H., J. Zhang, and W. Lu, *Material structure and chemical bond effect on the electrochemical performance of black phosphorus-graphite composite anodes.* Electrochimica Acta, 2019. **309**: p. 264-273.
101. Shin, H., J. Zhang, and W. Lu, *A Comprehensive Study of Black Phosphorus-Graphite Composite Anodes and HEMM Synthesis Conditions for Improved Cycle Stability.* Journal of The Electrochemical Society, 2019. **166**(12): p. A2673-A2682.
102. Huang, Y., et al., *Interaction of black phosphorus with oxygen and water.* Chemistry of Materials, 2016. **28**(22): p. 8330-8339.
103. Shin, H., et al., *Degradation of the solid electrolyte interphase induced by the deposition of manganese ions.* Journal of Power Sources, 2015. **284**: p. 416-427.
104. Janot, R. and D. Guérard, *Ball-milling in liquid media: Applications to the preparation of anodic materials for lithium-ion batteries.* Progress in Materials Science, 2005. **50**(1): p. 1-92.
105. Chen, Y., et al., *Nanoporous carbon produced by ball milling.* Applied physics letters, 1999. **74**(19): p. 2782-2784.
106. Kado, Y., et al., *Pulverized Graphite by Ball Milling for Electric Double-Layer Capacitors.* Journal of The Electrochemical Society, 2019. **166**(12): p. A2471-A2476.